

Utah State University

DigitalCommons@USU

All Graduate Theses and Dissertations

Graduate Studies

12-2018

Mesospheric Gravity Wave Climatology and Variances Over the Andes Mountains

Jonathan Rich Pugmire
Utah State University

Follow this and additional works at: <https://digitalcommons.usu.edu/etd>



Part of the [Physics Commons](#)

Recommended Citation

Pugmire, Jonathan Rich, "Mesospheric Gravity Wave Climatology and Variances Over the Andes Mountains" (2018). *All Graduate Theses and Dissertations*. 7387.
<https://digitalcommons.usu.edu/etd/7387>

This Dissertation is brought to you for free and open access by the Graduate Studies at DigitalCommons@USU. It has been accepted for inclusion in All Graduate Theses and Dissertations by an authorized administrator of DigitalCommons@USU. For more information, please contact digitalcommons@usu.edu.



MESOSPHERIC GRAVITY WAVE CLIMATOLOGY AND
VARIANCES OVER THE ANDES MOUNTAINS

by

Jonathan Rich Pugmire

A dissertation submitted in partial fulfillment
of the requirements for the degree

of

DOCTOR OF PHILOSOPHY

in

Physics

Approved:

Michael J. Taylor, Ph.D.
Major Professor

Ludger Scherliess, Ph.D.
Committee Member

Robert Schunk, Ph.D.
Committee Member

Vincent Wickwar, Ph.D.
Committee Member

Robert Gillies, Ph.D.
Committee Member

Laurens H. Smith, Ph.D.
Interim Vice President for Research and
Interim Dean of the School of Graduate Studies

UTAH STATE UNIVERSITY
Logan, Utah

2018

Copyright © Jonathan Rich Pugmire 2018

All Rights Reserved

ABSTRACT

Mesospheric Gravity Wave Climatology and Variances over the Andes Mountains

by

Jonathan Rich Pugmire, Doctor of Philosophy

Utah State University, 2018

Major Professor: Michael J. Taylor, Ph.D.

Department: Physics

Atmospheric gravity waves transfer huge amounts of energy and momentum from weather driven sources in the lower atmosphere into the middle and upper atmosphere where they break and deposit this energy driving seasonal changes in the mesospheric temperature and wind fields. This dissertation uses recently obtained extensive measurements by the Utah State University Mesospheric Temperature Mapper (MTM) which has operated autonomously at the Andes Lidar Observatory since 2009. The primary research goal is to investigate and quantify mesospheric gravity wave climatology and associated OH temperature variances over the Andes Mountain Range, which is an important but sparsely studied region. The Andes provide a natural laboratory for novel studies of the occurrence and properties of orographically forced "mesospheric mountain waves" (MWs) which are generated by the interaction of strong eastward winds with the towering Andes Mountains. These standing waves are well documented in the troposphere and stratosphere and can constitute large perturbations in these regions, yet their detection in the mesosphere, until recently, has been rare. This climatology study –utilizing over 1700 nights of mesospheric GW measurements and temperature variances –yields new knowledge of seasonal oscillations on the mesospheric dynamics. This extensive data set reveals large day-to-day

variability, interannual variability with a well-defined semiannual oscillation and an occasional quarter-annual oscillation. Comparisons of the MTM data set with temperature measurements obtained by the SABER radiometer on the TIMED satellite show the reliability of the MTM temperature measurements with a warm bias of 5.5 K, consistent with other ground-based studies. The combined MTM temperature variance and SABER vertical temperature profiles reveal a significant increase in temperature variance and gravity wave potential energy during the winter months. Somewhat surprisingly, MWs were identified on 10% of the clear wintertime nights during the period of 2012–2017. Statistical analysis of the mountain waves reveals they are short lived (~ 2.7 h), very low phase speed (i.e., quasi-stationary), and are well-aligned with the Andes Mountain Range. Available radiosonde wind and meteor-wind radar data reveal favorable wind conditions for MW propagation from the mountains into the mesopause region (~ 90 km) during the winter months.

(182 pages)

PUBLIC ABSTRACT

Mesospheric Gravity Wave Climatology and Variances over the Andes Mountains

Jonathan Pugmire

Look up! Travelling over your head in the air are waves. They are present all the time in the atmosphere all over the Earth. Now imagine throwing a small rock in a pond and watching the ripples spread out around it. The same thing happens in the atmosphere except the rock is a thunderstorm, the wind blowing over a mountain, or another disturbance. As the wave (known as a gravity wave) travels upwards the thinning air allows the wave to grow larger and larger. Eventually the gravity wave gets too large – and like waves on the beach – it crashes causing whitewater or turbulence. If you are in the shallow water when the ocean wave crashes or breaks, you would feel the energy and momentum from the wave as it pushes or even knocks you over. In the atmosphere, when waves break they transfer their energy and momentum to the background wind changing its speed and even direction. This affects the circulation of the atmosphere.

These atmospheric waves are not generally visible to the naked eye but by using special instruments we can observe their effects on the wind, temperature, density, and pressure of the atmosphere. This dissertation discusses the use of a specialized camera to study gravity waves as they travel through layers of the atmosphere 50 miles above the Andes Mountains and change the temperature. First, we introduce the layers of the atmosphere, the techniques used for observing these waves, and the mathematical theory and properties of these gravity waves. We then discuss the camera, its properties, and its unique feature of acquiring temperatures in the middle layer of the atmosphere. We introduce the observatory high in the Andes Mountains

and why it was selected. We will look at the nightly fluctuations (or willy-nilly-ness) and long-term trends from August 2009 until December 2017. We compare measurements from the camera with similar measurements obtained from a satellite taken at the same altitude and measurements from the same camera when it was used at a different location, over Hawaii. Next, we measure the amount of change in the temperature and compare it to a nearby location on the other side of the Andes Mountains. Finally, we look for a specific type of gravity wave caused by wind blowing over the mountains called a mountain wave and perform statistics of those observed events over a period of six years.

By understanding the changes in atmospheric properties caused by gravity waves we can learn more about their possible sources. By knowing their sources, we can better understand how much energy is being transported in the atmosphere, which in turn helps with better weather and climate models.

Even now –all of this is going on over your head!

ACKNOWLEDGMENTS

I would like to publicly acknowledge and thank all those who have contributed to the completion of this dissertation. First, I would like to thank my major professor, Dr. Mike Taylor for his time, support, and guidance. I would also like to thank Dr. Dominique Pautet and Dr. Yucheng Zhao for our frequent discussions. They have helped so much with answering my continuous stream of questions about computer problems, software, programming, understanding the results, and editing this dissertation. I would like to thank my committee for providing feedback and edits, and being flexible with their time: Dr. Ludger Scherliess, Dr. Robert Schunk, Dr. Vince Wickwar, and Dr. Robert Gillies. Additionally, all the professors and teachers throughout my life who have helped and motivated me.

I would like to thank the Physics Department Staff particularly Karalee Ransom for all the candy and help she has provided to me and to the many others I have sent to her office over the years. I would also like to thank Vanessa Chambers for her help editing this dissertation. I would like to thank fellow graduate students who have helped me in my graduate career and provided valuable feedback for my research and dissertation: David Hansen, Kenneth Zia, Neal Criddle, and Michael Negale.

The operation and analysis of the MTM was supported by NSF grant 1110215. Support for my graduate research and this dissertation was also provided by the Keith Taylor Endowed Graduate Fellowship, the Graduate Enhancement Award, Utah NASA Space Grant Consortium Fellowship, and by working as a Graduate Teaching Assistant for the Physics Department.

I would like to thank the academy: my parents Doug and Norine, siblings, in-laws, and other extended family and friends who have helped over the years. I could not have done it without their love and support. I would like to thank the most important people in my life: my beautiful wife, Alisha for her love and encouragement; and my

kids, Isaac and Rachael. They have helped me stay focused, prioritize things that are most important, given me fun breaks to deal with stress; they sacrificed time and opportunities while I worked long hours on graduate classes, teaching, research, and dissertation writing.

Finally, I acknowledge and thank God, the Creator and the Source of all knowledge for "with God all things are possible."

Jonathan Rich Pugmire

CONTENTS

	Page
ABSTRACT	iii
PUBLIC ABSTRACT	v
ACKNOWLEDGMENTS	vii
LIST OF TABLES	xi
LIST OF FIGURES	xii
CHAPTER	
1. INTRODUCTION	1
1.1. The Earth's Atmosphere	1
1.2. Atmospheric Airglow Emissions	4
1.3. Atmospheric Waves	7
1.4. Summary of Chapters	14
2. THE MESOSPHERIC TEMPERATURE MAPPER	16
2.1. Introduction	16
2.2. The MTM	16
2.3. MTM Data Acquisition	19
2.4. MTM Data Processing and Derivation of Temperature	20
2.5. Zenith Temperature	23
2.6. Temperature Map	24
2.7. Keogram Representation	25
2.8. Spectral Analysis	29
2.9. Summary	30
3. MESOSPHERIC TEMPERATURE CLIMATOLOGY OVER THE ANDES 32	
3.1. Early Campaigns	32
3.2. Andes Lidar Observatory	33
3.3. ALO MTM Operations	35
3.4. MTM Nightly Data	36
3.5. Investigating Seasonal Trends at ALO	40
3.6. Summary and Conclusions	55

4. COINCIDENT MTM AND SABER MEASUREMENTS OF MESOSPHERIC TEMPERATURE OVER ALO	57
4.1. Introduction	57
4.2. SABER Instrument and OH Temperature Data	59
4.3. ALO MTM and SABER Temperature Comparison	66
4.4. Summary and Conclusions	76
5. MESOSPHERIC TEMPERATURE VARIANCE MEASUREMENTS OVER THE ANDES MOUNTAINS	80
5.1. Introduction	80
5.2. MTM Variance Method and Data	80
5.3. SABER Variance and Potential Energy Measurements	91
5.4. Summary and Conclusions	97
6. OBSERVATIONS OF MESOSPHERIC MOUNTAIN WAVE STRUCTURE AND DYNAMICS OVER THE ANDES	99
6.1. Introduction to Mountain Waves	99
6.2. Mountain Wave Observations at ALO	106
6.3. Summary and Conclusions	120
7. SUMMARY AND FUTURE WORK	123
7.1. Summary	123
7.2. Future Work	126
REFERENCES	129
APPENDIX	155
APPENDIX A COPYRIGHT PERMISSIONS	156
CURRICULUM VITAE	162

LIST OF TABLES

Table	Page
2.1. Characteristics of MTM Filters Used For Airglow Observations at ALO.	20
3.1. OH Band Intensity and OH Rotational Temperature Nocturnal Averages for Nights in Figure 3.3.	40
3.2. Results of the Harmonic Fits to the OH Rotational Temperature Time Series for the Years 2009–2017 at ALO.	43
3.3. Results of the Harmonic Fits to the T_{OH} Time Series For the Superposed Year (Figure 3.12a).	55
4.1. Coincidence SABER Temperature and T_{OH} Measurements For 2009–2016 Using Different Size Latitude-Longitude Boxes Centered on ALO.	62
4.2. Yearly Mean SABER T_k and Mean T_{OH} and Standard Deviations, σ .	68
4.3. Temperature Comparison Between SABER and Several Ground-based Instruments	77
6.1. Parameters of Mountain Waves Observed at ALO and Notation of Coincidence Measurements From Other Instruments.	110

LIST OF FIGURES

Figure	Page
1.1. Temperature structure showing the layers of the Earth's atmosphere.	2
1.2. Visible and near infrared spectrum of common atomic and molecular emissions in the Earth's middle atmosphere.	5
1.3. Image taken from the International Space Station showing several air-glow emission layers in the MLT region.	6
1.4. Normalized emission layer altitudes for several species dominant in the MLT region.	7
1.5. Free-body diagram showing a parcel of air moving up an inclined plane with the buoyancy force and gravitational force acting on it.	9
2.1. The MTM imaging system and example image.	17
2.2. Schematic diagram showing the MTM imager and its specialized optics.	18
2.3. Image processing steps for an example image taken on 8 July 2012.	21
2.4. Emissions given by different OH (6,2) vibrational transitions.	22
2.5. MTM OH temperature data for 14 August 2010 and several temperature measurements from the Na lidar at 87, 88, and 89 km altitudes.	23
2.6. Measurements made by the MTM on the night of 2–3 November 2016.	24
2.7. Processed OH (6,2) relative band intensity map taken at 2337 UT and averaged rotational temperature map taken from ALO on 8 July 2012.	25
2.8. Keogram creation process for the night of 22–23 June 2012.	26
2.9. E-W OH band intensity keograms with 5–60 min and >60 min band-pass filters applied for the night of 22–23 June 2012.	28
2.10. Zenith OH rotational temperature and band intensity for 22–23 June 2012 showing the same small-scale GW signature as the top of Figure 2.9.	28
2.11. Result of 2-D FFT spectral analysis of intensity image of Figure 2.7a showing the symmetric spectrum from which ϕ and λ_H are obtained.	29

3.1. The Andes Lidar Observatory (right image) is located (red marker on map) in the Chilean Andes Mountains of South America (30.3°S, 70.7°W, 2530 m).	35
3.2. Plots showing the raw intensity measurements for nine nights throughout the program.	38
3.3. OH band intensity measurements with derived OH rotational temperature for the same nights as in Figure 3.2.	39
3.4. MTM nightly averaged T_{OH} measurements for each year 2010–2017.	42
3.5. MTM nightly averaged T_{OH} measurements from 12 August 2009 until 31 December 2017 (years are separated by black vertical lines).	45
3.6. Monthly averaged OH temperatures from August 2009 to June 2017 showing clear SAO.	45
3.7. Lomb-Scargle periodogram analysis of T_{OH} for the 8-year data set showing annual and semiannual oscillation signatures.	46
3.8. MTM nightly averaged T_{OH} measurements shown in one superposed year for both ALO and Maui.	47
3.9. Harmonic analysis of Figure 3.8 showing the amplitude and phase of the AO, SAO, and QAO observed by the MTM at ALO and Maui.	49
3.10. T_{OH} measured from 12 August 2009 until 31 December 2017.	51
3.11. Similar to Figure 3.10 except each year (2009–2017) is shown separately for better resolution.	52
3.12. Thirty-minute T_{OH} data from Figure 3.10 folded into one superposed year for raw data and with tides removed.	53
3.13. Results of harmonic analysis showing half-hour bins of the amplitude of the AO and SAO signatures from Figure 3.12, with and without tides.	54
4.1. Comparison of different OH layer thickness assumptions.	63
4.2. SABER versions 1.07 and 2.0 OH-equivalent temperature comparison.	64
4.3. Temperature difference between SABER and MTM observed over Maui.	65
4.4. MTM data obtained 22–23 May 2012 and 7–8 September 2013 with coincident SABER measurement.	67

4.5.	Time series of the SABER T_k and the MTM T_{OH} with a 30-day running mean applied to both data sets.	68
4.6.	Temperature difference between SABER and MTM observed over ALO.	69
4.7.	Scatter plots of the MTM T_{OH} versus SABER T_k and GRIPS OH temperature versus SABER T_k showing linear relationships.	70
4.8.	Monthly mean difference between the SABER T_k and the MTM T_{OH} folded into one year for 2009–2016 at ALO.	72
4.9.	MTM nightly mean T_{OH} with a second-order polynomial showing the long-term trend along with the solar activity as measured by F10.7 cm.	73
4.10.	Nighttime SABER T_k 2002–2017 over ALO and the solar F10.7 index.	74
4.11.	Dependence of the nocturnal mean T_{OH} and SABER T_k on the F10.7 cm index.	76
5.1.	I_{OH} and T_{OH} for UT day 212, (29–30 July) 2016.	82
5.2.	Raw T'^2 for the year 2014 with a 30-day smoothing, and GW T'^2 measurements with the 24 h and 12 h tides removed with a 30-day smoothing.	83
5.3.	T'^2 measurements with the 24 h and 12 h tides removed for several years with a 30-day smoothing.	84
5.4.	GW variance with the tides removed for all eight years consecutively.	85
5.5.	Average seasonal variance from nearby El Leoncito, Argentina for OH and O ₂ shown by a 29-night running mean.	86
5.6.	Composite year of the MTM OH variance data (2009–2017).	86
5.7.	Distribution of nightly η values for all nights (2009–2016).	88
5.8.	Example of bandpass filter subtraction for 30 July 2016.	89
5.9.	Average seasonal variance based on scale of GW.	90
5.10.	The process to reveal GW fluctuations from SABER temperature profiles.	92
5.11.	Comparison of the SABER measured temperature variance with the MTM measured T'^2 for 5 years.	93

5.12. Contour plot showing the monthly mean GW PE plotted for 13 years superposed into one year.	95
5.13. Average cycle of the GW potential energy over ALO taken at 10 km intervals throughout the stratosphere and mesosphere.	95
5.14. Vertical profiles of potential energy derived from SABER averaged over each 3-month season: winter, spring, summer, and fall.	96
6.1. Stably stratified air is lifted over mountains and oscillates about its equilibrium height on the lee side of the mountain, producing stationary waves.	100
6.2. Depiction of the vertical propagation of MWs showing their largest amplitudes happen well above the mountains.	101
6.3. Plot showing seasonal zonal wind speed profiles.	103
6.4. Monthly mean MLS radiance variance measurements and monthly temperature variance measurements over the Andes for two years (1995–1996).	105
6.5. All-sky time-averaged OH images each obtained from averaging ~60 images during the ~11 hr night on three successive nights (2–4 July 2008).	106
6.6. E-W keogram made from pixel 32 for the night of 2–3 June 2013 (UT day 154).	108
6.7. E-W keogram made from the middle pixels for the night of 8–9 July 2012.	109
6.8. Observed parameters of MW events from ALO, 2012–2017.	112
6.9. Zonal wind profiles recorded by three radiosondes before, during, and after MTM observed MW events on the night of 29–30 June 2014.	114
6.10. E-W keogram for the night of 29–30 June 2014.	114
6.11. Radiosonde soundings of the zonal wind profiles, u , taken at 00 UT only for 17 of the 37 nights when MW signatures coincide with the radiosonde soundings at 00 UT.	115
6.12. Example MR measurements showing different zonal wind conditions when MW were detected in the MLT region by the MTM.	116

6.13. Plots showing MW signature in the keogram, as well as coincident MR u winds and radiosonde u wind measurements for the night of 18 June 2013.	119
6.14. E-W keogram and corresponding CIPS images taken on the night of 27–28 June 2016.	120
7.1. Monthly mean ΔT between the SABER T_k and the MTM T_{OH} for 2009–2017 at ALO.	127
7.2. Nightly average temperature during each January and February from 2011 to 2016 showing two-day wave structure.	128
A.1. Copyright permission for use of Figure 4.3.	157
A.2. Copyright permission for use of Figure 4.7b.	158
A.3. Copyright permission for use of Figure 5.5.	159
A.4. Copyright permission for use of Figure 6.4.	160
A.5. Copyright permission for use of Figure 6.5.	161

CHAPTER 1

INTRODUCTION

This dissertation presents a study of atmospheric gravity wave (GW) temperatures and climatology in the middle atmosphere conducted at the Andes Lidar Observatory (ALO) located high in the Andes Mountain Range, Cerro Pachón, Chile, providing some of the best nighttime viewing conditions in the world. This introductory chapter acquaints the reader with necessary background and theory to understand (i) the thermal layers of our atmosphere, (ii) the atmospheric phenomena that enables the detection and measurement of waves in the middle atmosphere, and (iii) the mathematical theory and fundamentals describing atmospheric waves including their sources, propagation, and dissipation.

1.1. The Earth's Atmosphere

The Earth's atmosphere is a thin layer of gas held in hydrostatic equilibrium by the force of gravity. The atmosphere's density and pressure decrease exponentially with altitude, and eventually merges with the near-vacuum space environment. The structure of the atmosphere is characterized by the vertical distribution of pressure, temperature, density, and composition. The atmosphere maintains a balance between the absorption of solar radiation and the outgoing thermal radiation. This balance causes a complex temperature profile that varies not only with altitude but also with season, local time, and geographic location. The atmosphere consists mostly of molecular nitrogen (78%) and oxygen (21%), in addition to many minor species. The neutral atmosphere is divided into four regions as shown in Figure 1.1 distinguished by their different temperature gradients: the troposphere, stratosphere, mesosphere, and thermosphere. Pauses—the boundaries separating these regions—correspond to a change in sign in the gradient of the temperature profile. The figure shows that the

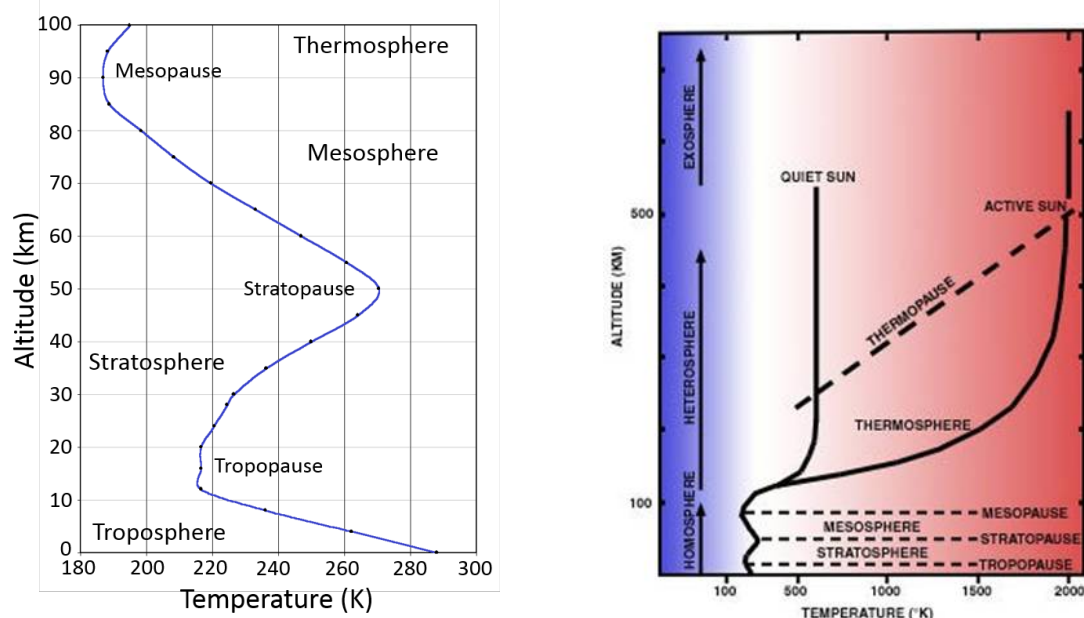


Figure 1.1. Temperature structure showing the layers of the Earth’s atmosphere. Left plot is zoomed in on the lower 100 km. Right plot shows the solar effects in the thermosphere and is adapted from *Banks and Kockarts* [2013].

temperature varies greatly (~ 150 K) from the surface up into the lower thermosphere. The solar cycle also contributes considerably to deviations in the temperature profile, particularly in the thermosphere [*Schunk and Nagy*, 2004].

The lowest region of the atmosphere, termed the troposphere, extends from the surface to a height of ~ 10 – 15 km, depending on latitude. It contains about 75% of the atmosphere’s mass and most of the water vapor. It is characterized by an unstable positive lapse rate (negative temperature gradient) of ~ 6 – 7 K km^{-1} and is well-mixed. Solar radiation that penetrates to the Earth’s surface is absorbed and heats the air which rises into the cooler region above. As the air rises, it expands due to the lower surrounding pressure, causes a drop in temperature due to adiabatic cooling, and results in vertical convection. Therefore, the troposphere is unstable and very dynamic, generating a wide variety of atmospheric weather phenomena.

The stratosphere is the region where the ozone layer (O_3) exists, and extends from the tropopause to a height around $\sim 45\text{--}50$ km where it reaches a temperature of about 270 K. It is characterized by a negative lapse rate due to the absorption of solar ultraviolet radiation by the ozone layer and is thermodynamically stable with very little convection.

At the stratopause the temperature again reverts to a positive lapse rate in the region defined as the mesosphere where the temperature continues to decrease with altitude, until it reaches the coldest region on the Earth: the mesopause ($\sim 85\text{--}100$ km). Due to GW effects, the summer mesopause is lower and colder (~ 140 K) than the winter mesopause [*Qian et al.*, 2017; *Schmidlin*, 1992]. In this region, very little absorption takes place which causes an energy deficit and subsequent cooling. The mesosphere also consists mostly of molecular nitrogen and oxygen, in addition to many minor species. Some metals such as sodium and iron, originating from meteor ablation, form metal-rich layers in the upper mesosphere.

Above the mesosphere in the thermosphere ($\sim 90\text{--}600$ km), the temperature increases rapidly with altitude until it reaches the exosphere where the density is too low to behave like a gas. In the thermosphere, where atomic oxygen and nitrogen absorb incoming solar extreme ultra violet (EUV) radiation, the temperature ranges from $\sim 700\text{--}1400$ K, reaching up to 2000 K during solar maximum conditions (see Figure 1.1). The temperature increases rapidly in the lower thermosphere and then stays fairly constant with increasing altitude. Energetic ultraviolet and x-ray radiation also cause ionization of atmospheric molecules (mainly N_2 and O_2) resulting in ionized gas and creating the ionosphere. At predominantly high-latitude regions, charged particles driven by the solar wind precipitate down the Earth's magnetic field lines and lose energy by exciting and ionizing atmospheric constituents. These excited constituents emit light in varying colors, creating the aurora.

Together the upper mesosphere and lower thermosphere (MLT) region (~ 80 – 100 km), including the mesopause boundary between them, is a complex system. Its thermal structure is strongly controlled by several physical processes (e.g., absorption of incident solar radiation, auroral heating, and infrared radiative cooling) and dynamical processes from the lower atmosphere including GWs, tides and planetary waves [*Mlynczak and Solomon, 1993; Nappo, 2002; Smith, 2004*] which deposit large amounts of energy and momentum. Knowledge of temperature and its variability with altitude in the MLT region is an important parameter in understanding its structure and dynamics.

1.2. Atmospheric Airglow Emissions

Airglow, frequently referred to as nightglow, is an emission of light which occurs in the MLT region between 80 – 120 km. As opposed to the bright, sporadic aurora which primarily occur at high latitudes, airglow is distinguished as being global and ever-present in its nature [*Nappo, 2002*]. Airglow emissions are produced indirectly by solar radiation absorbed in the sunlit part of the atmosphere. During the day, some atmospheric molecules and atoms are photoionized or dissociated by incoming solar radiation and recombine chemically de-exciting to a lower-energy state as first suggested by *Chapman* [1931] and emit a optical emission in the visible and near infrared (NIR) spectrum that we now term airglow [*Chamberlain, 1961; Wallace and Broadfoot, 1969*]. After the sun has set, the recombination continues and these emissions, termed nightglow, are detectable from the ground at specific wavelengths. Several sources of airglow occur at specific wavelengths, e.g., atomic oxygen OI emissions at 557.7 nm (green line) and at 630.0 nm (red line), the O₂ (0,1) emission at 866.0 nm, and the sodium, Na, emission at 589.2 nm as shown in Figure 1.2. The NIR domain is dominated by several hydroxyl (OH) molecular band emissions identified first by *Meinel* [1950] (see Figure 1.2).

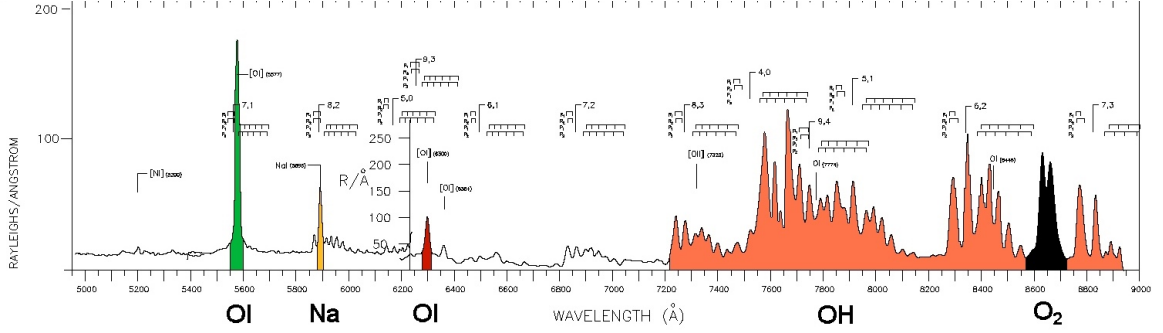
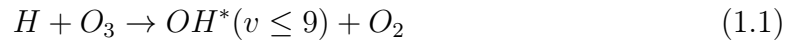


Figure 1.2. Visible and near infrared spectrum of common atomic and molecular emissions in the Earth’s middle atmosphere. Note the OH band has a very broad emission due to the many vibrational modes. OI, Na and O₂ are also marked. Adapted from *Broadfoot and Kendall* [1968].

Each of these emission layers occur at a particular altitude as shown from space in Figure 1.3 and can act as tracers for GWs. Several of these layers in the MLT are shown in Figure 1.4. The NIR OH Meinel airglow emissions originate in a relatively thin layer nominally centered at ~ 87 km with a layer thickness of ~ 6 – 10 km, while the Na emission originates from an altitude of ~ 90 km, O₂ at ~ 94 km, and atomic OI emission at ~ 96 km, each with similar layer thicknesses as OH [*Baker and Stair Jr*, 1988].

In this study we focus on the NIR OH airglow emissions which is the brightest emission in the visible and NIR spectrum. The excited OH arises from the reaction of hydrogen and ozone [*Bates and Nicolet*, 1950; *Gardner and Taylor*, 1998; *Herzberg*, 1951]:



The OH is formed in an excited vibrational state ($v \leq 9$) as represented by the asterisk in Equation 1.1. The release of this excess energy relaxes the OH molecules and creates a series of overlapping molecular band emissions spanning the range of 0.4 – $4.0 \mu\text{m}$ and dominating the NIR spectrum. As noted, the OH emission is the most



Figure 1.3. Image taken from the International Space Station showing several airglow emission layers in the MLT region [NASA ISS image ISS042-E-037847].

intense nightglow emission and is easily detectable at ground level using sensitive imaging and photometric instruments. The intensity of the photochemical emission is proportional to the local density of the emitting species and the temperature, and variations can be related to the variations of density and temperature. Temperature variations are directly related to the GW perturbations.

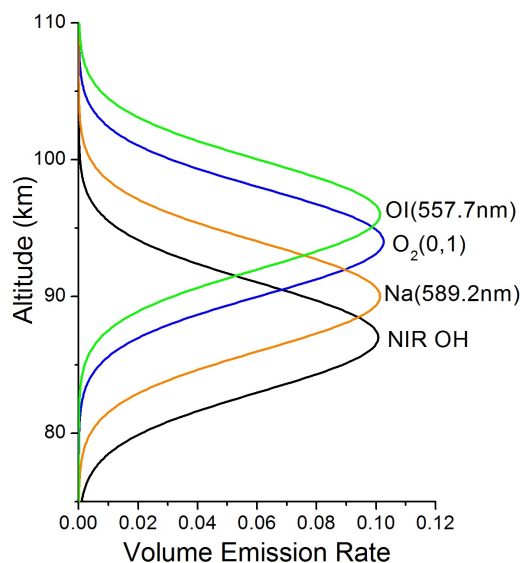


Figure 1.4. Normalized emission layer altitudes for several species dominant in the MLT region. OH and O₂ have nominal altitudes of 87 km and 92 km, respectively [Courtesy M.J. Taylor].

1.3. Atmospheric Waves

Wave phenomena are a result of perturbations in any medium and are prevalent in fluids: bodies of water and planetary atmospheres. Atmospheric waves can be classified into two main groups based on their scale-sizes. There are large-scale waves known as planetary waves and tides. They are both global in nature and exhibit coherent patterns in both latitude and longitude. Tides are mostly generated by the absorption of solar radiation by water vapor and ozone in the troposphere and stratosphere, respectively, during the day [Forbes, 1982]. The rapid tidal heating as the Earth rotates induces oscillations with periods that are harmonics of the 24-h length of a solar day (e.g., a wave with a 24-h period is the diurnal tide, 12-h period is the semidiurnal tide, 8-h period for the terdiurnal, etc.). These waves propagate westward with the sun and are referred to as migrating tides. Planetary waves, also known as Rossby waves, are induced by the periodic structure of the land-sea topography which creates global waves with larger periods (e.g., 2, 16, 28 days).

On smaller scales, atmospheric GWs, or buoyancy waves, are transverse and coherent oscillations resulting from the restoring forces of gravity and buoyancy acting on a vertically perturbed parcel of air in a stably stratified atmosphere. *Hines* [1960] first proposed the existence of GWs to explain wave-like phenomena evident in long-lived meteor trains and noctilucent clouds observed in the upper atmosphere. *Hines* [1989] laid the groundwork for what is now known as linear GW theory. The study of GWs continues to expand with quantitative advances in observational and computational techniques [*Fritts and Alexander, 2003; Nappo, 2002*]. Importantly, GWs are ubiquitous and play a dominant role in the structure, energetics, and dynamics of the MLT region by coupling the lower and upper atmospheric layers together [*Reid, 1986*]. GW oscillations occur within the fluid (atmosphere) and are sometimes called internal waves. GWs typically have periods of tens of minutes to several hours. Depending on their period, internal GWs propagate predominantly slantwise from their sources in the troposphere into the stratosphere and mesosphere [e.g., *Hines, 1960; Nappo, 2002; Sica and Russell, 1999; Taylor and Pendleton Jr, 2003*].

GWs are global in nature but usually have local and/or regional sources and their propagation depends on their wave properties and the prevailing atmospheric conditions. Their influence extends throughout all of the layers of the atmosphere. GW sources generally exist in the troposphere and stratosphere and propagate upwards into the upper atmosphere where wave amplitudes increase as the background density decreases [e.g., *Hines, 1960; McIntyre et al., 2003; Nappo, 2002*]. GWs can be generated from storms, volcanoes, earthquakes, the jet stream, and the flow of air over mountains (known as mountain waves) [e.g., *Fritts and Alexander, 2003; Fritts and Nastrom, 1992; Holton and Alexander, 1999; Lu et al., 1984; Nastrom and Fritts, 1992; Preusse et al., 2002; Tsuda et al., 1994*]. Ducted waves are trapped within density or wind discontinuity boundary layers and can propagate large horizontal dis-

tances within the “wave guide.” Thus, in the atmosphere ducted waves, propagating GWs, evanescent waves, and stationary waves can all be found. Waves that propagate freely through the atmosphere can transfer significant amounts of energy and momentum from the troposphere and stratosphere into the overlying MLT region.

1.3.1. Buoyancy Frequency

Atmospheric GWs are often described using a free-body diagram of a parcel of air that is moving up a ramp with the angle β [Nappo, 2002]. The parcel of air, represented as a box, has the force of gravity acting on it downwards and the buoyancy force acting on it upwards as shown in Figure 1.5. As the parcel of air moves up the ramp, it is displaced vertically. The region above is less dense and so the parcel is no longer in hydrostatic equilibrium. Gravity acts as a restoring force to bring it back down to its original height. The returning parcel of air has inertia and will overshoot the original height into a more dense layer below where the buoyancy force will push the parcel of air back up. Assuming the fluid is stable, the parcel of air will oscillate up and down about the point of zero net force, with a frequency of oscillation known as the Brunt-Väisälä frequency, N , which is dependent on the atmospheric conditions and the force of gravity [Fritts and Alexander, 2003; Nappo, 2002].

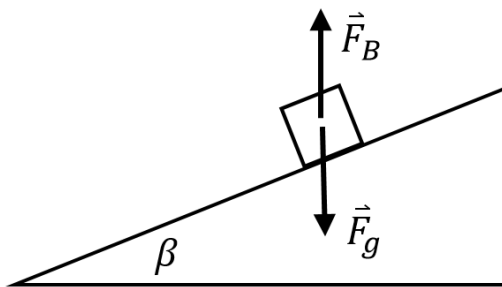


Figure 1.5. Free-body diagram showing a parcel of air moving up an inclined plane with the buoyancy force and gravitational force acting on it. Modified from Nappo [2002].

Following *Nappo* [2002], using Newton's second law to add up the forces acting on the parcel of air gives

$$m_p \frac{d^2 z}{dt^2} = -g \sin \beta (m_p - m_a), \quad (1.2)$$

where m_p is the mass of the parcel of air, g is gravity, and m_a is the mass of the ambient or surrounding air. Substituting the ideal gas law in order to relate the masses to temperature gives

$$\frac{d^2 z}{dt^2} = -g \sin \left(\beta \frac{T_a - T_p}{T_a} \right), \quad (1.3)$$

where T_p is temperature of the parcel of air and T_a is the ambient temperature. The real part of the solution is a sine function expressing the motion of a wave. In order for the wave to propagate in the atmosphere it must have a shorter frequency than the buoyancy frequency

$$N = -\sqrt{\frac{g}{\rho_o} \frac{\partial \rho_o}{\partial z} \sin \beta}, \quad (1.4)$$

which can be expressed in terms of the atmospheric density at sea level, ρ_o . Often-times the buoyancy frequency is expressed as N^2 so the number is always positive. The Brunt-Väisälä frequency is the maximum vertical frequency a wave can have and still propagate in the atmosphere. $N \approx 0.02 \text{ s}^{-1}$ and corresponds to a wave period of ~ 5 minutes [*Nappo*, 2002]. If β is 90° then the minimum period is about 5 minutes, and as β decreases, the wave period increases. Therefore, short period waves propagate almost vertically and waves with much larger periods travel obliquely almost horizontally.

1.3.2. Linear Gravity Wave Theory

GWs are frequently described with a simple linear theory that treats them as

small perturbations from a stable, stratified background varying only in the vertical direction. Using Linear Theory and starting with the Euler Equations, atmospheric GW motion can be described. The following equations used to describe atmospheric GWs are the momentum equations in the x -direction (1.5) and the z -direction (1.6), the mass-continuity equation (1.7), and energy equation (1.8):

$$\frac{\partial u}{\partial t} + u \frac{\partial u}{\partial x} + w \frac{\partial u}{\partial z} = -\frac{1}{\rho} \frac{\partial p}{\partial x}, \quad (1.5)$$

$$\frac{\partial w}{\partial t} + u \frac{\partial w}{\partial x} + w \frac{\partial w}{\partial z} = -\frac{1}{\rho} \frac{\partial p}{\partial z} - g, \quad (1.6)$$

$$\frac{\partial u}{\partial x} + \frac{\partial w}{\partial z} = 0, \quad (1.7)$$

$$\frac{\partial \rho}{\partial t} + u \frac{\partial \rho}{\partial x} + w \frac{\partial \rho}{\partial z} = 0, \quad (1.8)$$

where u and w are the fluid (wind) velocity vectors in the x - and z -directions; p is pressure, and ρ is density. These four equations, in addition to the Buoyancy Frequency squared from equation (1.4), define a complete set of equations describing inviscid fluid motion [Fritts and Alexander, 2003].

In order to solve the system of equations, we perturb them from equilibrium (assuming the perturbations are small) and linearize them, ignoring any non-linear terms. It is assumed that the solution is a plane wave. The wave equation for linear GWs is referred to as the *Taylor-Goldstein* equation [Nappo, 2002].

If we look at the simple case of constant background stratification and constant buoyancy frequency, then the *Taylor-Goldstein* equation gives a dispersion relation of

$$m^2 = \frac{k^2 N^2}{\Omega^2} - k^2 - \frac{1}{4H_s^2}, \quad (1.9)$$

where m^2 is the vertical wavenumber related to the vertical wavelength, λ_z , by

$$m = \frac{2\pi}{\lambda_z}, \quad (1.10)$$

where k^2 is the horizontal wavenumber related to the horizontal wavelength, λ_x , by

$$k = \frac{2\pi}{\lambda_x}, \quad (1.11)$$

The intrinsic frequency, Ω , is defined as the frequency of a wave relative to the background wind speed, u_o , and is given by

$$\Omega = \omega - u_o k = (c - u_o)k, \quad (1.12)$$

where ω is the observed wave frequency ($\omega = ck$) and c is the observed phase speed. H_s is the pressure scale height, which is the distance over which the pressure drops exponentially in the atmosphere (6–8 km), and can be ignored if wavelengths are much less than the scale height.

One of the most important results of linear wave theory is the dispersion relation because it relates the wave's angular frequency to the physical properties of the atmosphere and wave structure. The wave motion energy propagates upwards and parallel to the lines of constant phase and perpendicular to the downward phase progression. When $\omega = N$, then $\beta = 0$, the wave propagates horizontally, and the fluid oscillates vertically. When ω/N is very small, corresponding to either low-frequency waves or strong stratification in the atmosphere, β approaches $\pi/2$, the wave propagates almost vertically and the fluid oscillates horizontally.

1.3.3. Wave Dissipation

In order to conserve kinetic energy as a wave propagates upwards, the amplitude

of the wave increases related to the atmospheric scale height as the atmospheric density decreases [e.g. *Gossard and Hooke, 1975*]. These growing wave amplitudes can eventually become too large to remain stable and break. Depending on their amplitude and the prevailing atmospheric conditions, GW tend to break in the stratosphere and MLT region where they deposit their momentum into the background flow. Secondary waves capable of propagating to higher altitudes may be generated by this breakdown process [*Fritts and Nastrom, 1992; Tsuda et al., 1994*].

Additionally, at critical layers, where the background wind velocity, u_o , is equal to the GW horizontal intrinsic phase speed, c_I , in the direction of the motion of the wave, the GW cannot propagate upward anymore. Only GWs with phase speeds greater than the background wind can propagate in the same direction as the wind.

1.3.4. Observations of Waves

Observational studies of GWs in the MLT region consist of measuring their propagation characteristics such as horizontal and vertical wavelengths (λ_h and λ_z), observed period, observed phase speed ($c = \frac{\omega}{k}$), direction or propagation (ϕ), potential energy (PE), momentum flux (MF), as well as local, seasonal, and interannual variability.

Modelling studies show that GWs significantly influence the “composition, structure, background wind, and temperature fields that drive the global circulation system” [*Garcia and Solomon, 1985*]. For example, vertical upwellings in the summer polar region and corresponding downwellings in the winter polar region are largely driven by GW dissipation in the MLT region, which deposits momentum against the mean zonal (East-West) flow, resulting in a residual meridional circulation [e.g., *Andrews et al., 1987*]. Long-term observations of GWs are important in order to quantify the magnitude and location of the variability and investigate their primary causes. Currently, the effects of GWs are usually parameterized in atmospheric cli-

mate models based on our current knowledge and therefore new measurements are always needed to further improve our understanding of their influences [*Richter et al.*, 2010].

1.4. Summary of Chapters

This dissertation presents a study of OH rotational temperature and small-scale GWs in the MLT region mostly using data from Andes Lidar Observatory (ALO), Chile. The primary instrument used in this study, the Utah State University (USU) Mesospheric Temperature Mapper (MTM), is introduced in Chapter 2 together with MTM data products and image analysis techniques.

Chapter 3 introduces ALO, provides background to its establishment and lists key scientific instruments and goals of ALO collaborative observations. The results of an 8 yr climatology study (comprising over 1700 nights) of mesospheric OH temperatures over the Andes Mountains yield new knowledge of seasonal oscillations and tidal influences. Comparisons of nightly mean temperatures and yearly cycles are also made using temperature measurements obtained by the same MTM imager when it was located at Maui, Hawaii during an earlier campaign (2001–2004) [*Zhao et al.*, 2007].

Chapter 4 compares the ground-based mesosphere temperature data set from ALO with concurrent measurements obtained from the Sounding of the Atmosphere by Broadband Emission of Radiation (SABER) instrument on the Thermosphere, Ionosphere, Mesosphere, Energetics and Dynamics (TIMED) satellite [*Remsberg et al.*, 2008]. Coincidence criterion are discussed, as well as effects of measurement biases due to different data acquisition techniques.

Chapter 5 uses MTM temperature variance observations as a measure of GW activity, and discusses the contribution of different scale-sizes of waves to the total seasonal variance. Vertical temperature profiles obtained by SABER are used to

study of GW PE revealing enhancements during the winter months.

Chapter 6 discusses the formation and properties of mountain waves and how they propagate into the MLT region. An established measurement technique is used to identify and measure the properties of 37 mountain wave events observed during six consecutive winter seasons (2012–2017). Conditions in the lower atmosphere that allow the propagation of mountain waves into the MLT region are investigated in coordination with mesospheric wind conditions.

Chapter 7 summarizes the results of this dissertation research and discusses possible future research.

CHAPTER 2

THE MESOSPHERIC TEMPERATURE MAPPER

2.1. Introduction

Ground-based observations provide a practical and cost-effective technique for remote sensing of GW perturbations in the MLT region. Photometers, interferometers, and spectrometers have been widely used to obtain one-dimensional measurements of GWs in the hydroxyl (OH) Meinel band emission intensity and related rotational temperatures at ~ 87 km altitude [e.g., *Bittner et al.*, 2002; *Burns et al.*, 2003; *French et al.*, 2000; *Greet et al.*, 1997; *Liu et al.*, 2015; *Meriwether*, 1975; *Noll et al.*, 2016; *Offermann and Gerndt*, 1990; *Scheer and Reisin*, 1990; *Semenov et al.*, 2013; *Takahashi et al.*, 1994]. With the development of highly sensitive CCD detectors in the 1990s, observations have naturally expanded to include imaging studies of the GW field. All-sky imaging measurements of OH emissions provided wide-field two-dimensional measurements of the small-scale short-period GWs [*Kam et al.*, 2017; *Pautet et al.*, 2018; *Taylor*, 1997; *Taylor and Garcia*, 1995]. Modern imaging instruments are capable of observing mesospheric GWs over a 180° field of view (FOV) to cover a large geographic area ($\sim 5 \times 10^5$ km²) using an all-sky optical arrangement. Narrowband filters are used to image several different airglow emissions using a computer-controlled filter-wheel system. Each filter is successively exposed to the night sky enabling the GWs in the different airglow emissions to be sequentially imaged. To date, these systems continue to provide important information for determining GW characteristics and climatology from numerous sites around the world.

2.2. The MTM

The USU Mesospheric Temperature Mapper (MTM) is a high-performance solid-state imaging system, as shown in Figure 2.1a. It was designed and tested at USU

in 1996 with funding from the NSF CEDAR (National Science Foundation Coupling, Energetics, and Dynamics of Atmospheric Regions) program as part of an initiative to develop new instrumentation for the twenty-first century for upper atmosphere research. The MTM differs from typical airglow imaging instruments as it is capable of precise measurements and mapping of both the intensity and rotational temperature fields of the NIR Hydroxyl OH (6,2) and molecular oxygen O₂ (0,1) airglow emission layers (see Section 1.2). Specifically, it was designed with a smaller FOV, $\sim 90^\circ$, as shown in Figure 2.1b, to quantify short-period mesospheric GW signatures [Pendleton Jr et al., 2000; Taori et al., 2005; Taylor et al., 2001].

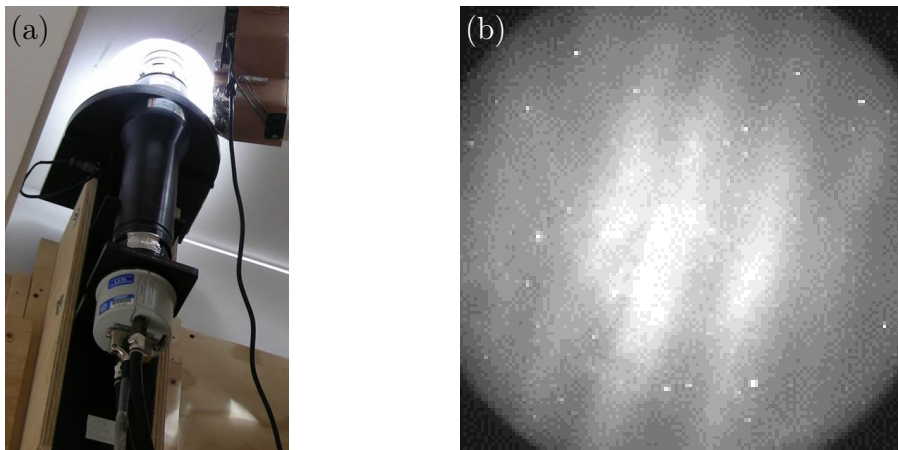


Figure 2.1. The MTM imaging system and example image. (a) MTM imager with wide-field lens at top, followed by filter wheel and telecentric lens system. CCD imager and cooling pipes are positioned at bottom [Courtesy M.J. Taylor]. (b) An example image from the MTM taken 8 July 2012.

The MTM takes advantage of enhancements in the performance of large-area back-thinned CCD arrays that feature exceptionally high-quantum efficiencies (up to 80% at NIR wavelengths) coupled to a wide-angle Keo Consultants telecentric lens system (90° FOV). Figure 2.2 shows a schematic diagram of the optics used to

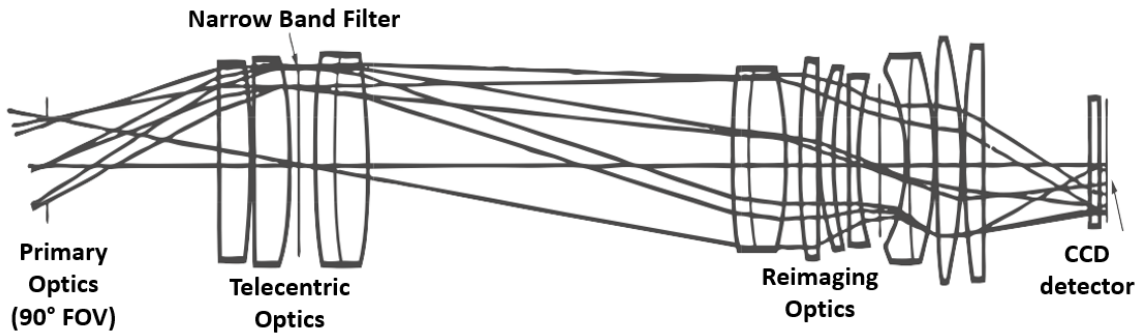


Figure 2.2. Schematic diagram showing the MTM imager and its specialized optics [Courtesy R. Eather, Keo Consultants].

obtain the wide FOV needed by the MTM. The MTM provides airglow intensities (measured in photon counts) and wave data similar to other imagers, but also enables computation of the temperature field at OH and O₂ altitudes over a substantial region ($\sim 1.8 \times 10^4$ km²). Thermal noise is minimized by cooling the detector to -50° C using a two-stage Peltier system aided by a closed-cycle liquid refrigeration unit [Pendleton Jr et al., 2000; Taylor et al., 2005].

The MTM has performed exceptionally well with over 20 years of operation to date, including ~ 5 years of coordinated observations at the Air Force Maui Optical Station, Hawaii (20.8° N), as part of the NSF Maui MALT program to investigate GWs alongside different lidar systems, as well as observations at Fort Collins, Colorado, Star Fire Optical Range, New Mexico, and Bear Lake Observatory, Utah [e.g., Simkhada et al., 2009; Taori and Taylor, 2006; Taori et al., 2005; Taylor et al., 1999; Zhao et al., 2005, 2007]. Since 2009, the MTM has operated at Cerro Pachón, Chile (30.3° S) as part of the ALO program. The MTM has obtained an 8-yr (and growing) data set that is used extensively in this dissertation to study characteristics of small-scale GW events over the Andes Mountains [e.g., Cao et al., 2016; Fritts et al., 2014a; Hecht et al., 2014, 2018; Liu et al., 2016; Vargas et al., 2016; Walterscheid

et al., 2015].

More recently, a new successor instrument, known as Advanced Mesospheric Temperature Mapper, has been designed and built by USU and the Space Dynamics Laboratory and deployed in Scandinavia, Alaska, Bear Lake, Antarctica and New Zealand [e.g., *Bossert et al.*, 2014, 2017; *Cai et al.*, 2014; *Fritts et al.*, 2014b, 2016; *Pautet et al.*, 2014, 2016, 2018; *Yuan et al.*, 2014, 2016].

2.3. MTM Data Acquisition

Images are sequentially taken using a temperature-stabilized set of narrow-band filters ($\Delta\lambda \simeq 1.2$ nm) centered on the $P_1(2)$ and $P_1(4)$ emission lines of OH (6,2) Meinel Band at 840 nm and 846.5 nm, respectively, and at 866 nm and 868 nm for the O_2 (0,1) atmospheric emission. The filter wheel rotates and observes each of the four emission lines sequentially for 60 s followed by a background sky measurement, resulting in a cadence of ~ 5.5 min. Further details of the filters used for observations are presented in Table 2.1. A *dark* image, when the shutter remains closed, is taken every 32 cycles. The camera operates automatically from dusk to dawn (for solar depression angles $< 12^\circ$) for approximately 22 nights each month (centered on the new moon period). Data are stored as "TIFF" images locally on a computer drive and are downloaded at regular intervals to USU for analysis.

In order to obtain a larger signal-to-noise ratio (~ 80 - 100 :1) necessary for precise temperature measurements, the image data are 8×8 binned. This results in a decrease in spatial resolution from the original 1024×1024 pixels to 128×128 "superpixels" [*Pendleton Jr et al.*, 2000; *Taylor et al.*, 1999]. Each superpixel has a footprint of 0.9×0.9 km at the OH layer height and the total image has a FOV of 1.8×10^4 km². This is sufficient to resolve short-period small-scale GWs with horizontal wavelengths < 100 km.

Table 2.1. Characteristics of MTM Filters Used For Airglow Observations at ALO.

Airglow emission	Optical filter	
	Peak λ (nm)	Bandwidth (nm)
P ₁ (2) line of OH (6,2) band	840.0	1.20
P ₁ (4) line of OH (6,2) band	846.5	1.20
O ₂ (0,1) band	866.0	1.20
O ₂ (0,1) band	868.0	1.20

2.4. MTM Data Processing and Derivation of Temperature

In order to perform further analysis including derivation of OH rotational temperatures and retrieval of GW parameters, additional image processing steps are required. The MTM image data are processed using software developed at USU. An example of a raw P₁(2) image taken on 9 July 2012 is shown in Figure 2.3a. The first step is the removal of background stars from the images (see Figure 2.3b). This is done by the software identifying and replacing sharp, localized intensity spikes in individual pixels with an interpolated value from the surrounding pixels [*Garcia et al.*, 1997]. This works well for removing stars and hot pixels in the CCD chip. The presence of the Milky Way, as it passes through the images, is accounted for using the background images and is subtracted from the band intensity calculations.

Next, the images require flat fielding, spatial calibration, and unwarping. Flat fielding is the process of removing unwanted variations in the background intensity of the images by subtraction. A mean flat-field image is made for each night. This enables the removal of bright features in the background images, brightness enhancements at the edges of the images due to the van Rhijn effect, and lens effects such as vignetting (see Figure 2.3c). Spatial calibration uses the known star field

to map the original image to standard coordinates aligning due North to the top. Unwarping relates the distance between pixels in the image to the actual physical distance. It transforms the images into a final geographic coordinate system with a two-dimensional uniformly-spaced 150×150 km grid at the airglow layer height. Therefore, the azimuth or direction of propagation of the waves, ϕ , is measured in degrees clockwise from North. The result of this process is shown in Figure 2.3d. For further detail on image processing see *Hapgood and Taylor [1982]* and *Garcia et al. [1997]*.

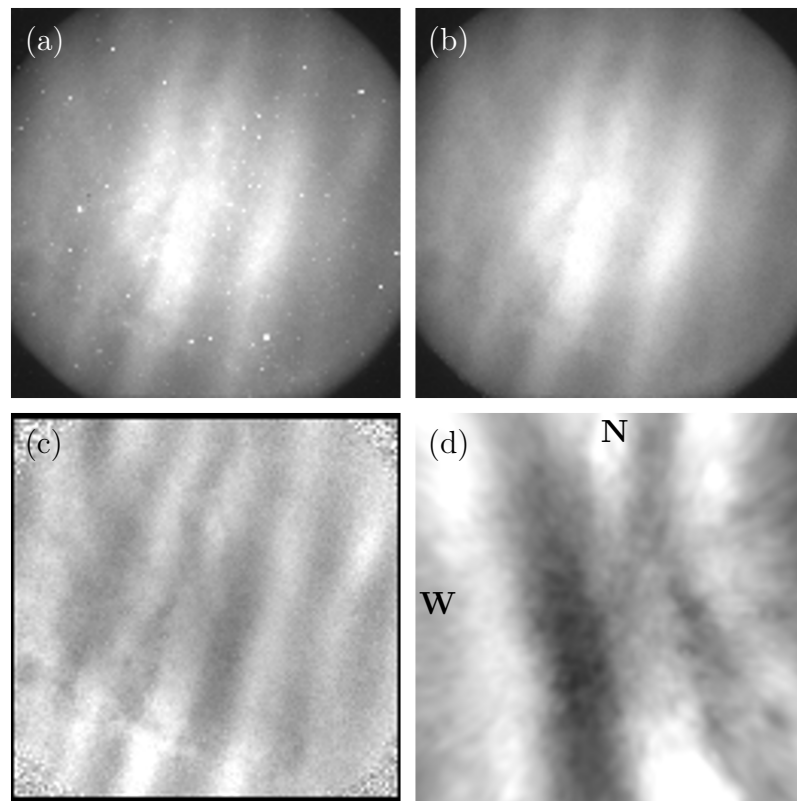


Figure 2.3. Image processing steps for an example image taken on 8 July 2012. (a) Raw image, (b) image with stars removed, (c) flat fielded image, (d) calibrated, unwarped, and enlarged image.

Relative intensity measurements of the selected OH emission lines, along with the background emission (as shown in Figure 2.4), are used to determine absolute

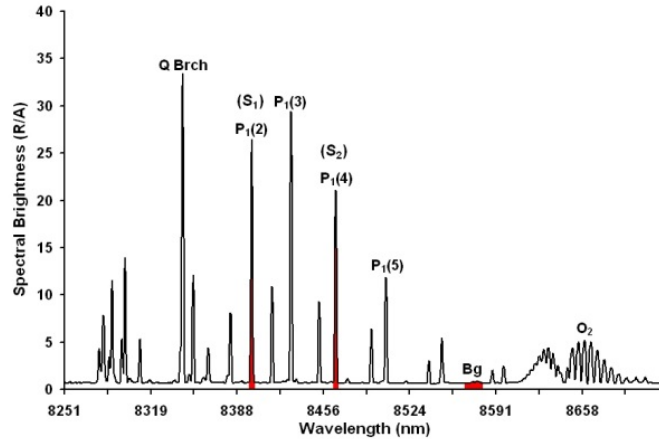


Figure 2.4. Emissions given by different OH (6,2) vibrational transitions. The ratio of the $P_1(2)$ to $P_1(4)$ emissions (highlighted in red) is used to measure T_{OH} [Courtesy M.J. Taylor.].

OH rotational temperatures, T_{OH} , with high precision ~ 1 – 2 K. This is done using the well-established ratio method [Goldman *et al.*, 1998; Meriwether Jr, 1984] as described by the equation 2.1:

$$T_{OH} = \frac{228.45K}{\ln \left[2.810 \frac{P_1(2)}{P_1(4)} \right]} \quad (2.1)$$

where $P_1(2)$ and $P_1(4)$ are the intensity counts of the individual emission lines. Derivation of the rotational temperature was done separately for the OH and O_2 emissions. For the OH measurements, a value of 1.300 was used for the ratio of transition probabilities [Pendleton Jr and Taylor, 2002].

Assuming local thermodynamic equilibrium (LTE) conditions, the derived rotational T_{OH} should be similar to the atmospheric kinetic temperature. Previous comparisons of the MTM OH and O_2 rotational temperatures with other well calibrated instruments, including a Na lidar, have shown that our nocturnal mean temperatures, referenced to 87 km and 94 km respectively, are accurate to ± 5 K [Pendleton Jr *et al.*,

2000; Zhao *et al.*, 2005]. These results are reaffirmed in Figure 2.5 which shows MTM OH temperature, T_{OH} , data (black line) for the night of 14 August 2010 with several temperature measurements from the Na lidar at 87, 88, and 89 km altitudes (red, blue, and green lines, respectively). Further instrument comparisons will be discussed in subsequent Chapter 3 and 4. The stability and high linearity of the MTM provides capability for long-term studies of mesospheric temperature variability.

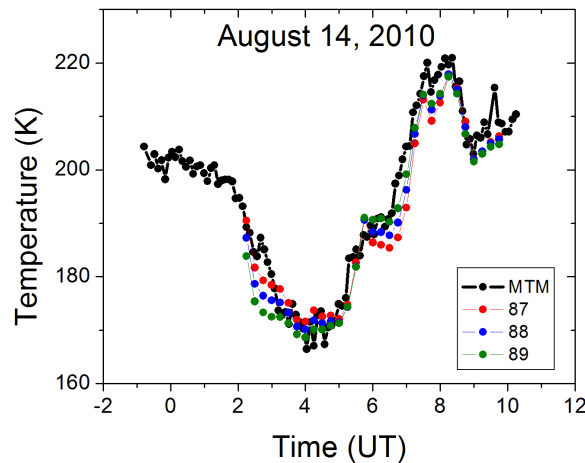


Figure 2.5. MTM OH temperature data for 14 August 2010 (black line) and several temperature measurements from the Na lidar at 87, 88, and 89 km altitudes (red, blue and green lines) [Courtesy Y. Zhao].

2.5. Zenith Temperature

To measure temporal variability useful for investigating larger-scale wave events and long-term climatological studies, only the central 5×5 superpixels of the array are used referred to as the “zenith temperature” measurements. This provides a zenithal footprint of about $4.5 \text{ km} \times 4.5 \text{ km}$ at 87 km. This data format is similar to those obtained from photometers, interferometers, spectrometers, and lidars. The intensity of the center superpixels (zenith) of each of the $P_1(2)$ (black line), $P_1(4)$ (grey line), background (green curve) are recorded and shown for the example night

of 2–3 November 2016 in Figure 2.6a. Perturbations in the intensities are signatures of wave activity and can be seen in the $P_1(2)$ and $P_1(4)$ lines. The zenith OH rotational temperature, T_{OH} (blue circles), and OH band intensity, I_{OH} (red squares), derived using Equation 2.1 for this night, are shown in Figure 2.6b. Both large-scale and small-scale GW signatures can be seen. These measurements are recorded and used to investigate GW activity and longer-term variations. For example, the mean I_{OH} for this night is $(59 \pm 5) \times 10^3$ counts and the mean T_{OH} is 191 ± 4 K for the night, where the ± 4 K is the standard deviation representing nightly temperature variation induced by the waves.

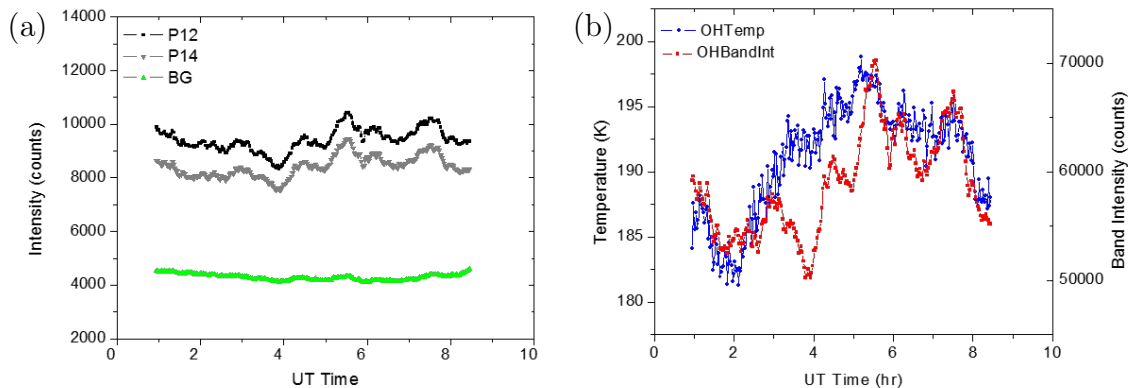


Figure 2.6. Measurements made by the MTM on the night of 2–3 November 2016. (a) Raw intensity measurements in total counts. The OH $P_1(2)$, $P_1(4)$ line intensities (black and grey, respectively) show wave activity. The background sky intensity is the green curve. (b) Derived I_{OH} measurements (red) and T_{OH} measurements (blue) for the same night. Both large-scale (large curve in blue) and small-scale GW (1-h period more pronounced in red) signatures are present.

2.6. Temperature Map

The primary advantage of the MTM over other imaging systems is its ability to measure the OH (and O_2) rotational temperatures at every pixel in the image. Once the images are flat-fielded, calibrated and unwarped as mentioned earlier, two

new maps are created: a rotational temperature map and a band intensity map characterizing the GW field at the airglow layer altitudes.

Figure 2.7a shows an example OH band intensity map at 2337 UT and Figure 2.7b shows the temperature map (averaged over several images) observed on 8 July 2012 UT from ALO, Chile (30.3°S, 70.7°W). The temperature scale ranges from 180–200 K as shown by the color bar. The white pixels denote regions above 200 K. Changes in the measured T_{OH} are caused by the propagation of GWs through the OH layer. Clearly visible in both images are large wave peaks due to GWs.

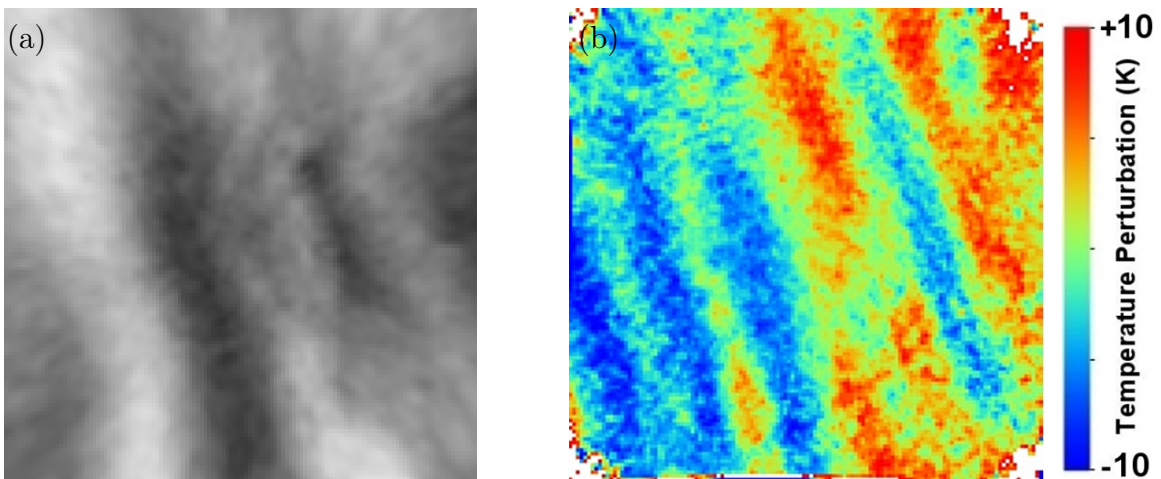


Figure 2.7. (a) Processed OH (6,2) relative band intensity map taken at 2337 UT and (b) averaged rotational temperature map [Courtesy P.D. Pautet] taken from ALO (30.3°S) on 8 July 2012. In both images, perturbations induced by propagating GWs throughout the OH layer are clearly visible.

2.7. Keogram Representation

Keograms were first used to summarize the occurrence and motions of various auroral forms during the course of a night [Eather *et al.*, 1976, 1979]. They are created by placing narrow slices (two pixels wide) from each image side by side to create a time series as shown in Figure 2.8. Four sequential OH intensity images are shown

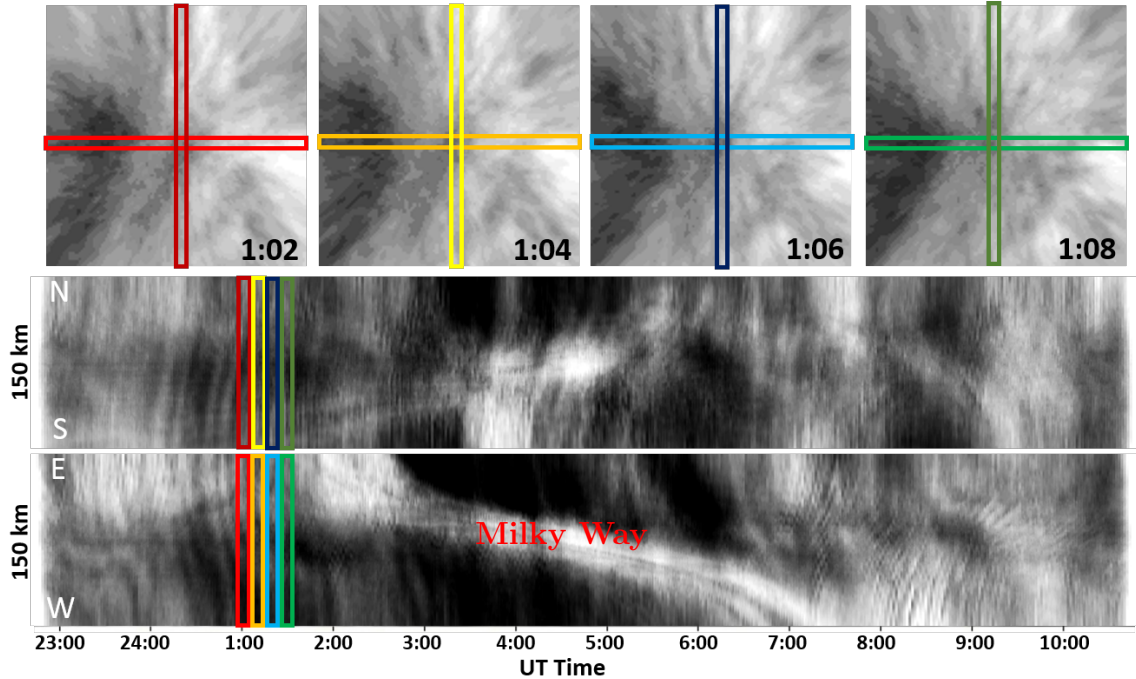


Figure 2.8. Keogram creation process for the night of 22–23 June 2012. Four consecutive OH intensity images (top) with vertical and horizontal slices used to create the N-S (center) and E-W (bottom) keograms.

on the top row of Figure 2.8 for the night of 22–23 July 2012. Sequential vertical slices provide a North-to-South (N-S) evolution of the MLT wave field during the night (center plot), while the horizontal slices provide the East-to-West (E-W) strip (bottom plot) in Figure 2.8. The four individual images (top plots) have dimensions of 150×150 km at the OH layer altitude, therefore the y -axis of the keograms is the distance of 150 km and the x -axis is time, measured to be ~ 11.7 h for the night shown in this example. Both keograms show strong evidence for extensive small-scale GWs throughout the night. They also show evidence for a larger-period coherent wave (45–50 min) that also existed throughout the night. The slowly rotating Milky Way also shows up in the keograms (particularly in the E-W keogram) as an elongated bright curved structure.

Filtering the keograms can more clearly identify the wave structure. For example, the small-scale features evident in Figure 2.8 can be further enhanced by applying a 5–60 min bandpass filter, as shown in the top of Figure 2.9 which clearly identifies the extensive ~ 50 min periodic wave with superposed smaller scale waves throughout the night. This periodicity is also evident in both the zenith OH rotational temperature (blue) and band intensity (red) plotted in Figure 2.10. By applying >60 min filter, the larger-scale waves can be seen in the intensity data (seen as light and dark patches in the bottom of Figure 2.9). Note: the large-scale GWs and tidal harmonics are not detectable in a single image because their horizontal wavelengths are significantly larger than the imager FOV, hence the use of keograms in their identification.

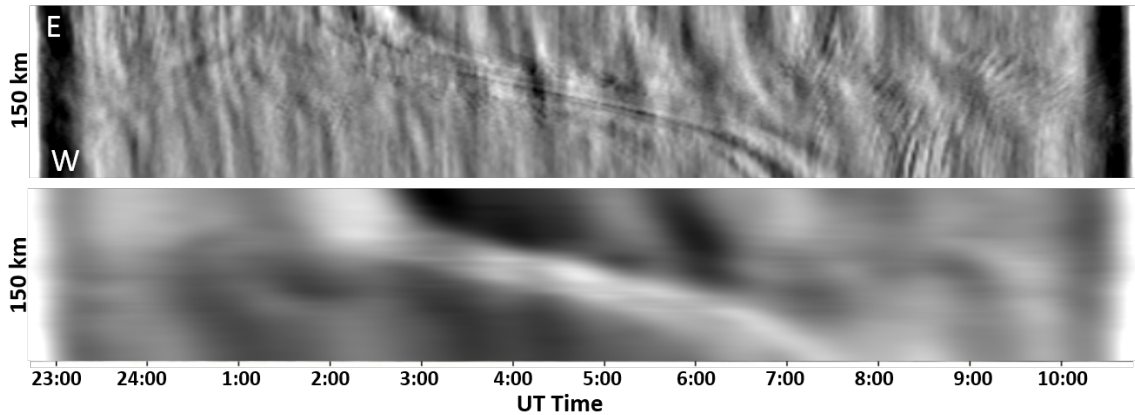


Figure 2.9. E-W OH band intensity keograms with 5–60 min (top) and >60 min bandpass filters applied (bottom) for the night of 22–23 June 2012.

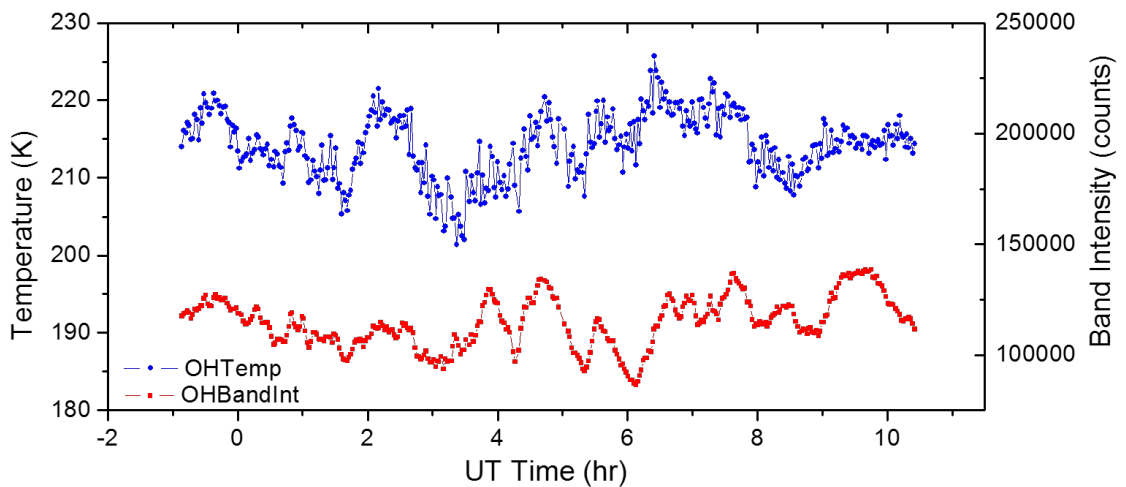


Figure 2.10. Zenith OH rotational temperature (blue) and band intensity (red) for 22–23 June 2012 showing the same small-scale GW signature as the top of Figure 2.9.

Once correctly interpreted, keograms are extremely useful in quickly identifying clear nights, small-scale GWs, much larger GW (a few to several hours) and tidal-scale signatures. In Chapter 6, keograms will also be used for identifying quasi-stationary mountain waves.

2.8. Spectral Analysis

Spectral analysis techniques are commonly used to determine the frequency (and period) of small-scale GWs that are prevalent in the image data (e.g., Figure 2.7). Fourier analysis, based on the sinusoidal basis functions, easily determines the wave parameters and is the standard image processing procedure on airglow imager data sets [Coble *et al.*, 1998; Garcia *et al.*, 1997; Vargas *et al.*, 2016]. The use of Fourier analysis requires data sets with equally spaced time intervals. This works well on individual nights with continuous clear skies. When data points are missing through the night due to cloud, interpolation may be used [Press, 2007]. This study focuses on the wealth of continuous nightly data obtained during the ALO program with only occasional small gaps.

To determine the horizontal wavelength, λ_H , and the direction of propagation (or azimuth) of a small-scale GW event a “region of interest” is first selected containing several wave crests. A 2-D FFT spectral analysis is performed on a sequence of individual images. The FFT converts the image’s spatial domain into the frequency domain resulting in a symmetric periodogram with complex magnitudes revealing the wavelength and direction of propagation as shown in Figure 2.11.

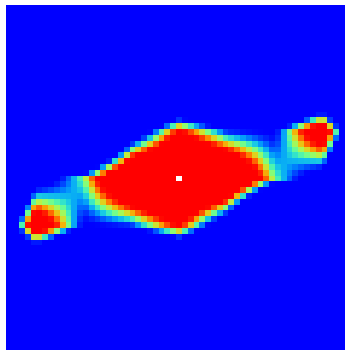


Figure 2.11. Result of 2-D FFT spectral analysis of intensity image of Figure 2.7a showing the symmetric spectrum from which ϕ and λ_H are obtained (dimensions are in frequency, axes not shown).

The apparent phase velocity, $c = \frac{\Delta x}{\Delta t}$, of the wave is determined by measuring the

horizontal displacement, Δx , of selected wave crests in several images over time, Δt . These measurements are repeated several times throughout the duration of individual GW events to obtain average wave characteristics. The duration of individual GW events is determined using movie clips of the image data.

For example, the FFT analysis performed on Figure 2.7a yields a ϕ of $259^\circ \pm 5^\circ$ (towards the Southwest), λ_H of 48 ± 3 km, and an observed horizontal phase speed, c , of 3 ± 5 m s⁻¹. These values are typical of the mountain waves observed at ALO (see Chapter 6). Additionally, the mean temperature was found to be 208 ± 2 K, with a wave amplitude of 9 ± 1 K.

2.9. Summary

The MTM is a CCD imager developed at USU with funding from the CEDAR program. It has operated for almost 20 years at several low- and mid-latitudes sites since its construction in 1996 to study the upper atmosphere.

The MTM has a 90° FOV which corresponds to a region of about 150 km in diameter at 87 km. Along with measuring small-scale GW parameters, the MTM is capable of studying GW induced T_{OH} variability in the NIR OH emission layer. The T_{OH} is derived using the OH (6,2) rotational band intensity ratio of the P₁(4)/P₁(2) emission lines.

Novel temperature maps provide two-dimensional information of temperature perturbations in the OH layer. With the use of keograms, small-scale and large-scale waves (including mountain waves) can be readily identified and characterized (see Chapters 5 and 6). Intensity keograms are better suited for detection of waves, while temperature measurements provide their perturbation amplitudes. Well-developed 2-D FFT spectral analysis is used to determine wave propagation parameters.

Zenith OH temperature measurements provided by the MTM are useful for studying the seasonal, annual, and long-term climatology of the mesosphere and for compar-

isons with other instruments; both ground-based (see Chapter 3) and satellite-borne (see Chapter 4).

The following chapters use these tools to investigate GWs and mesospheric temperature variability over the Andes ranging from individual events to seasonal time scales.

CHAPTER 3

MESOSPHERIC TEMPERATURE CLIMATOLOGY OVER THE ANDES

3.1. Early Campaigns

Early campaigns using a suite of ground-based and airborne instruments to study the dynamics of the MLT region were the Airborne Lidar and Observations of the Hawaiian Airglow (ALOHA-90) campaign and a few years later the ALOHA/ANLC-93 campaign. A broad range of results were reported in several papers in special sections for ALOHA-90 (Geophysical Research Letters, 18(7), 1991) and ALOHA-93 (Geophysical Research Letters, 22(20), 1995; Journal of Geophysical Research, 103(D6), 1998) [e.g., *Gardner et al.*, 1991; *Hecht and Walterscheid*, 1991; *Hickey et al.*, 1998; *Kane et al.*, 1991; *Lowe and Turnbull*, 1995; *Swenson et al.*, 1995; *Swenson and Mende*, 1994; *Taylor and Edwards*, 1991; *Taylor and Hill*, 1991; *Taylor et al.*, 1995a,b,c,d,e].

The tremendous success of these programs stimulated a joint research initiative, the Maui Mesosphere and Lower Thermosphere (Maui MALT) program between the NSF and the U.S. Air Force Office of Scientific Research (AFOSR). Joint measurements were conducted from the Air Force Maui Optical Station at the summit of Haleakala Crater, Maui, Hawaii (20.8°N, 156.2°W, 2970 m) to provide a more extensive ground-based seasonal observing program over a 5-yr period [*Swenson*, 2005]. As part of Maui MALT, the USU MTM operated from November 2001 to December 2006, providing detailed information on GWs and mesospheric temperature variability. These measurements were complemented by coincident observations of mesospheric wind and temperature observations using the University of Illinois at Urbana-Champaign (UIUC) Na Doppler Lidar, and from May 2002 observations of the MLT wind field using the UIUC Meteor-wind Radar co-located at Maui, Hawaii. Together

these data enabled detailed investigation of the dynamic structure of the MLT including GWs, tides, and planetary waves. In addition, analysis of the spatial and temporal features of the wind and temperature fields of the tropical mesosphere, and measurements of the vertical fluxes of momentum transported by small-scale waves were made. Observations and results were reported in a series of papers (Journal of Geophysical Research, 110(D9), 2005).

In addition, long-term observations during the Maui MALT campaign using the MTM have revealed annual oscillations (AO) and semiannual oscillations (SAO) of mesospheric temperatures [Taori *et al.*, 2005; Taylor *et al.*, 2005; Zhao *et al.*, 2005, 2007]. The suite of instruments at Maui also provided correlated measurements using Na lidar, meteor-wind radar, and the MTM [Liu and Gardner, 2005; Tang *et al.*, 2005], of observed small-scale GW propagation [Simkhada *et al.*, 2009], instabilities [Hecht *et al.*, 2005; Larsen *et al.*, 2004; Li *et al.*, 2005], mesospheric bores [Seyler, 2005], and initial measurements of GW momentum flux [Liu and Gardner, 2005; Tang *et al.*, 2005].

3.2. Andes Lidar Observatory

Building on the success of these measurement programs, the Andes Lidar Observatory (ALO) was established and started observations of the MLT region in August 2009 (see Figure 3.1). The ALO consists of a small purpose-built observatory located near the Cerro Pachón Observatory (30.3°S, 70.7°W, 2530 m) high in the Andes Mountains in northern Chile. This site provides excellent facilities for studying GWs, seasonal variability and climatology of the MLT region.

The location of ALO is important for mesospheric GW studies because it provides data in a geographic area that is poorly characterized, namely the low-latitude Southern Hemisphere. Cerro Pachón is also the location of the GEMINI South and Southern Astrophysical Research telescopes managed by the Association of Universi-

ties for Research in Astronomy. It provides excellent year-round viewing conditions (~ 300 clear nights per year), high elevation, and existing infrastructure and personnel support for occasional maintenance of the MTM. ALO's location in the Andes Mountain Range in a continental region also provides contrasting data with that obtained from the Maui MALT investigation which was conducted over a single peak in the central Pacific Ocean.

The Southern Hemisphere has fewer observational sites than the Northern Hemisphere, particularly those equipped for measuring the airglow emissions. For example, *Semenov et al.* [2013] summarized nine sites in the Southern Hemisphere versus 27 sites in the North. Therefore, the addition of a new ground-based temperature data set from the Southern hemisphere is useful. The location of ALO was chosen to investigate the dynamics and wave phenomenology of the MLT, specifically the influence of terrain-generated waves due to strong convective activity over the nearby coastal waters, the extreme dryness of the area, and the region's steep terrain. These attributes make it a prime location for the generation and observation of GWs over a wide range of frequencies, including stationary mountain waves [*Walterscheid and Hickey, 2005*].

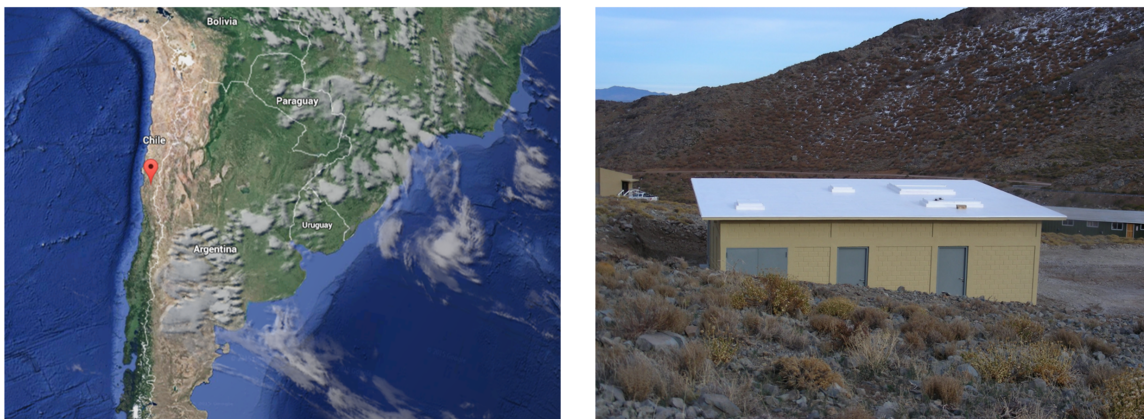


Figure 3.1. The Andes Lidar Observatory (right image) is located (red marker on map) in the Chilean Andes Mountains of South America (30.3°S , 70.7°W , 2530 m). This purpose-built facility has multiple roof hatches for nighttime observations using lidar and other instruments.

A suite of instruments similar to those used in Hawaii was funded by a NSF collaborative grant for operation from ALO. These included the Na wind-temperature lidar, a meteor-wind radar, an all-sky airglow imager, and a multi-channel photometer all operated by UIUC, and an Aerospace Infrared Camera, along with our established MTM. The measurement of mesospheric temperatures is particularly important for quantifying the dynamics of the MLT region over this new site.

3.3. ALO MTM Operations

As discussed in Chapter 2, the USU MTM is capable of precise measurements of the brightnesses (measured in photon counts) and rotational temperatures of the NIR Hydroxyl OH and molecular oxygen O_2 airglow emission layers which occur at peak altitudes of ~ 87 km and ~ 94 km, respectively [Taori *et al.*, 2005; Taylor *et al.*, 2001]. For the first ~ 25 months, joint OH and O_2 intensity, and temperature measurements were recorded (August 2009–November 2011). However, due to a filter failure, the O_2 measurements were curtailed in early November 2011. Subsequently, the OH cadence time was reduced from the initial ~ 6 min to ~ 2 min, and the OH exposure times

were decreased to 30 sec based on the high quality of the data. The sum effect was to enhance the GW temporal resolution increasing the temperature measurements to over 30 samples/h with only limited effects on the temperature sensitivity, as shown later in Figure 3.3.

The imager operates automatically for up to 12 h (depending on the season) from dusk to dawn (for solar depression angle $\geq 12^\circ$) for approximately 22 nights each month (centered on the new moon period). At the beginning and end of each night the intensity measurements are limited by strong twilight. This creates a "bath tub" shape to the intensity versus time data (shown in Figure 3.2a). These strong twilight data points are removed. Data are stored at ALO on a computer drive and are downloaded at regular intervals to USU for analysis (by me). Quick-look data using only the central 5×5 superpixels of the array were used for temperature and intensity measurements for each night. These data have been used for calibration and collaborative studies with Na temperature lidars, Fourier spectrometers, and both narrow and all-sky imagers; all of which take measurements centered on the zenith [e.g., *Hecht et al.*, 2018; *Liu et al.*, 2016; *Vargas et al.*, 2016]. Based on typical OH emission levels measured at ALO, the precision of the MTM emission intensity data is better than 0.5% for an individual image and the temperature precision was determined to be ~ 2 K (in 2 min) for the derived OH rotational temperatures. Comparative measurements of the OH rotational temperatures as measured by the MTM are in agreement with measurements of the on-site Na wind-temperature lidar (Figure 2.5). Since its early operations in 2009, I have been responsible for the remote operation, data processing, and analysis of the ALO MTM data set.

3.4. MTM Nightly Data

This section presents selected example data to illustrate the high quality and diversity of the MTM data regularly obtained from ALO during its >8 yr of operation.

The stored “.TIFF” images are processed and analyzed as discussed in Section 2.4 using software developed at USU. Figure 3.2 shows nine example nights: 19 September 2009, 12 June 2010, 8 March 2011, 2 July 2011, 23 May 2012, 12 February 2013, 25 August 1014, 15 July 2005 and 3 November 2016. The intensity of the zenith 5×5 superpixels of each of the $P_1(2)$ (black curve), $P_1(4)$ (grey curve), background (green curve) and dark images (blue curve) are shown. The first four panels also include the O_2 866 nm and 868 nm line data (red and pink lines, respectively) for comparison. The higher temporal resolution due to the removal of the O_2 filters can be seen in the remaining panels. Due to reduction from 1 min to 30 sec of the integration time of the OH emission line exposures the corresponding image brightness measured by photon counts is reduced by a factor of approximately two. Note that the x -axes are in UT which is off from local time depending on day-light savings, meaning local midnight is at 04 UT during the winter months and at 03 UT during the summer months.

The nine panels in Figure 3.2 illustrate the diversity in the nocturnal data. Large-scale, as well as frequent small-scale, GW activity can be seen in both the OH and O_2 emission data. Several panels show peaks in the background intensity (green curve) which is due to the presence of the Milky Way as it passes through the center pixels of the image. Background subtraction of this signal minimizes the impact on the band intensity and rotational temperature calculations. The dark image (flat blue curve) is the photon count of the CCD when the shutter stays closed and is used to monitor the temperature stability of the measurement.

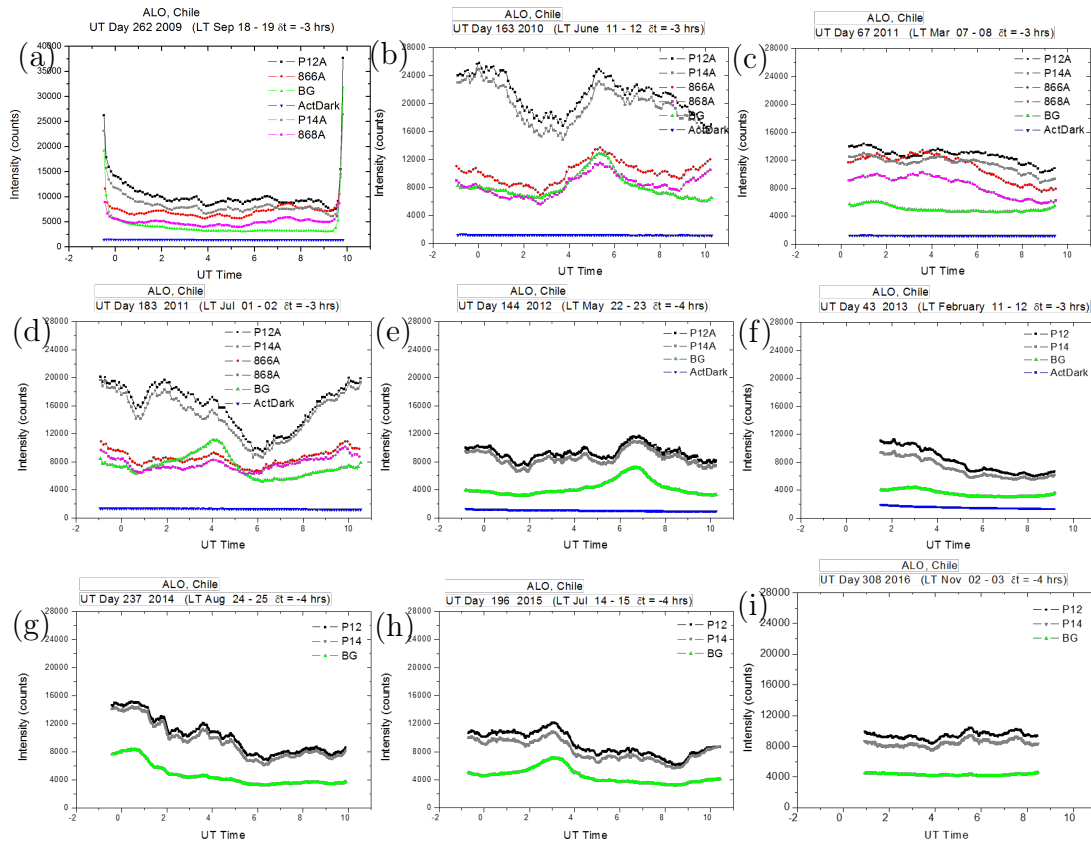


Figure 3.2. Plots showing the raw intensity measurements in total counts for nine nights throughout the program. The $P_1(2)$ to $P_1(4)$ line intensities (black and grey curves, respectively) show wave activity. The background sky intensity is the green curve and the dark image intensity is the blue curve. The first 4 plots include O_2 atmospheric band P branch intensities at 866 and 868 nm (red and pink curves, respectively). Subsequent OH plots were made at a higher temporal cadence of ~ 2 min.

Figure 3.3 shows the derived OH temperatures and intensities for the same nights as shown in Figure 3.2. Each plot uses the same temperature range (50 K), but centered on the mean nocturnal value, for direct comparison of the nights. These plots clearly show

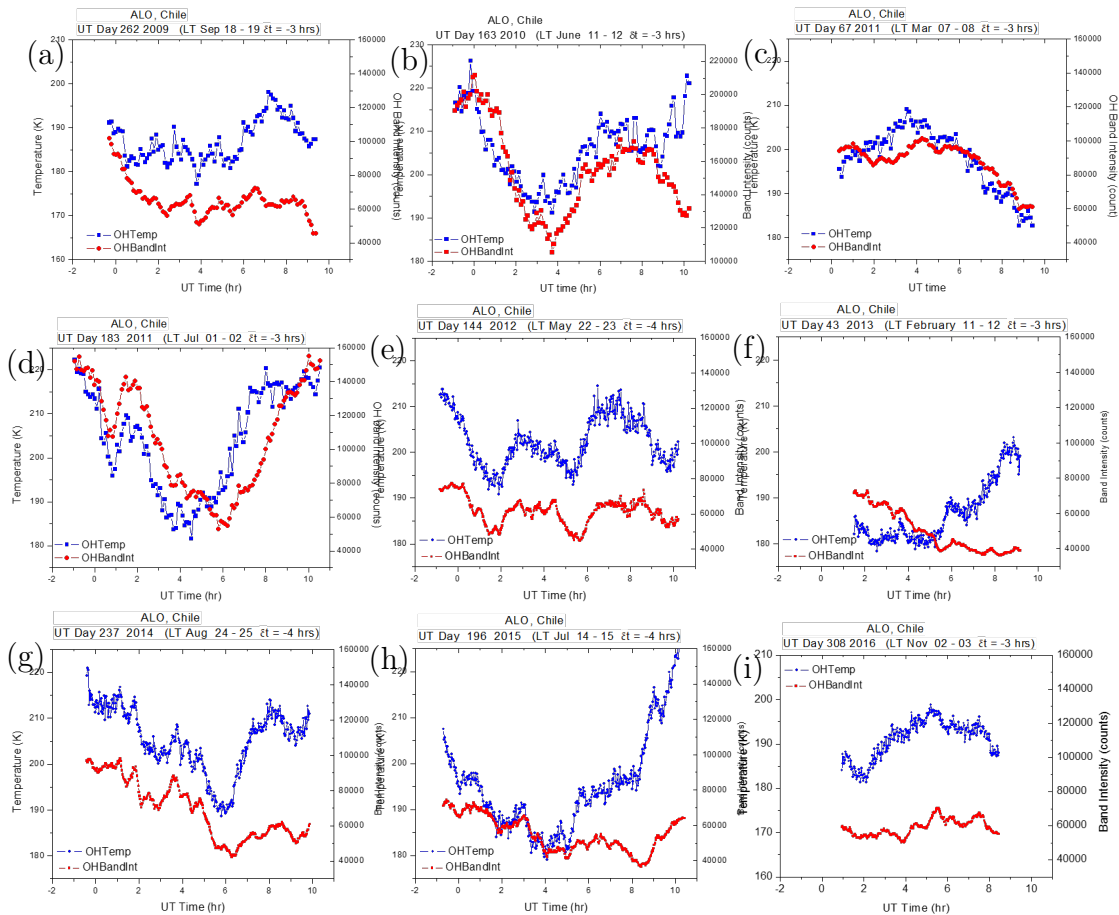


Figure 3.3. OH band intensity (red) measurements with derived OH rotational temperature (blue) for the same nights as in Figure 3.2. Large-scale tide-like signatures are ever present, as well as smaller-scale GW signatures.

the diversity in the GW signatures, periodicities, coherence, and amplitude in both the band intensity and temperature data. On some nights, large-scale tide-like signatures are visible (e.g., Figures 3.3b, c, d, f, g, h), while other nights show medium-scale GW features (e.g., Figures 3.3e, g), and most nights show small-scale GWs superposed on the other signatures (e.g., Figures 3.3a, e, g, h, i). Typical wave periods range from a few tens of minutes to several hours (limited by the length of the nighttime observations). The mean OH band intensity and rotational temperature measurements for each night are given in Table 3.1, where n is the number of images. These

Table 3.1. OH Band Intensity and OH Rotational Temperature Nocturnal Averages for Nights in Figure 3.3.

Year	UT day	Date	\bar{I}_{OH} ($\times 10^3$ count)	\bar{T}_{OH} (K)	n
2009	262	Sep 18–19	65 ± 10	187 ± 5	94
2010	163	Jun 11–12	155 ± 26	206 ± 8	107
2011	67	Mar 07–08	88 ± 11	198 ± 7	87
2011	183	Jul 01–02	107 ± 31	204 ± 12	110
2012	144	May 22–23	61 ± 8	202 ± 5	382
2013	43	Feb 11–12	50 ± 12	187 ± 7	265
2014	237	Aug 24–25	69 ± 17	205 ± 7	355
2015	196	Jul 14–15	55 ± 10	196 ± 11	384
2016	308	Nov 02–03	59 ± 5	191 ± 4	259

example measurements illustrate the rich dynamics and broad spectrum of waves that are ever-present over the Andes. Chapter 6 investigates a subset of these wave termed mesospheric mountain waves generated by strong wind forcing over the steep Andes Mountains.

3.5. Investigating Seasonal Trends at ALO

This section uses the large ALO database to investigate seasonal variability in the nocturnal mean temperatures. To date, over 1700 nights of quality data have been collected from ALO over a 101-month period from August 2009 through December 2017 (spanning 8 consecutive years), including 449 nights of O₂ measurements. Further measurements are currently being made at ALO but have yet to be incorporated in this analysis. This extensive data set provides novel detailed information for investigating the seasonal behavior of nocturnal mesospheric temperature over the Andes

and begins to build a climatology at the OH emission height. Nights with high quality data are defined by at least 4 h of cloudless images, although most nights average 5–10 h.

The mean OH temperature values for each night are recorded along with the standard deviation (σ) in the mean of the nightly temperature distribution, in order to reveal the nightly, and hence, yearly variations for the whole data set. This is illustrated in Figure 3.4, which plots the nocturnal mean OH temperature data (blue dots) for each individual year. During the course of any one night, the temperature can range from ± 5 K up to ± 20 K caused mainly by wave induced geophysical variability as represented by the error bars. During the 8-year period, the data show that the mean nightly temperature ranged typically from 170–230 K, with a mean value of 198 ± 5 K. For each individual year the mean OH temperature (T_{OH}) is given in Table 3.2, indicating very little variability from year to year. Note: the periodic (\sim monthly) short gaps are due to no camera operations during the full-moon period. Other gaps are due to bad weather and occasional MTM operational problems. The red curve on each plot shows the 30-day running mean smooth, with data gaps removed. The variations of the average temperature are quite large and show significant day-to-day variability. There is also visible evidence for longer-term seasonal variation in this data set possibly associated with an apparent semi-annual oscillation (SAO) signature peaking in the spring and fall.

Evidence of a SAO at low-latitudes was found in prior studies during the Maui MALT program [Taylor *et al.*, 2005; Zhao *et al.*, 2007]. The origin of the SAO is not clear but may be explained by several causes [Reed *et al.*, 1962; Takahashi *et al.*, 1995]. The semiannual variation in the solar zenith angle, and its resulting variation in the solar flux, should be one of the main sources [Roble and Ridley, 1994]. Seasonal change of the zonal and meridional wind system may also be important factors [Zhang

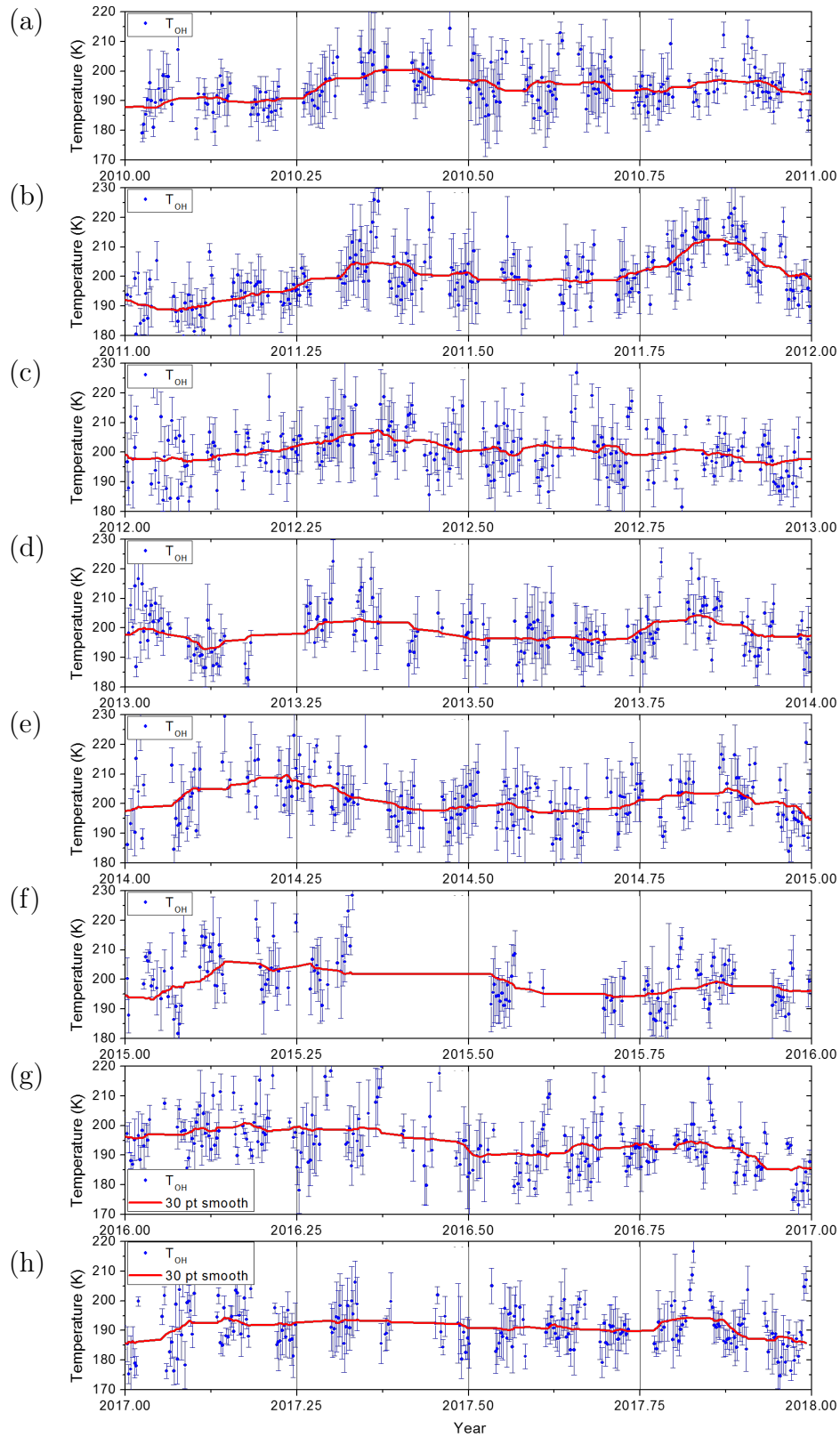


Figure 3.4. MTM nightly averaged T_{OH} measurements for each year 2010–2017. The blue points are the mean nightly temperatures, where the error bars are the standard deviation representing geophysical variability. A 30-day running-mean smoothing fit (red line) is shown.

Table 3.2. Results of the Harmonic Fits to the OH Rotational Temperature Time Series for the Years 2009–2017 at ALO.

Year	\bar{T}_{OH} (K)	N	AO		SAO		QAO	
			Amp (K)	ϕ	Amp (K)	ϕ	Amp (K)	ϕ
2009	192±8	64	–	–	–	–	–	–
2010	195±7	209	3.0	200	3.2	148	2.5	50
2011	200±9	241	4.0	250	7.4	133	2.5	49
2012	201±9	236	3.4	153	1.9	108	0.9	40
2013	199±8	190	0.7	271	4.4	131	4.3	20
2014	201±8	207	2.9	53	3.0	98	0.5	40
2015 [†]	199±10	146	5.7	120	3.2	127	5.2	51
2016	194±9	206	3.8	90	3.1	97	1.9	40
2017	191±7	210	1.3	121	1.7	101	3.3	37
ALO	198±5	365	1.9±0.3	192±10	3.4±0.3	131±3	2.0±0.3	37±3
Maui	197±14	365	2.4	42	3.8	111	1.5	31

[†] Limited data set.

et al., 2001]. The atmospheric solar tides and their seasonal variation in amplitude and phase are another possible factor which might explain such an oscillation.

At the location of ALO, which lies between low and mid-latitudes, both the SAO and annual oscillation (AO) signatures can be present. To investigate their signatures in the mesosphere and their relative contributions each year to the annual variability Figure 3.5 plots the MTM nightly averages for the whole 8 years (1700+ nights). While the mean temperature variability dominates from night-to-night, there is evidence of two peaks per year which is illustrated by a 30-night running-mean smoothing of the data shown by the solid red curve. The amplitude of this SAO is consistently

several K from year to year. Closer inspection reveals there is also a signature of an AO which is less coherent from year-to-year and smaller in amplitude than the SAO. Figure 3.6 takes this analysis a step further by plotting monthly-averaged temperature measurements. As before, the vertical bars indicate the standard deviation of the observed values from the means. The SAO signature is more evident in the monthly temperatures, showing maxima after the fall equinox (March–May) and in November with a higher peak during the fall (Note the exception in the year 2011 when the higher peak occurs in November).

Based on the apparent SAO signature in the temperature, a Lomb-Scargle (L-S) periodogram analysis is performed to investigate the spectral content of both the OH temperature and band intensity. The L-S periodogram is able to identify prominent periods in incomplete data sets [*Lomb, 1976; Press, 2007; Press and Rybicki, 1989; Scargle, 1982*]. This is particularly useful because long-term airglow data have gaps due to inclement weather, strong moon light and computer problems. Figure 3.7 shows the periodogram power versus wave period in days for the T_{OH} normalized to unity. The horizontal line indicates a 90% confidence level. Several well-defined peaks were identified well above the threshold level. These establish not only a dominant SAO component (180 days) but also a strong AO (353 day) and evidence for a novel 3-month or quarter-annual oscillation (QAO) at 91 days [*Zhao et al., 2016*]. Near identical periods were also detected in the intensity data (not shown). The 786 day (~ 26 months) period wave (not shown) may be evidence of a quasi-biannual oscillation (QBO) [e.g., *Huang et al., 2008; Wit et al., 2016*] and is not considered further in this study. Furthermore, the prominent 29-day period may be due to the monthly gaps in data caused by no operation during full moon. The SAO signature is very well defined and clearly dominates the other seasonal signatures at this intermediate-latitude site.

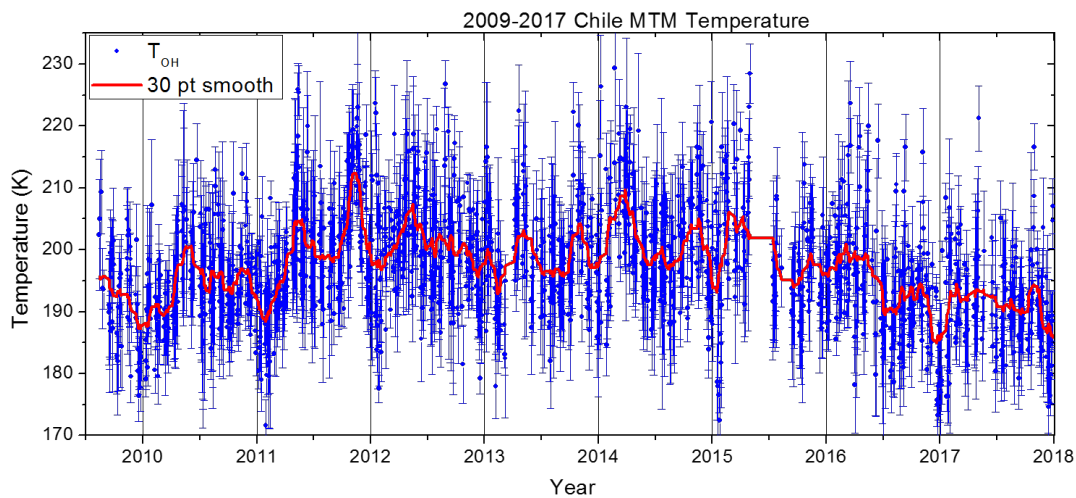


Figure 3.5. MTM nightly averaged T_{OH} measurements from 12 August 2009 until 31 December 2017 (years are separated by black vertical lines). The blue points are the mean temperature for each night and the error bars represent the standard deviation in temperature each night. A 30-day running-mean smoothing fit (red line) is shown.

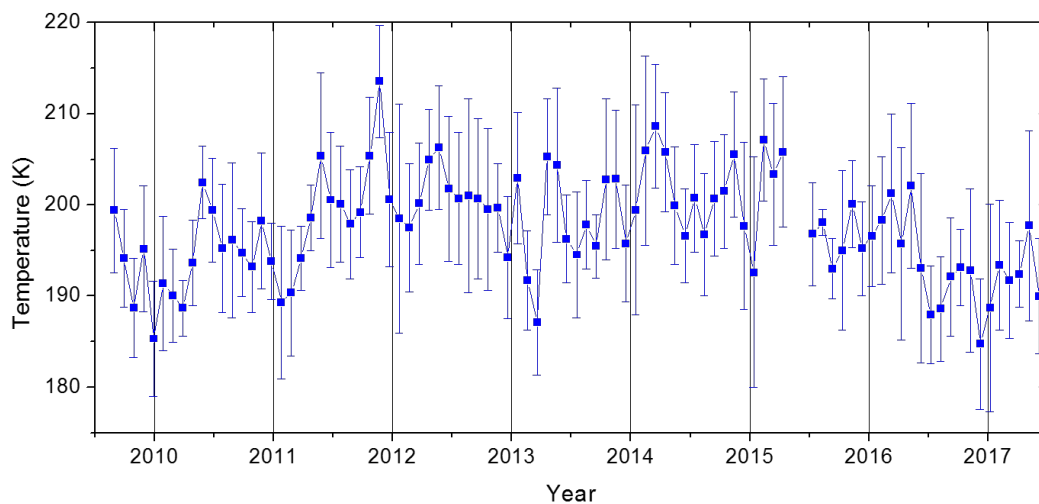


Figure 3.6. Monthly averaged OH temperatures from August 2009 to June 2017 showing clear SAO.

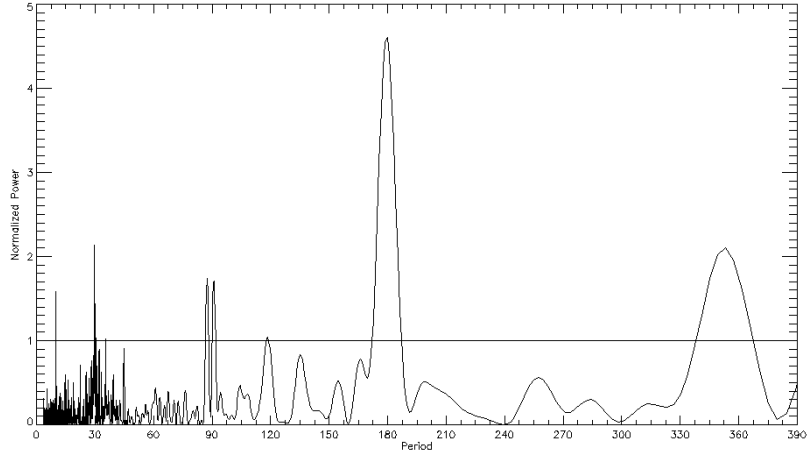


Figure 3.7. Lomb-Scargle periodogram analysis of T_{OH} for the 8-year data set showing annual and semiannual oscillation signatures. The horizontal line shows the 90% confidence level.

3.5.1. Year-to-Year Variability in Seasonal Oscillations

To reveal general trends in the observed AO and SAO (and QAO) variations of the T_{OH} , Figure 3.8a summarizes the annual mean variation of the 8-year data set superposed into a single year as a function of day number (as before, the error bars are dominated by geophysical variability). The twin peaks of the SAO are immediately evident occurring about a month after the fall (UT day 120) and spring (UT day 300) equinoxes. The fall peak tends to be larger than the spring peak as shown by the 15-day smoothing curve (red curve). To quantify the contributions of the AO, SAO and QAO components, a least-squares fit to these data has been performed of the form [Zhao *et al.*, 2007]

$$y(t) = A + C_1 \cos\left(\frac{2\pi t}{365} + \phi_1\right) + C_2 \cos\left(\frac{2\pi t}{182} + \phi_2\right) + C_3 \cos\left(\frac{2\pi t}{91} + \phi_3\right), \quad (3.1)$$

where A is the annual mean temperature, the second term is the fit to the AO, the third term is the fit to the SAO component, and the fourth term is the fit to the

QAO. The C variables are the amplitudes and the ϕ terms are the phase shifts. The resultant fit (black curve) to the data is clearly very good and the individual wave components are summarized in Table 3.2.

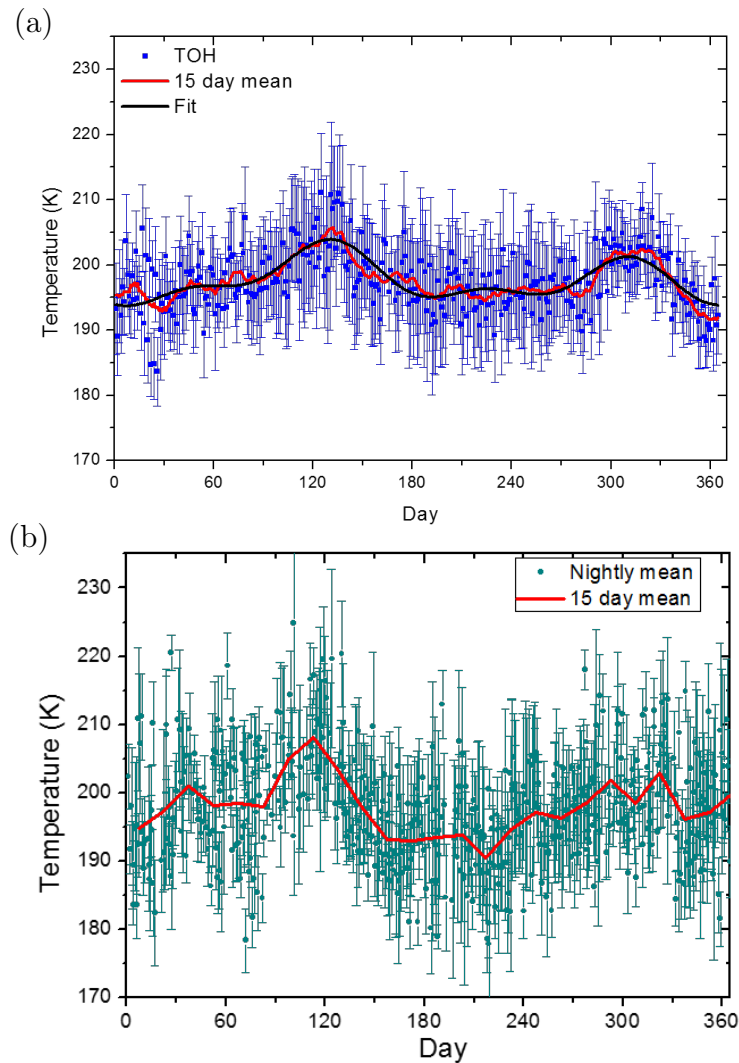


Figure 3.8. MTM nightly averaged T_{OH} measurements shown in one superposed year for both ALO and Maui. (a) T_{OH} measurements from 12 August 2009 until 31 December 2017. The blue points are the mean nightly temperature and the error bars represent the standard deviations. A 15-day running-mean smoothing fit (red line) is shown. A least-squares fit using a mean, AO, SAO and QAO is shown as the smooth black curve. (b) Similar data from Maui MALT campaign from November 2001 to December 2004 [Taylor *et al.*, 2005].

Table 3.2 summarizes the results of the least-squares fitting for the individual AO and SAO components for the T_{OH} data. The composite year reveals an SAO amplitude of 3.4 K, while the AO was significantly smaller at 1.9 K. The amplitude of the SAO tended to be larger during most years, however, from year-to-year their relative amplitudes and phases were observed to vary significantly. For example, the AO was larger during 3 years (2012, 2015, and 2016). Note: the year 2015 has significantly reduced data due to a computer failure (only 146 nights).

Table 3.2 also summarizes evidence for an unusual QAO signature. An QAO was initially found to be significant in 2010 and 2011 where its amplitude (2.5 K) was comparable to AO and SAO amplitudes [Zhao *et al.*, 2016]. More recently, in 2016 and 2017, the QAO amplitude again increased to be comparable with AO and SAO signatures. The year 2013 shows large SAO and QAO signatures (4.4 K, respectively), and a very low AO signature (<1 K), as depicted in Figure 3.4d. In contrast, 2011 exhibited the largest seasonal perturbation amplitudes for the AO (4.0 K), SAO (7.4 K), and QAO (2.5K).

The amplitudes of the individual components of the AO (black), SAO (blue), QAO (red) and their relative phases are plotted in Figure 3.9a as determined from the least-square fit. They strongly suggest that the origin of the asymmetry between the spring and fall temperature peaks is due to a combination of AO and SAO signals.

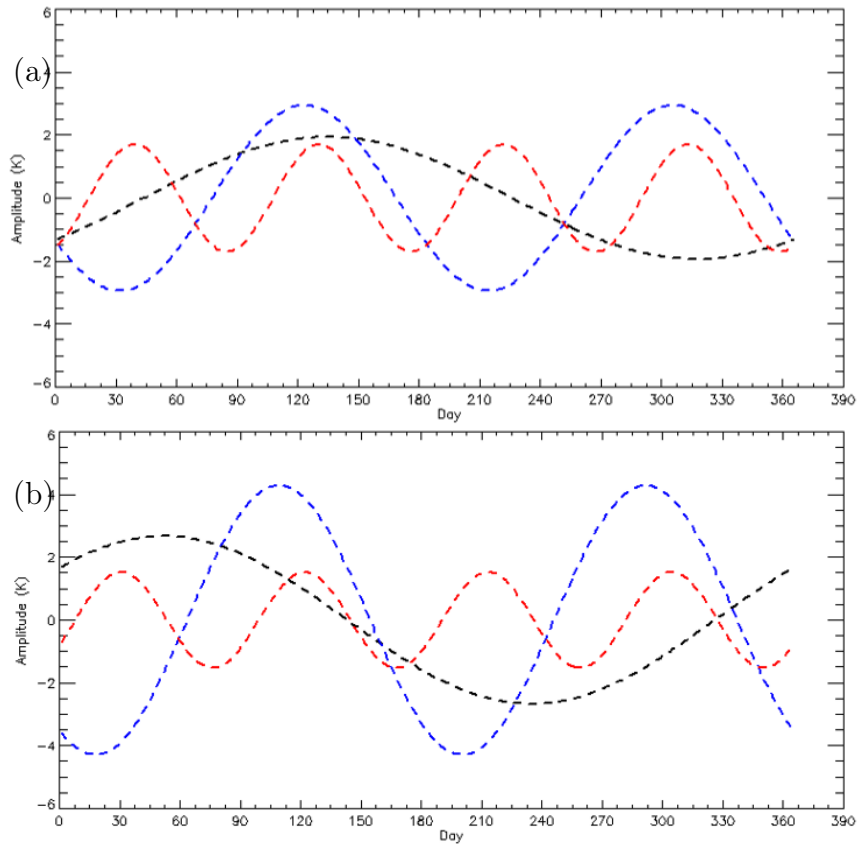


Figure 3.9. Harmonic analysis of Figure 3.8 showing the amplitude and phase of the AO (black), SAO (blue), and QAO (red) observed by the MTM at (a) ALO and (b) Maui.

To place these findings in a broader perspective, Figure 3.8b plots the results for three years (November 2001–December 2004) of MTM measurements at Maui folded into one year [Taylor *et al.*, 2005; Zhao *et al.*, 2005]. A 15-day running-smooth fit to T_{OH} data from Maui is also shown in red. Using the same basic Equation 3.1, Maui fitted amplitude results are also shown in Table 3.2. Maui results showed a mean T_{OH} of 197 ± 5 K, an AO with an amplitude of 2.4 K, an SAO of 3.8 K [Taylor *et al.*, 2005; Zhao *et al.*, 2007], and this new analysis presented herein also suggests an QAO amplitude of 1.5 K at Maui, as shown in Figure 3.9b.

In summary, ALO MTM results show an AO and a predominant SAO signature

with maxima near the equinoxes with the fall maximum being larger. These findings are in good agreement with previous results showing both AO and SAO signatures [e.g., *Gelinas et al.*, 2008; *Offermann et al.*, 2009; *Roble and Ridley*, 1994; *Zhang et al.*, 2001; *Zhao et al.*, 2005]. *Takahashi et al.* [1994] reported the SAO as a typical feature at low latitudes, while the AO is a dominant feature at higher latitudes. *Gelinas et al.* [2008] reported OH temperature and intensity measurements from Adelaide (34.9°S) and Alice Springs (23.7°S), Australia and indicated that the SAO of the diurnal tide dominated the OH intensity and temperature data with the peak of the SAO occurring a month after the equinoxes.

The extensive MTM data set (2009–2017) has enabled the identification of significant year-to-year variability in the relative amplitudes of AO and SAO, and the high precision of the measurements has enabled the occasional identification of QAO signatures, which are new and currently under further investigation.

3.5.2. Local Time Variability

So far, the seasonal analysis has used only nightly mean MTM data (i.e., 1 data point/night). However, the 8-yr MTM data set comprises over 388,000 data points (spread out over 12 hours in local time) enabling detailed investigations of tidally driven local time variations in mesospheric temperature and potential influences on the AO and SAO. *Reid et al.* [2017] and *Silber et al.* [2017] recently presented studies where they divided spectrometric nightglow data from Adelaide, Australia (34.9°S) and Tel-Aviv, Israel (32.1°N) respectively, into regular four 3-h bins and 1 min bins respectively, to study local time variability. Following their methods, the MTM data has been divided into twenty 30-min blocks and the resultant ALO T_{OH} data set is plotted in Figure 3.10. Each clear, moonless night is represented by a vertical column starting at the beginning of the night (~ 22 UT) and ending around 10 UT (maximum duration ~ 12 h), when the solar depression angle was $\geq 12^\circ$. In this format, the plot

shows that the T_{OH} was consistently colder during the nights in 2010, 2016, and 2017, and the nights were substantially warmer in 2011 and 2012, as previously suggested by their average values in Table 3.2. The gaps in the data arise mainly from no observations during the full moon and overcast skies (The plot also shows the longer austral winter nights occur during the middle of each year.).

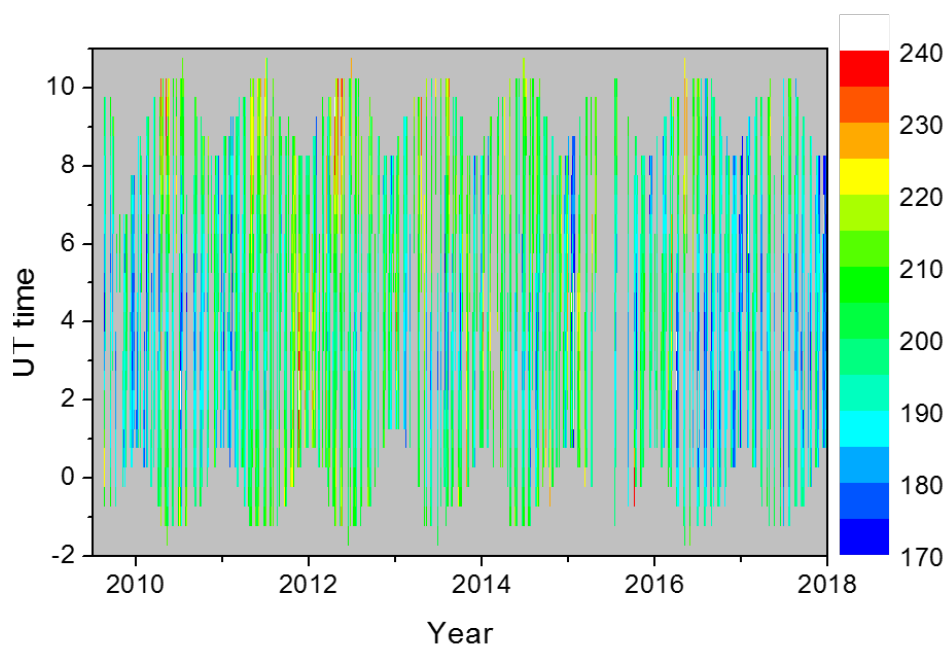


Figure 3.10. T_{OH} measured from 12 August 2009 until 31 December 2017. Each vertical column of data is one night averaged into thirty minute bins (1700 nights). The vertical axis shows the time over the course of the night, with local midnight at 04 UT (winter) and 03 UT (summer).

Figure 3.11 replots the data separately for each year for better identification of the reoccurring warmer and colder regions. In particular, the temperature feature in the cold years, 2016 and 2017, and warm years, 2011 and 2012, can now be visually compared. In both of these situations, colder temperatures generally occur in the evening hours during the summer months and warmer temperatures in the morning

hours during winter months. These findings agree with *Reid et al.* [2017] and *Silber et al.* [2017] who both identified similar pre-dawn warmings.

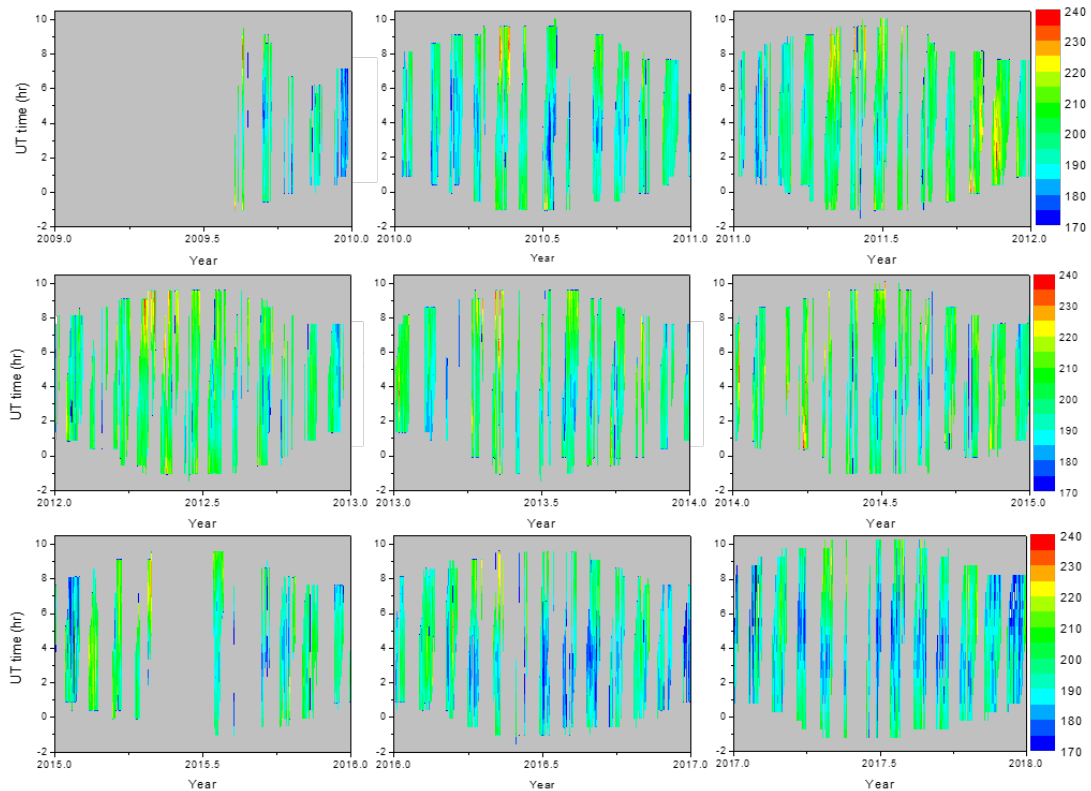


Figure 3.11. Similar to Figure 3.10 except each year (2009–2017) is shown separately for better resolution.

To investigate these thermal features further, the data set has been superposed into one year as shown in Figure 3.12a. This plot is very well populated and immediately identifies the extensive (~ 1 month duration) “hot spot” around day 120 in the early morning hours. Also evident during this period is a milder warming occurring in the early evening hours during the same days as the pre-dawn hot spot. A second, weaker warming is evident around day 310 where the mesosphere is warmer throughout the night. An extensive cold region occurs between these two warm regions centered on local midnight during days ~ 180 –250. Taken together, these structures

constitute the basic characteristics of AO and SAO signatures as reported in previous Figures 3.5, 3.6, and 3.8, and show significant local time and seasonal variability.

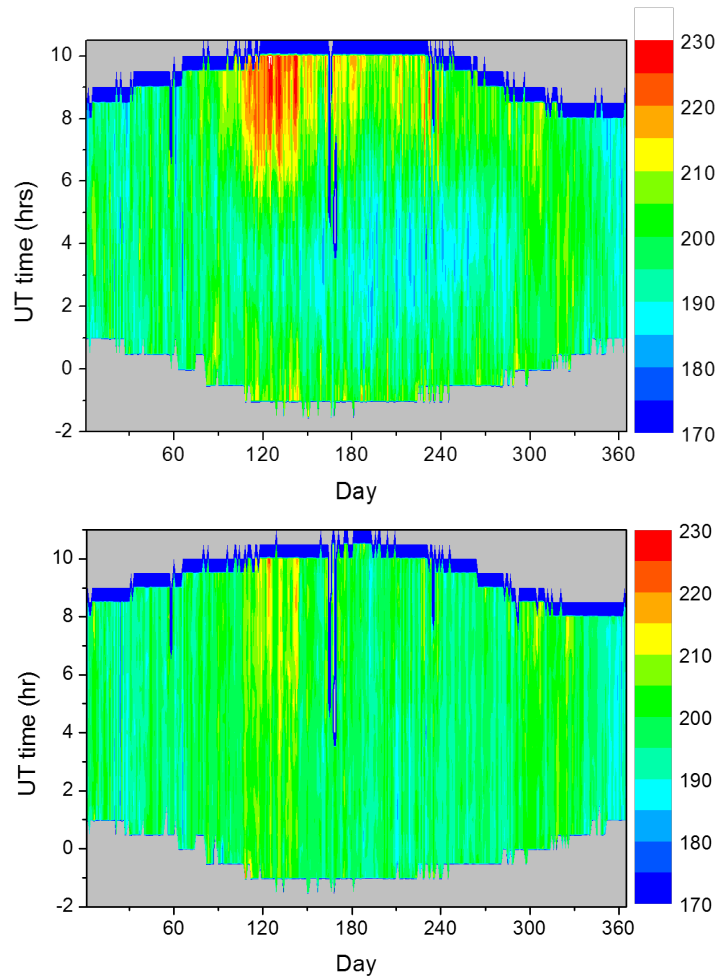


Figure 3.12. Thirty-minute T_{OH} data from Figure 3.10 folded into one superposed year for (a) raw data and (b) with tides removed. Note: plot (a) shows a high temperature peak around UT day ~ 120 near dawn (~ 06 – 10 UT), and plot (b) shows the reduced peaks.

One important source of variability are atmospheric tides. In particular, the diurnal and semidiurnal tides may introduce systematic biases during the course of the night. To investigate the combined influence of the tides, the diurnal (24 h) and semidiurnal (12 h) tide signatures were removed from each night using a modified version of Equation 3.1. The superposed year is shown in Figure 3.12b with the data

analyzed the same way as in Figure 3.12a. Harmonic analysis of each horizontal block was used to determine the mean amplitudes and phases of the AO and SAO in order to estimate the nightly geophysical variation with and without tides. The results are plotted in Figure 3.13. Before the tides were removed (Figure 3.13a), the amplitudes of the AO (black curve) and SAO (red curve) were variable with time, but both increased significantly during the course of night and dominated in the early morning with average values of 4.4 K and 3.7 K, respectively. With the tides removed (Figure 3.13b), the AO amplitude (black curve) reduced greatly ($\sim 60\%$) with an average amplitude of 1.9 K, while the SAO reduced slightly ($\sim 10\%$) to an average amplitude of 3.3 K. The phase of the AO changed significantly before tidal removal but remained constant, peaking on UT day 142, after the tides were removed. In comparison, the SAO phase remained approximately constant (peaking on day UT 125) before and after the removal of the tides. See Table 3.3 for details.

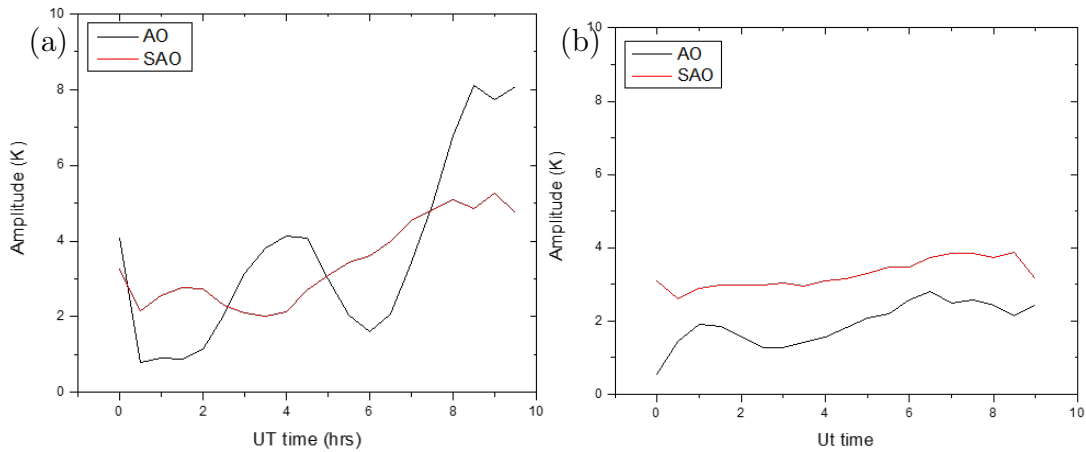


Figure 3.13. Results of harmonic analysis showing half-hour bins of the amplitude (measured in Kelvin) of the AO (black) and SAO (red) signatures from Figure 3.12a, (a) with and (b) without tides. Once tides are removed, the amplitude of the AO (black) and SAO (red) signatures are more constant throughout the night (from Figure 3.12b).

Table 3.3. Results of the harmonic fits to the T_{OH} time series for the superposed year (Figure 3.12a).

	AO		SAO	
	Amplitude (K)	ϕ (days)	Amplitude (K)	ϕ (days)
With Tides	4.4±0.9 K	113±18	3.7±0.4 K	121±2
Tides Removed	1.9±0.1 K	142±3	3.3±0.1 K	125±1

Given these results, when the superposed year, with tides (Figure 3.12a), is examined for the nightly OH variation, a change from a predominant SAO at the beginning of the night to a superposition of the AO and SAO by the end of the night with the AO dominating can be seen. These changes support the likely influence of tides on the local-time observed AO and SAO signatures. With tides removed, the AO was impacted significantly, while the SAO was only slightly affected. The recent tidal analysis by *Silber et al.* [2017] associated with seasonal measurements of the AO and SAO at similar latitudes revealed (their Figure 7) that the semidiurnal tide affected the amplitude of the AO, while the amplitude of the SAO was influenced by the diurnal tide. This finding suggests that at ALO the semidiurnal tide has a greater influence on the combined AO and SAO seasonal variations.

3.6. Summary and Conclusions

The MTM has succeeded in obtaining over 8 years (2009–2017) of high quality mesospheric OH intensity and temperature data from ALO, Chile (30.3°S). The rich data set includes over 1700 nights of measurements that are well-distributed throughout the years and in local time enabling high quality nocturnal GW studies and seasonal investigations. A key finding was the great variability from night to night in both temperature and intensity data, as well as clear semiannual seasonal oscillation.

Much of this chapter focuses on the use of MTM temperature data to investigate the seasonal variability in particular the distinct SAO which occurs at low-to-mid latitudes and dominates at ALO. Least-squares fitting analysis determines an average SAO amplitude of 3.4 K (range 2–7 K) peaking around UT day 131 over the 8 years, and an AO component which was significantly smaller with an average amplitude of 1.9 K (range 1–6 K) peaking around UT day 192. A systematic asymmetry was also found with the larger peak temperature occurring during the fall likely due to a superposition of the AO and SAO signatures. These results agree well with previous studies [*Reid et al.*, 2017; *Silber et al.*, 2017; *Zhao et al.*, 2007]. In particular, a comparison with similar MTM measurements from the low-latitude Maui MALT program revealed near identical SAO amplitudes at both sites. An unexpected QAO (average amplitude, 2 K) was also identified at ALO [*Zhao et al.*, 2016] and reanalysis of the Maui MALT data may also exhibit a similar but smaller QAO signature.

A clear SAO pattern is observed for both the OH intensity and temperature. To further investigate the dominant seasonal signature, the effect of tidal oscillations were studied following the methods of *Reid et al.* [2017] and *Silber et al.* [2017]. As the seasonal airglow data time series is not continuous (12 h maximum) for each night, it is difficult to quantify the tides. Nevertheless, a harmonic local-time analysis was performed to remove solar diurnal and semidiurnal tidal contributions. With tides removed, the amplitude of the AO reduced significantly ($\sim 60\%$), while the amplitude of the SAO reduced only slightly ($\sim 10\%$). The recent tidal analysis by *Silber et al.* [2017] associated with seasonal measurements of the AO and SAO at similar latitudes ($\sim 30^\circ$) revealed that the semidiurnal tide affected the amplitude of the AO, while the amplitude of the SAO was influenced by the diurnal tide. Thus, at ALO the semidiurnal tide most likely has a greater influence on the seasonal variations.

CHAPTER 4

COINCIDENT MTM AND SABER MEASUREMENTS OF MESOSPHERIC TEMPERATURE OVER ALO

4.1. Introduction

In addition to ground-based observations of the mesosphere there have been several space-borne instruments which have made significant contributions to our knowledge of MLT region dynamics and temperature field. In particular the SABER instrument onboard the TIMED satellite has and continues to make major contributions to ongoing MLT studies [Liu *et al.*, 2015; López-González *et al.*, 2007; Noll *et al.*, 2016; Qian *et al.*, 2017; Reisin and Scheer, 2017; Remsberg *et al.*, 2008; Xu *et al.*, 2006, 2010, 2012]. Other space-based measurements of the MLT include the Optical, Spectroscopic, and Infrared Remote Imaging System (ORISIS) [Sheese *et al.*, 2011, 2014]; Scanning Imaging Absorption Spectrometer for Atmospheric Cartography (SCIAMACHY) [von Savigny *et al.*, 2004] and Michelson Interferometer for Passive Atmospheric Sounding (MIPAS) [García-Comas *et al.*, 2012] on the European ENVISAT; Atmospheric Chemistry Experiment â Fourier Transform Spectrometer (ACE-FTS) [Mulligan and Lowe, 2008]; Cloud-Aerosol Lidar with Orthogonal Polarization (CALIOP) [Alexander *et al.*, 2013]; Microwave Limb Sounder (MLS) [French and Mulligan, 2010; Jiang *et al.*, 2002, 2004]; the Cloud Imaging and Particle Size Instrument (CIPS) and Solar Occultation for Ice Experiment (SOFIE) on the AIM (Aeronomy of Ice in the Mesosphere) satellite [García-Comas *et al.*, 2014; Randall *et al.*, 2017]; and stratospheric soundings by the Atmospheric Infrared Sounder (AIRS) [Alexander and Teitelbaum, 2007], and the Cryogenic Infrared Spectrometers and Telescopes for the Atmosphere (CRISTA) instrument [Preusse *et al.*, 1999; Scheer *et al.*, 2006].

Ground-based observations of the atmosphere offer important information about the night-to-night variability on local time scales, and have great potential for long-term studies while being very cost effective. However, they are limited due to global geophysical coverage and suffer from inclement weather. In contrast, space-based observations provide much more “global” coverage depending on their orbit. Coordinated use of both ground-based and space-based data sets can provide a better understanding of the local and regional structure and long- and short-term variability in the MLT region.

Several comparative studies have been conducted between ground-based OH temperatures and SABER measurements. For example, *Oberheide et al.* [2006] and *Mulligan and Lowe* [2008] compared ground-based spectrometer measurements of the OH rotational temperature derived from OH Meinel band (3,1) data with SABER kinetic temperatures from three sites: Wuppertal (51°N), Maynooth (53.2°N) and Stockholm (59.5°N), all at mid-to-high Northern latitudes. Their extensive comparisons showed good agreement between the ground-based and SABER data, and on average the spectrometer OH temperatures were warmer than the SABER temperature by 4.5–8.6 K at the nominal OH altitude of 87 km. *López-González et al.* [2007] compared OH (6,2) Meinel band temperature measurements from Sierra, Nevada (37°N) with SABER observations at mid-latitudes. They reported similar temperature variations from night to night and throughout the season, and that the ground-based measurements were also warmer by ~ 5.7 K at 87 km altitude. *French and Mulligan* [2010] compared OH (6,2) rotational temperature measurements from Davis, Antarctica (68°S) with SABER over a seven year period (2002–2009). They reported warm bias of the ground-based measurements over the SABER temperature measurements. A more limited campaign of 120 nights over three winter periods, *Parihar et al.* [2017] found ground-based OH (6,2) rotational temperatures to be warmer than SABER

measurements by 4–5 K at Ranchi, India (23.3°N) at low-latitudes. All of these studies indicate a general good agreement with SABER and all point to a similar warm bias of the ground-based OH temperatures compared to the SABER measurements by, typically, 5 K. These comparative studies enable the identification of systematic differences and biases between the two techniques and validate their combined use for studying the thermal structure of the MLT region.

4.2. SABER Instrument and OH Temperature Data

The TIMED satellite was launched in December 2001. Its primary mission is to obtain state variables and study the energy transfer in the MLT region, at that time, the least understood and least explored region of the earth’s atmosphere [Yee *et al.*, 1999]. TIMED was launched in a circular orbit at 625 km altitude inclined at 74° to the equator [Russell III *et al.*, 1999]. SABER, built by USU’s Space Dynamics Laboratory, is one of four instruments aboard TIMED managed by NASA Langley Research Center. The SABER data provide fundamental information on the energy balance, chemistry, dynamics and transport of the MLT region [Mlynczak, 1997; Russell III *et al.*, 1999]. SABER is a versatile infrared radiometer capable of global measurements of the Earth’s limb producing the first comprehensive profile measurements of state parameters and species related to energetics and thermal structure in the MLT region [Remsberg *et al.*, 2008]. The technique that SABER uses to sound the atmosphere has “never before been used to study the MLT region in such detail” [Russell III *et al.*, 1999].

SABER views 90° to the right of the trajectory of the TIMED satellite and has an instantaneous FOV of 2 km by 24 km. It provides continuous coverage for the latitudes of 52°N–52°S with a view of higher latitudes (up to 83°N or S) alternating every 60+ days due to its yaw cycle. SABER is a 10-channel broadband limb-scanning infrared radiometer covering the spectral range from 1.27 μm to 17 μm . These up

and down limb scans view IR radiation emitted from the surface to the thermosphere (10–400 km) every 53 sec and their analysis provide profile measurements of kinetic CO₂ temperature, pressure, H₂O and CO₂, O₃ mixing ratios, and the volume emission rates of O₂ and OH, and heating and cooling rates among other measurements with a vertical resolution of ~ 2 km at the tangent point. *Remsberg et al.* [2008] reported systematic and random errors of 3.8 K and 2.2 K respectively for the SABER Version 1.07 temperature measurements. This study uses the kinetic CO₂ temperature profiles of SABER Level 2A data which cover the range of 15–100 km in altitude, and in order to reduce statistical uncertainty the data are averaged vertically over 1 km. Data and additional instrument details are available from <http://saber.gats-inc.com>. SABER obtains kinetic temperature profiles and before comparisons with ground-based T_{OH} can be made, the OH equivalent temperature (T_k) must be estimated (Discussed in Section 4.2.2).

The MTM instrument has a FOV corresponding to 150 km diameter at the OH emission altitude. However, for this chapter, only temperature measurements from the zenith were used, corresponding to a smaller 4.5 km by 4.5 km square region. The T_{OH} represents the weighted temperature of OH emission layer at the presumed altitude of 87 km.

4.2.1. Coincidence of SABER overpasses and MTM measurements

To quantify the comparison of the MTM data set with SABER measurements, criteria were selected to maximize the number of coincident measurement events between the two instruments. In theory, concurrent measurements of the SABER T_k and the ground-based OH T_{OH} from the same location should be used for comparison. In practice, exact overpasses are not common. Therefore, to investigate the effect of the size of the sample region on the comparative study three spacial coincidence regions of different sizes were initially selected: $\pm 2.5^\circ$, $\pm 5.0^\circ$, and $10^\circ \times 20^\circ$ latitude-longitude

boxes centered on ALO (30.3°S, 70.7°W).

When a SABER measurement event coincides with the MTM operating, a comparison of these data can be made by averaging several T_{OH} measurements for comparison with each SABER T_k . A short temporal window of ± 6 min was used for this study, a similar window was successfully employed for a study using the MTM OH data from Maui MALT (See Section 4.2.4). If the SABER event occurs just outside the MTM observation window, but still within the 6 min, then the closest 6 min of T_{OH} were averaged. T_k obtained outside this 6-min window are considered not coincident.

Nightly coincidence measurements were obtained over a time range of 23 to 11 UT throughout the year. Table 4.1 summarizes the statistics of all SABER T_k measurements that coincide with MTM measurements of T_{OH} during the period 2009–2016. The table lists the three different spatial box sizes centered over ALO, $\pm 2.5^\circ$, $\pm 5.0^\circ$, and $10^\circ \times 20^\circ$, and the number of events that occur in each box. A Gaussian curve was fitted to the distribution of temperature differences (ΔT), SABER T_k minus MTM T_{OH} , between the two measurements revealing a temperature offset of -5 K and FWHM of ~ 14 K, -5 K and FWHM of ~ 15 K, and -6 K and FWHM of ~ 16 K respectively. A negative ΔT indicates that the SABER T_k is cooler than the MTM T_{OH} . This shows that the OH layer is largely uniform over these considered scale sizes, and the spatial coincidence criteria can be decreased to increase the number of coincident measurements with little effect on the obtained biases. Therefore, to maximize the number of samples, the latitude-longitude box size of $10^\circ \times 20^\circ$ was chosen for this study.

4.2.2. OH Layer Thickness Comparison

As discussed in Section 1.2, hydroxyl emissions originate from a well-defined layer at a nominal altitude of 87 km with a layer thickness of ~ 8 – 10 km [*Baker*

Table 4.1. Coincidence SABER Temperature and T_{OH} Measurements For 2009–2016 Using Different Size Latitude-Longitude Boxes Centered on ALO.

Spatial Criterion	Events	ΔT (K)	FWHM (K)
$5^\circ \times 5^\circ$	394	-5.1	14.3
$10^\circ \times 10^\circ$	1720	-5.2	15.3
$10^\circ \times 20^\circ$	3465	-5.5	16.2

and Stair Jr, 1988; Yee *et al.*, 1997; Zhao *et al.*, 2005]. Approaches to find the OH equivalent temperature from the SABER T_k profiles have included using a Gaussian shaped weighting function [e.g., French and Mulligan, 2010; Oberheide *et al.*, 2006; Remsberg *et al.*, 2008] and the measured OH volume emission rates (VER) profiles from the SABER 1.6 μm or 2.0 μm channels [Mulligan and Lowe, 2008; Parihar *et al.*, 2017; She and Lowe, 1998, e.g.,]. The SABER OH VER channel has contributions from the OH (5,3) and (4,2) bands which peak at different altitudes [Baker and Stair Jr, 1988; von Savigny, 2015, and references therein], so the Gaussian-shaped weighting function was chosen for the present study, as given by:

$$f(z) = \frac{1}{\sqrt{2\pi\sigma^2}} \exp\left[-\frac{1}{2} \left(\frac{z - z_o}{\sigma}\right)^2\right], \quad (4.1)$$

where z is the altitude, z_o is the reference altitude, and σ is the standard deviation. Individual SABER temperature profiles were height-weighted using the Gaussian function with the reference altitude being 87 km with a layer thickness, or full width at half maximum ($\text{FWHM} \approx 2.355\sigma$), of ~ 9.3 km. Yee *et al.* [1997] and Remsberg *et al.* [2008] used a OH layer thickness of 9.3 km, while Oberheide *et al.* [2006] used a OH layer thickness of 8.7 km. Figure 4.1a compares 1833 SABER profiles, from 2016, using the two different layer thicknesses and shows very good agreement. The

resultant temperature difference was only 0.1 ± 0.4 K, as shown in the distribution of Figure 4.1b. These OH layer thicknesses were also compared with thinner and thicker layers of 6 to 10 km yielding similar results. In comparing the four different possible layer thicknesses, it is concluded that there is no significant difference between the T_k values obtained. In the current study a value of 9.3 km is therefore used, as this was the same Gaussian-shaped height-weighting function previously used by *Zhao et al.* [2005] and *Remsberg et al.* [2008] using the MTM at Maui, Hawaii (20.8°N).

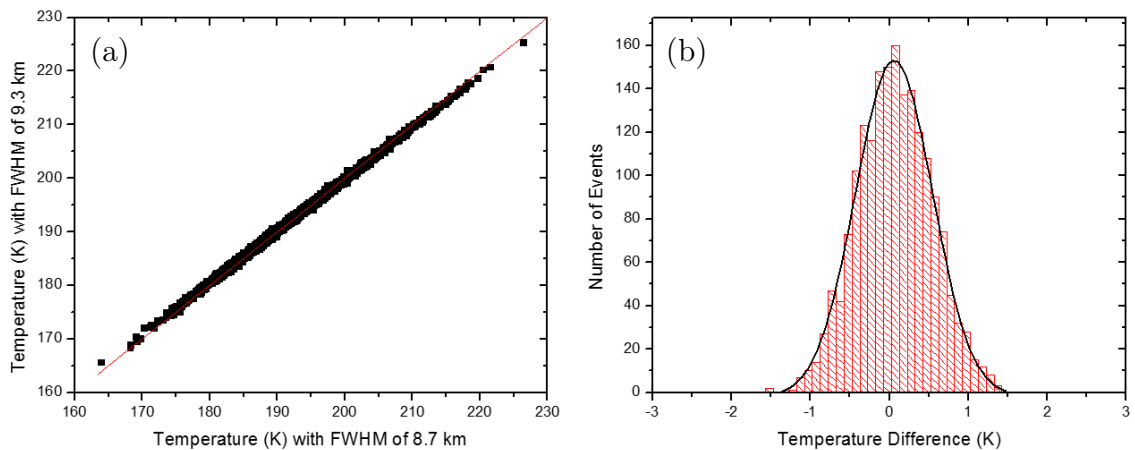


Figure 4.1. Comparison of different OH layer thickness assumptions. (a) Linear fit to comparison of SABER OH-equivalent temperature measurements with different thicknesses for 1833 temperature profiles centered over ALO at a height-weighted altitude of 87 km during the year 2016. (b) The distribution of temperature differences for the 1833 temperature measurements. Gaussian fit shows a difference of only 0.06 K with a FWHM of 1.0 K.

4.2.3. SABER Version Comparison

The most recent version of data available from SABER is version 2.0, which is an improvement over all previous versions, including v1.07. The new version features improvements to the production algorithms to reduce differences in up and down scans of the radiance data, improvements to the procedures for simultaneous measurements of the temperature and density, and updates to the climatology models which has

reduced the number of anomalies. Most of these updates affect the stratosphere and high-latitude measurements. To quantify the difference between versions, one year of data, 2010, is used. A total of 1826 SABER T_k profile measurements from a $10^\circ \times 20^\circ$ box centered on ALO were used. The mean temperature for SABER v1.07 for the 1826 profiles at the height weighted altitude of 87 km was 194.1 ± 8.4 K and the mean temperature for the SABER v2.0 was 192.4 ± 8.5 K. The SABER temperature measurements are plotted in Figure 4.2a showing a very linear relationship with a slope of 0.99. Figure 4.2b shows a Gaussian curve fit to the difference between the two versions revealing a difference of 1.6 ± 1.2 K, v1.07 being warmer. This shows that the SABER version measurements are very similar, as should be expected. Due to the improvements offered by v2.0 and because v1.07 was completely replaced as of January 2013 for the rest of the study, SABER v2.0 Level 2A data will be exclusively used in this dissertation.

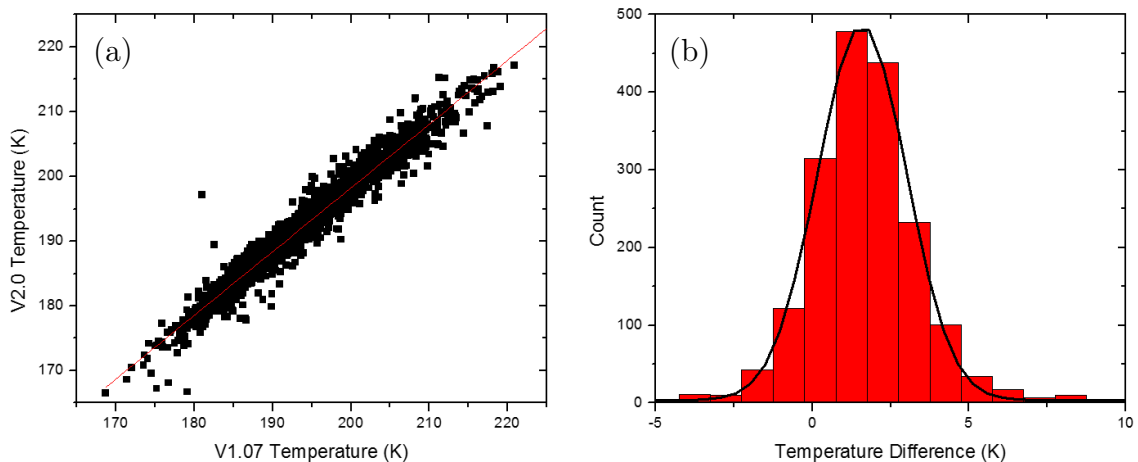


Figure 4.2. SABER versions 1.07 and 2.0 OH-equivalent temperature comparison. (a) Linear fit to the comparison of SABER versions 1.07 and 2.0 temperature measurements for 1826 SABER temperature profiles centered over ALO at a height-weighted altitude of 87 km during the year 2010. (b) The distribution of ΔT for the 1826 temperature measurements. Gaussian fit shows difference of 1.6 ± 1.2 K.

4.2.4. Previous Comparison Between SABER and the MTM

From November 2001 to December 2006, the MTM instrument operated from the Air Force AMOS facility, Maui, Hawaii (altitude 2970 m, 20.8°N, 156.2°W) obtaining over 1000 nights of high-quality data [Zhao *et al.*, 2005, 2007]. Remsberg *et al.* [2008] reported a comparison with previous SABER v1.07 temperature and the MTM T_{OH} . Maui comparison used a $10^\circ \times 20^\circ$ coincidence box and MTM T_{OH} were averaged over ± 12 min. Figure 4.3a shows a time series plot for over 2300 coincidence events during 2003 showing SABER T_k measurements (red circles) and MTM T_{OH} (blue). Both data sets show large variabilities (up to 40 K) during 2003, and the MTM and corresponding SABER measurements tracked each other well. The SABER average temperature was 197.0 K, while the average MTM temperature was slightly warmer, 202.2 K. Figure 4.3b is a histogram plot with a fitted Gaussian curve of the distribution of the temperature differences, ΔT , showing a systematic temperature offset of 5.2 ± 0.2 K with the MTM warmer.

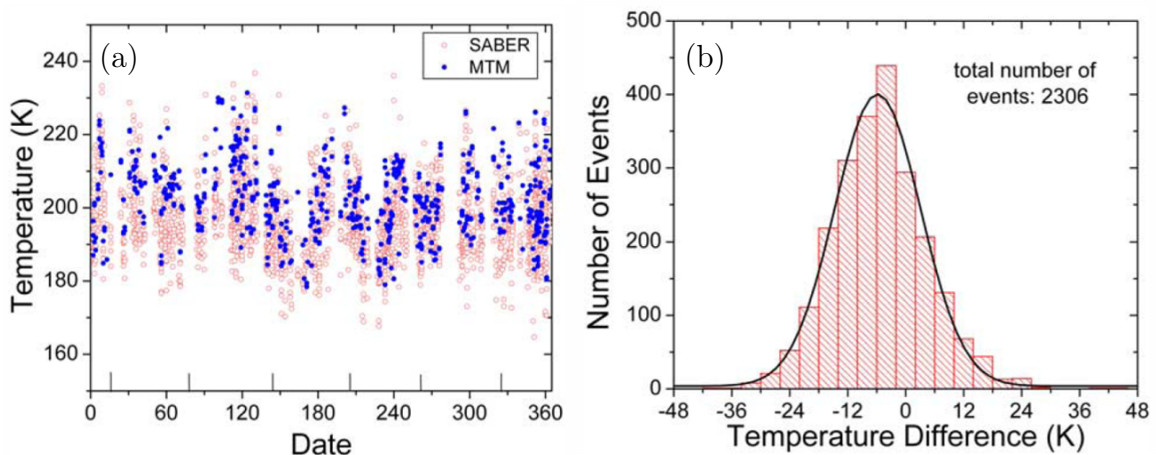


Figure 4.3. Temperature difference between SABER and MTM observed over Maui. (a) Time series of the SABER T_k (red) and the MTM T_{OH} temperatures (blue) for 2003 at Maui [Remsberg *et al.*, 2008]. (b) Histogram of ΔT with a Gaussian fit and a standard deviation of 8.9 K [Remsberg *et al.*, 2008].

In a similar study, *von Savigny et al.* [2004] reported space-borne OH (3,1) Meinel band temperature measurements by the SCIAMACHY instrument and also compared them with the MTM T_{OH} from Maui, Hawaii (21°N). They reported the measurements were in good agreement, and that the ground-based measurements were again warmer with a similar mean temperature difference of 7.1 K.

4.3. ALO MTM and SABER Temperature Comparison

For comparison with the 8 years of ALO data, all coincident SABER temperature measurements within the $10^\circ \times 20^\circ$ box are recorded. In practice, up to ~ 8 SABER measurements are possible each night. As in prior studies, each of the SABER temperature measurements is compared with the closest MTM temperature measurements. Two example nights are illustrated in Figure 4.4 with the 12-min averaging window shown by the bold, black lines. Figure 4.4a shows T_{OH} obtained 22–23 May 2012 illustrating the typical variability observed at ALO. The figure shows the derived zenith T_{OH} as discussed in Chapter 3 (blue) and identifies two coincident SABER overpass T_k measurements (mean value = 197.5 K, red circles) at ~ 0500 UT with a mean difference of 0.7 K. Likewise, Figure 4.4b shows the T_{OH} (blue) obtained 7–8 September 2013 and two coincident SABER overpass T_k measurements (mean value = 182.8 K, red circles) at ~ 0410 UT (see data in enlarged box) with a mean difference of -0.5 K. Note the importance of using a short averaging window due to strong GW-induced variability.

Figure 4.5 shows the comparison between SABER v2.0 T_k (open red squares) and MTM T_{OH} (open blue circles) for 3465 coincidences within the $10^\circ \times 20^\circ$ sample volume centered on ALO during the period of 2009–2016. The seasonal temperatures ranged from ~ 160 – 230 K and had a mean of 191.3 ± 0.1 K ($\sigma = 8.2$) for SABER and 198.0 ± 0.2 K ($\sigma = 8.2$) for the MTM data. The SABER and MTM temperatures again track well and show good agreement throughout this period as shown by the 30-day

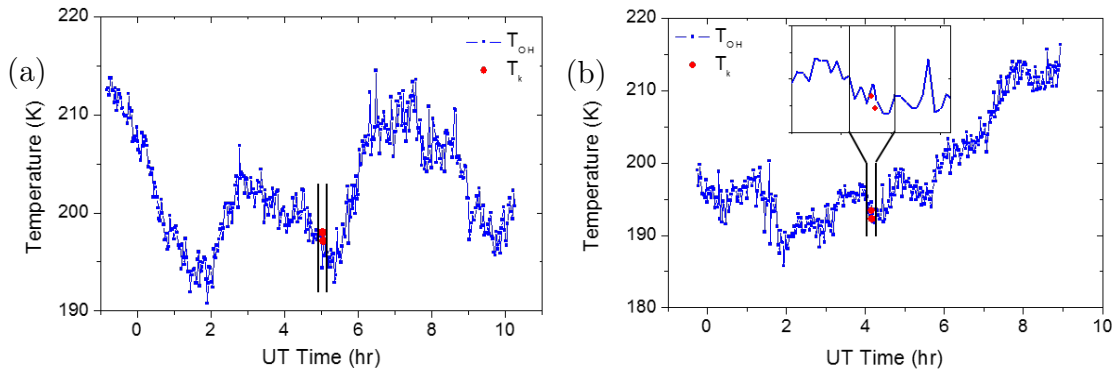


Figure 4.4. MTM data obtained 22–23 May 2012 and 7–8 September 2013 with coincident SABER measurement. (a) The derived zenith OH (6,2) rotational temperature (blue) and two superimposed coincident SABER overpass temperature measurements (red circle) at 0500 UT. (b) The derived zenith OH (6,2) rotational temperature (blue) and two superimposed coincident SABER overpass temperature measurements (red circle) at 0410 UT.

smooth fits (red line and blue line, respectively). However, the mean temperature measurements from ALO are consistently warmer than those measured by SABER during this extended period revealing a consistent ~ 5 K systematic offset between the two data sets, with ALO warmer. Table 4.2 displays the mean temperature and standard deviation, as well as the number of coincident events each year, n . Note the number of coincidence measurements differ from year to year based on when the MTM was operating as limited by the full moon, cloud coverage, power outages or computer problems, and the 60-day yaw cycle of the TIMED satellite.

In Figure 4.6a, the ALO temperature measurements are superposed into one year for comparison with results from Maui (shown before in Figure 4.3a). Both Figures consistently show an offset with the T_{OH} higher than the T_k . The average ΔT at Maui and ALO are similar, both being warmer than SABER. This offset at ALO is shown in Figure 4.6b which plots a distribution of the ΔT , along with a Gaussian fit. Both Figures 4.3b and 4.6b show very similar distributions yielding good Gaussian

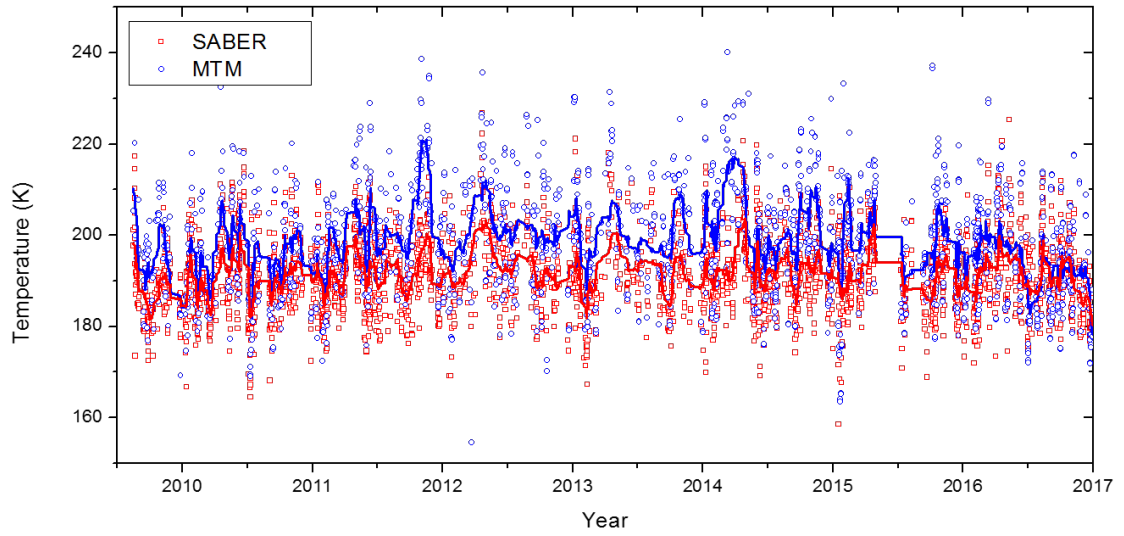


Figure 4.5. Time series of the SABER T_k (red squares) and the MTM T_{OH} (blue circles) with a 30-day running mean applied to both data sets.

Table 4.2. Yearly Mean SABER T_k and Mean T_{OH} and Standard Deviations, σ .

Year	\bar{T}_k (K)	σ	\bar{T}_{OH} (K)	σ	n
2009	188.0	7.4	195.0	11.3	169
2010	190.1	8.4	194.7	11.0	552
2011	191.5	7.6	200.4	11.6	574
2012	193.1	8.9	200.4	12.6	269
2013	191.6	9.0	200.0	11.2	294
2014	192.6	8.2	201.6	12.1	566
2015	190.9	7.9	198.6	11.7	440
2016	191.3	8.2	193.7	10.2	601
TOTAL	191.3±0.1	8.2	198.0±0.2	11.8	3465

fits. The peak of the ALO Gaussian is -5.5 ± 0.3 K ($\sigma=6.9$), and although ALO provides 50% more data than the Maui data set, it compares very well with the Maui results, -5.2 ± 0.2 K ($\sigma=8.9$). Despite the expected increase in GW activity due to orographic forcing over the ALO site, the FWHMs of the ALO and Maui data are similar. This provides good confidence when comparing SABER and ground-based measurements under different geophysical forcing conditions.

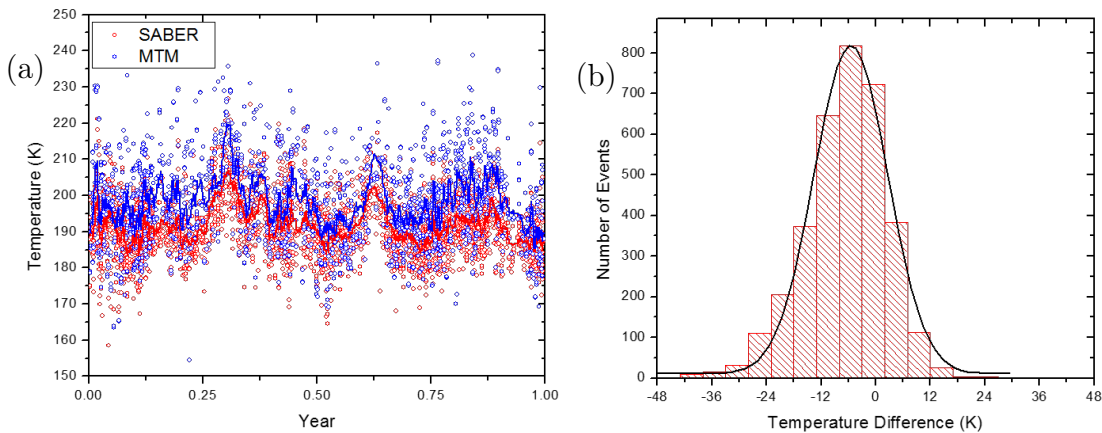


Figure 4.6. Temperature difference between SABER and MTM observed over ALO. (a) A time series of the SABER T_k (red squares) and the MTM T_{OH} (blue circles) for 2009–2016 at ALO superposed into one year. A 30-point running smooth applied. (b) A distribution of the ΔT with a Gaussian fit showing the ~ 5 K offset.

To further investigate these measurements, Figure 4.7a compares the measured T_{OH} with the SABER T_k for each of the 3400 coincidence data points. The plot shows a distinct elongated clustering in the data suggesting a linear relationship. The dashed line depicts a 1:1 relationship between the two data sets. However, the red line shows the actual linear fit which is similar in slope at 0.91 but is offset, yielding an unexpectedly low coefficient of determination (R^2) of 0.41. Closer examination of the plot shows that for a given SABER temperature (e.g., 200 K) there is a broader

range of MTM T_{OH} as indicated by the large Gaussian widths (σ) of the T_{OH} (see Table 4.2).

For comparison, Figure 4.7b shows results from a comparative study with the GRIPS instrument and SABER at mid-latitudes as reported by *Oberheide et al.* [2006]. Their study used three years of measurements and yielded a high correlation between SABER and GRIPS temperature measurements (slope of 0.99 and R^2 of 0.86), as well as a systematic temperature offset of 7.4 K. They also found that there was no significant year-to-year and month-to-month biases. Furthermore, they concluded that 87 km was the best altitude to use when calculating the OH equivalent temperatures from the SABER data [*Oberheide et al.*, 2006]. One possible cause for the low correlation coefficient in 4.7a could be related to seasonal changes in the OH layer as SABER measurements are referenced to the 87 km altitude.

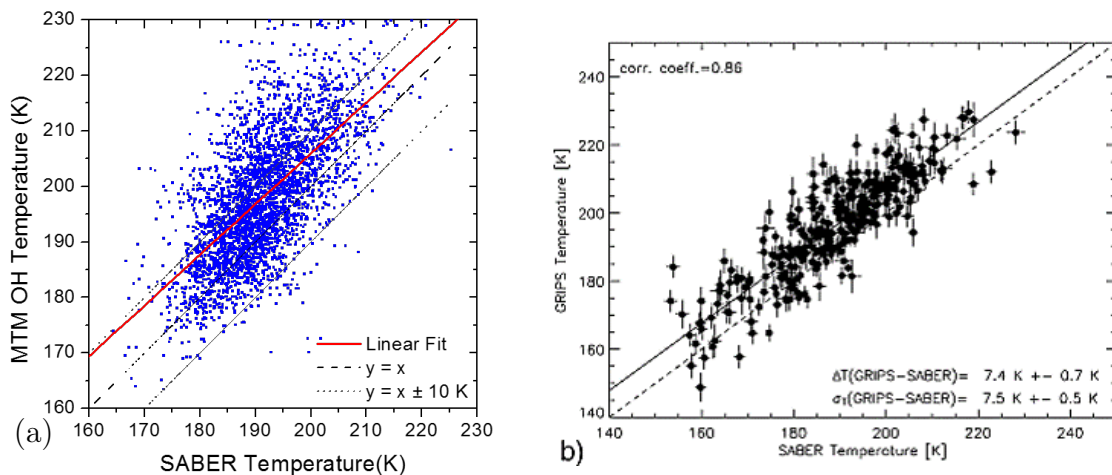


Figure 4.7. Scatter plots of the MTM T_{OH} versus SABER T_k and GRIPS OH temperature versus SABER T_k showing linear relationships. (a) MTM T_{OH} versus SABER T_k , for 2009–2016 at ALO. The dashed lines show $y = x$. Slope is 0.91. (b) GRIPS OH temperature versus SABER T_k [*Oberheide et al.*, 2006]. Slope is 0.99.

4.3.1. Seasonal Investigation

To investigate the possible effects of seasonal variability, Figure 4.8 plots the mean ΔT as a function of month (January–December, 1–12). While the mean ΔT is -5.5 ± 0.3 K ($\sigma = 6.9$ K), the figure clearly shows the offset changes from month-to-month in a cyclic manner with the greatest differences occurring in April and November (~ -9 K), which is also when the SAO peaks occur as determined from the MTM data (see Figures 3.6 and 3.8a). In contrast, the smallest ΔT at ALO occurs during both the winter and summer months (~ -4 K). *Mulligan and Lowe* [2008] compared ground-based OH temperature measurements from Maynooth, Ireland (53.2°N) with SABER temperatures and reported an annual seasonal variability in the ΔT at this mid-latitude site. They assumed that the variability in the temperature is due primarily to seasonal changes in the OH layer altitude. They determined that higher SABER temperatures measured in the winter months were primarily due to the lower altitude of the OH layer, while summer months were dominated by a higher (and thinner) OH layer. Applying this finding to Figure 4.8 suggests that during the winter months at ALO the OH layer was closest to the nominal altitude of 87 km as assumed in *Mulligan and Lowe* [2008], *Oberheide et al.* [2006] and in this study. Taken together, the ALO results suggest that the observed cyclic ΔT may be due to a change in altitude of the OH layer in synchronization possibly driven by the SAO. During SAO peaks the altitude layer was furthest from the nominal altitude of the OH layer. *Mulligan and Lowe* [2008] discussed a range of altitudes for the OH layer, $\sim 84\text{--}88$ km.

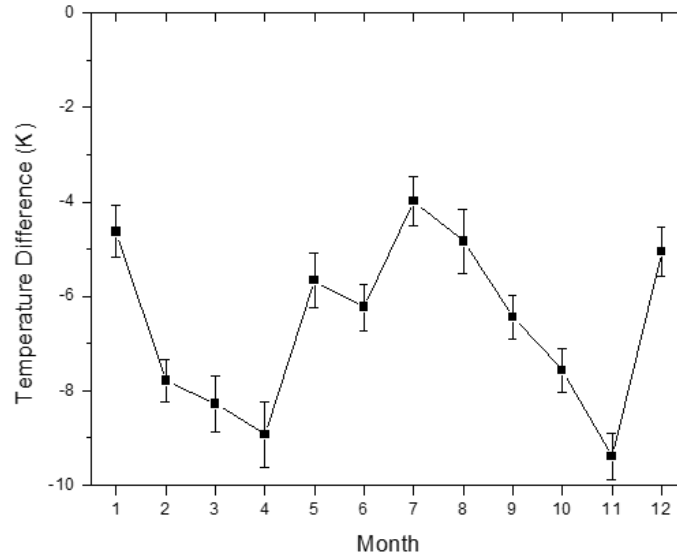


Figure 4.8. Monthly mean difference between the SABER T_k and the MTM T_{OH} folded into one year for 2009–2016 at ALO.

4.3.2. Longer-Term Trends

To investigate longer-term trends in the MTM data Figure 3.5 from Chapter 3 is replotted as Figure 4.9 with a second-order polynomial fit (red curve) showing a longer-term trend in the temperature data. The blue circles show the individual nocturnal mean temperatures and the blue curve plots the 30-day running average. Also, plotted is the solar activity as measured by the solar radio flux at 10.7 cm (grey). This index is a measure of the F10.7 cm radio emission which originates from the sun’s chromosphere and corona and is a well-established measurement of solar activity [NOAA, 2018]. The index is measured in “solar flux units” (sfu) which can vary from a low of ~ 50 sfu to above 300 sfu during the ~ 11 -year solar cycle. F10.7 cm correlates well with the number of sunspots and is easily measured by ground-based instruments. The black curve shows the 180-day smoothed F10.7 cm measurement from the daily values. It is interesting to note that the mean T_{OH} generally appears to

follow the solar activity as shown by the second-order polynomial and 30-day running smooth (red curve) to the mean T_{OH} measurements.

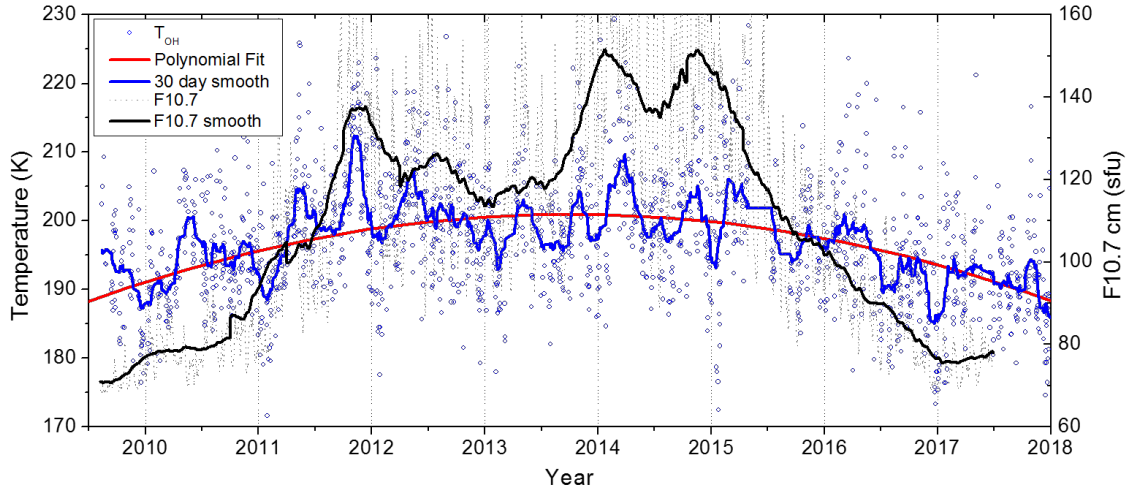


Figure 4.9. MTM nightly mean T_{OH} with a second-order polynomial (red) showing the long-term trend along with the observed (grey) and 180-day smoothed (black) solar activity as measured by F10.7 cm.

With the generally good agreement between the SABER T_k and ground-based OH temperatures (all with a bias of ~ 5 K), Figure 4.9 can be extended back in time to 2002 by using SABER data as a good proxy of OH temperature at 87 km. Focusing on ALO and using a stricter sample volume of $10^\circ \times 10^\circ$ box in both latitude and longitude, nearly 10,600 coincident events were obtained from January 2002 until May 2017. This provides 16 years of measurements, ~ 1.5 solar cycles, encompassing solar cycle 24. The results are shown in Figure 4.10 which plots the SABER T_k measurements as red dots. A 30-point (magenta) smoothing fit clearly identifies the SAO with similar amplitudes as those measured by the MTM. In the lower plot of Figure 4.10, the corresponding solar activity is shown as measured by the F10.7 cm solar index along with a 180-point smoothing curve (black line). A 180-point (red) smoothing is applied to the SABER data above for direct visual comparison. Also

visible in the black second-order polynomial fit is a similar longer-term variation that was identified in the MTM T_{OH} data in Figure 4.9 with a peak around 2014. There is a clear visible correlation between the SABER T_k and the solar activity over this extended period. It is evident that the solar minimum of 2009 matches the low temperature measured by both SABER and the MTM, and the solar maximum in 2014 matches the temperature peak seen in both instruments (See also Figure 4.9). In order to establish a correlation between the T_{OH} and T_k measurements and solar activity at least two solar cycles are necessary, but in the mean time, these figures are highly suggestive of such a correlation.

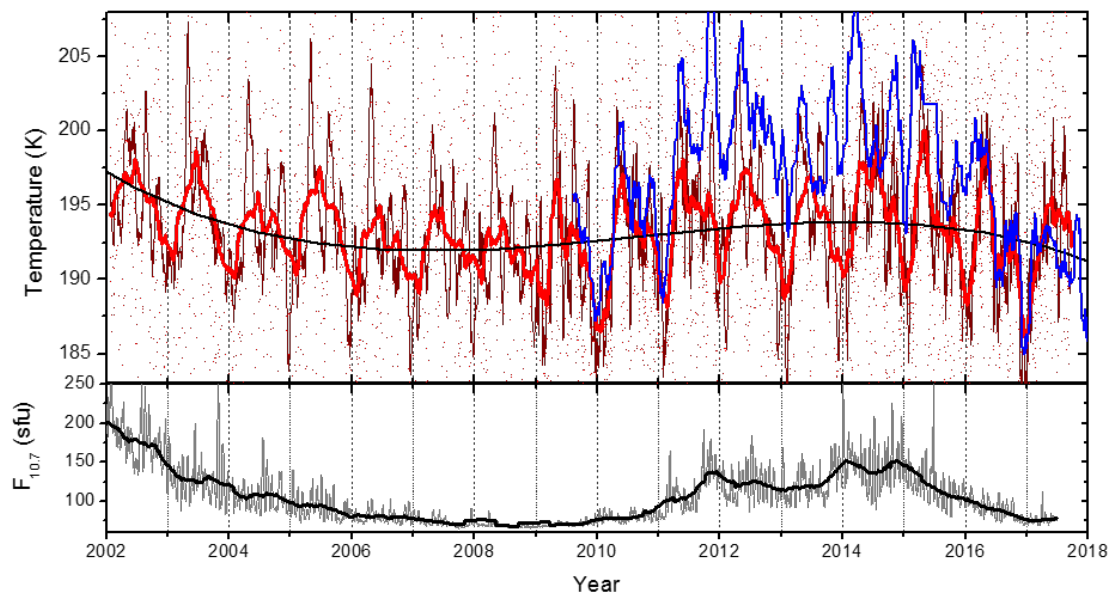


Figure 4.10. Nighttime SABER T_k 2002–2017 over ALO and the solar F10.7 index. The top plot shows T_k (red dots circles) 2002–2017 at ALO with a 30-point (magenta curve) and 180-point (red curve) smooth fits. The black curve is second order polynomial. The 30-night smoothing of the mean MTM temperatures is plotted in blue. The lower plot shows the solar activity given by F10.7 cm (grey) with a 180 point smooth (black).

With the information available and following the analyses of *Beig* [2011] and

Forbes et al. [2014] an initial estimate of the temperature dependence on the solar activity has been made. This was obtained by first removing contributions of the diurnal and semidiurnal tides, and then the composite year variability, as shown in Figure 3.8. From the nightly mean T_{OH} the temperature sensitivity can be determined. Figure 4.11 shows the residual temperatures derived from this analysis using the MTM (blue) and SABER (red) temperature data as a function of the solar F10.7 cm Index. The solar sensitivity, given by the linear fit, for the MTM data is 11.8 ± 0.6 K/100 sfu (shown by the blue line). The SABER T_k dependence on the solar cycle is 5.2 ± 1.8 K/100 sfu (shown by the red line). *Forbes et al.* [2014] studied the solar dependence of global SABER temperatures and reported that at 85 km altitude the SABER temperature dependence on solar activity was 3–6 K/100 sfu. Our SABER measurement is in agreement with these previous measurements. Although occasional higher values similar to our MTM results have also been reported [*Beig, 2011; Forbes et al., 2014*]. While observations longer than one solar cycle are needed to more accurately make a connection between the mesospheric temperatures and the solar activity, the correlation can begin to be seen and the climatology of the mesosphere can begin to be built. Additionally, ongoing measurements will continue to contribute to further insight into the solar dependence of the mesosphere T_{OH} observed.

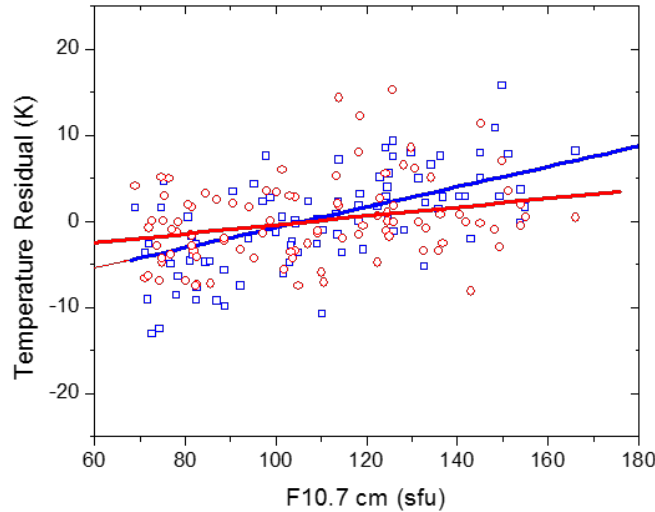


Figure 4.11. Dependence of the nocturnal mean T_{OH} (blue) and SABER T_k on the F10.7 cm index. Temperature sensitivity, S , is 11.8 K/100 sfu and 5.2 K/100 sfu, respectively.

4.4. Summary and Conclusions

There have been several comparison studies of satellite and ground-based mesospheric temperature measurements using a variety of instruments and techniques. In particular, SABER has provided over 16 years of altitude-resolved temperature data for investigating mesospheric temperature variability in the MLT region.

This chapter compares the MTM OH (6,2) rotational temperatures with the SABER kinetic temperatures. Eight years of observations from 2009–2017 have yielded over 3400 coincidence measurements within a $10^\circ \times 20^\circ$ latitude-longitude box centered over ALO. SABER measurements were height-weighted to the nominal OH emission layer peak of 87 km and layer thickness of 9.3 km, and then compared to the zenith 12-min averaged MTM T_{OH} .

In general, the results of the MTM comparison show that the ground-based temperatures derived using transition probabilities given by *Pendleton Jr et al.* [2000]

Table 4.3. Temperature Comparison Between SABER and Several Ground-based Instruments

Years	Location	ΔT (K)	Paper
2009–2017	Cerro Pachon, Chile (-30°S)	-5.5 ± 0.3	This Chapter
2003–2005	Wuppertal, Germany (51°N)	-7.5	<i>Oberheide et al.</i> [2006]
1998–2002	Sierra, Nevada (37°N)	-5.7	<i>López-González et al.</i> [2007]
2002–2004	Maui, Hawaii (20°N)	-5.2 ± 0.2	<i>Remsberg et al.</i> [2008]
2004–2005	Wuppertal, Germany (51°N)	-4.5 ± 0.5	<i>Mulligan and Lowe</i> [2008]
2004–2005	Maynooth, Germany (53°N)	-8.6 ± 0.8	<i>Mulligan and Lowe</i> [2008]
2002–2009	Davis, Antarctica (68°S)	~ -2	<i>French and Mulligan</i> [2010]
2011–2013	Ranchi, India (23°N)	$-4-5$	<i>Parihar et al.</i> [2017]
2002–2014	El Leoncito, Argentina (32°S)	-4.5 ± 0.2	<i>Reisin and Scheer</i> [2017]

and *Goldman et al.* [1998] are in good agreement with the retrieved satellite measurements over the eight years, both in their absolute values (within 5 K) and their night-to-night variability.

Specifically, it was found that the selected $10^\circ \times 20^\circ$ sample volume provided a large coincident data set while maintaining sensitivity to the local mesospheric temperature environment. The temperatures ranged from $\sim 160-230$ K and exhibited a mean ΔT of 5.5 K. The MTM T_{OH} are found to be warmer than the SABER T_k measurements, in good agreement with several prior studies at other latitudes as listed in Table 4.3 [e.g., *López-González et al.*, 2007; *Mulligan and Lowe*, 2008; *Oberheide et al.*, 2006; *Parihar et al.*, 2017; *Remsberg et al.*, 2008]. These results comprising data from numerous sites and several years all show that the 5 K offset is a remarkably consistent feature of the SABER data set over a range of latitudes, suggesting some systematic offset in the SABER results.

This said, the comparison of the SABER T_k with the MTM T_{OH} show periods of good agreement both in the day-to-day variability and the mean temperatures, but also periods of systematic differences. Assessing the comparability of SABER and MTM temperatures requires discussing the different measurements techniques of the instruments. Differences in the temperature may be due to the large discrepancy in the FOVs of the measurements. The SABER instrument has an instantaneous FOV of 2 km (vertically) by 24 km (horizontally) and uses a limb-scan from about 15 km to 110 km to acquire the tangent point temperature from a very long line of sight. It derives atmospheric temperature from the kinetic temperature of CO₂ IR emissions which include non-LTE considerations. *Remsberg et al.* [2008] reported that SABER derived temperatures were found to be 2–3 K too low in the mid-mesosphere from random error due to noise of 2 K at 85 km altitude and systematic error due to uncertainties in the abundance of CO₂ and non-LTE conditions of 4 K at 85 km altitude.

The MTM is stationary with a smaller instantaneous FOV used for comparison (5 km×5 km), and T_{OH} is a measure of the rotational temperature of OH molecules assumed to be in LTE with the atmosphere over a emission layer of slightly varying height and thickness. Detailed measurements have also determined seasonal changes in this offset possibly due to layer height changes associated with the SAO at ALO. Furthermore, the SABER OH equivalent temperature represent averages over an assumed emission height of ~87 km. These results suggest the OH emission layer moves vertically or distorts its shape, then the MTM observed altitude can differ by a few km from the SABER OH equivalent altitude, resulting in discrepancies in the measured temperatures.

Given the large differences in the instrumental fields of view and the differing techniques employed to determine the mesospheric temperatures the results are quite

remarkable and show the immense utility of using SABER data as a reference for coordinated satellite and ground-based measurements for climatological studies.

Comparison with earlier MTM and SABER studies at Maui have extended this investigation to over 15 years, establishing the MTM has maintained an accurate OH temperature measurement during this period with an average warm bias of ~ 5 K.

An intriguing long-term trend in the MTM data set was also discussed, which is visible in Figure 4.10. This trend matches the solar cycle with a solar sensitivity of 12 K/100 sfu, but the effects of planetary waves have not yet been removed from this data. This solar sensitivity is currently two times larger than most other reported solar sensitivities, while the solar sensitivity of the SABER T_k are in good agreement with other reported results [Beig, 2011; Forbes *et al.*, 2014]. Longer data sets are needed to investigate the solar influence on the OH temperature.

CHAPTER 5
MESOSPHERIC TEMPERATURE VARIANCE MEASUREMENTS OVER THE
ANDES MOUNTAINS

5.1. Introduction

Atmospheric gravity waves (GWs) perform an important function in the transfer of energy and momentum from the lower atmosphere to the middle and upper atmosphere. They affect the thermal structure of the MLT and the mean wind circulation. A better understanding of GW climatology is needed for accurate modelling of the atmosphere. GWs have a broad range of horizontal scales and they are a localized phenomenon driven by a variety of geophysical sources. This chapter uses variances of OH rotational temperature, T_{OH} , and relative band intensity, I_{OH} , as a proxy for GW activity. Following the methods of *Reisin and Scheer* [2004], who used ground-based measurements to study OH intensity and temperature variances at El Leoncito, Argentina (31.8°S, 69.2°W), and *Jiang et al.* [2002] who used satellite data to measure radiance variance lower in the troposphere and stratosphere, the MTM data are used to conduct a similar variance study of the mesospheric temperature.

5.2. MTM Variance Method and Data

The MTM data used in this study measured airglow OH (6,2) band intensity and T_{OH} variances in a zenith sample area of about 5 km×5 km at 87 km altitude. For further details about the instrument and data reduction, see Chapter 2. All nights with at least 4 h of data during the eight years of MTM data (12 August 2009 – 31 December 2017) are used in this study.

The measured OH rotational temperature variance (T'^2), or square of the standard deviation (σ^2) measured in K², assumed to be caused by GWs, is related to the GW potential energy (PE) in the atmosphere. Section 5.3.2 will discuss PE further

and show that PE is proportional to the square of the temperature perturbations, i.e., the variance. Much of this chapter naturally focuses on T'^2 rather than GW PE to characterize different wave scales because PE requires additional information such as the Brunt-Väisälä frequency, which is readily given by lidar measurements of the vertical temperature gradient, but is not always available.

5.2.1. Daily Variance Measurements

Figure 5.1 shows a typical nightly I_{OH} and T_{OH} time series containing a mixture of shorter-period GW and tide-like structures for UT day 212, (29–30 July) 2016 before and after the subtraction of the diurnal (24 h) and semidiurnal (12 h) tidal components using harmonic analysis as described in Chapter 3. Figure 5.1a shows that before the subtraction, the large-scale tidal features dominate. The mean T_{OH} (blue line) is 190 ± 1 K, and the associated variance 121 K^2 . The mean I_{OH} (red line) for the night is $(5.0 \pm 0.1) \times 10^4$ counts with a variance of $1.1 \times 10^8 \text{ counts}^2$. Figure 5.1b shows that after subtraction, the visible smaller-scale perturbations exhibit dominant periods of ~ 1 h and ~ 4 h with a T_{OH} (I_{OH}) variance of 6 K^2 (9.42×10^6), representing 5% (8%) of the unfiltered data variance. This illustrates the importance of the removal of the tidal components for GW variance studies. In the following analysis, only the diurnal and semidiurnal tidal harmonics are removed in order to facilitate the direct comparison with spectrometric measurements from nearby El Leoncito [Reisin and Scheer, 2004].

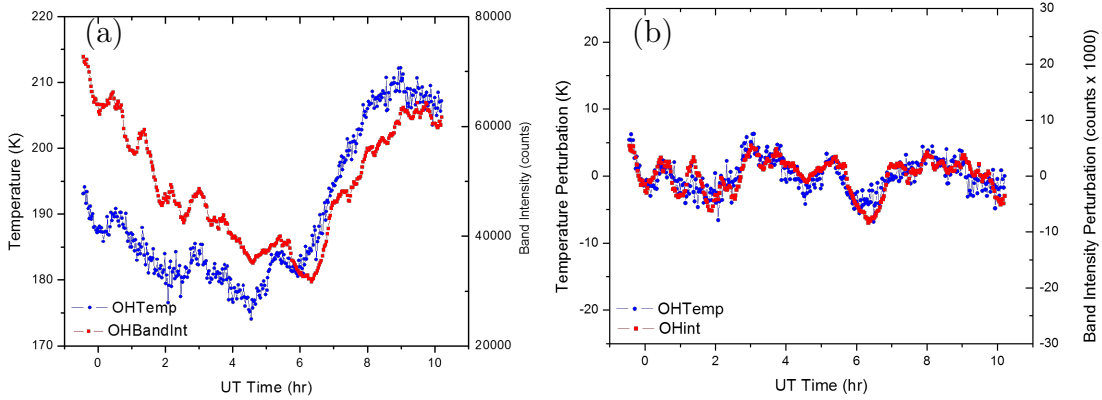


Figure 5.1. I_{OH} and T_{OH} for UT day 212, (29–30 July) 2016. Plot (a) shows the raw T_{OH} (blue line) and I_{OH} (red line). Plot (b) shows the T_{OH} and I_{OH} after the diurnal and semidiurnal tide components are subtracted.

As the amplitude of the wave is proportional to the relative variation of the intensity data, the large range of the nocturnal I_{OH} require the intensity variance to be normalized by the mean intensity. The T'^2 measurements are not usually normalized.

5.2.2. Annual Temperature Variance with Tides Removed

Figure 5.2a shows the total variance for the year 2014. The plot shows that from night to night there can be large changes in the temperature variance (grey curve) with peak values greater than 200 K^2 . This situation occurs in almost every month of the year. The average variance ranges from $30\text{--}80 \text{ K}^2$, with the highest sustained levels during the winter months, as depicted by the 30-day smoothing (blue curve). For comparison, Figure 5.2b plots the variances with the 24-h and 12-h tidal components removed. The highest values are now around 30 K^2 and the average variances range from $\sim 5\text{--}10 \text{ K}^2$. There is still a clear tendency for enhanced variance during the winter and extending into the spring months.

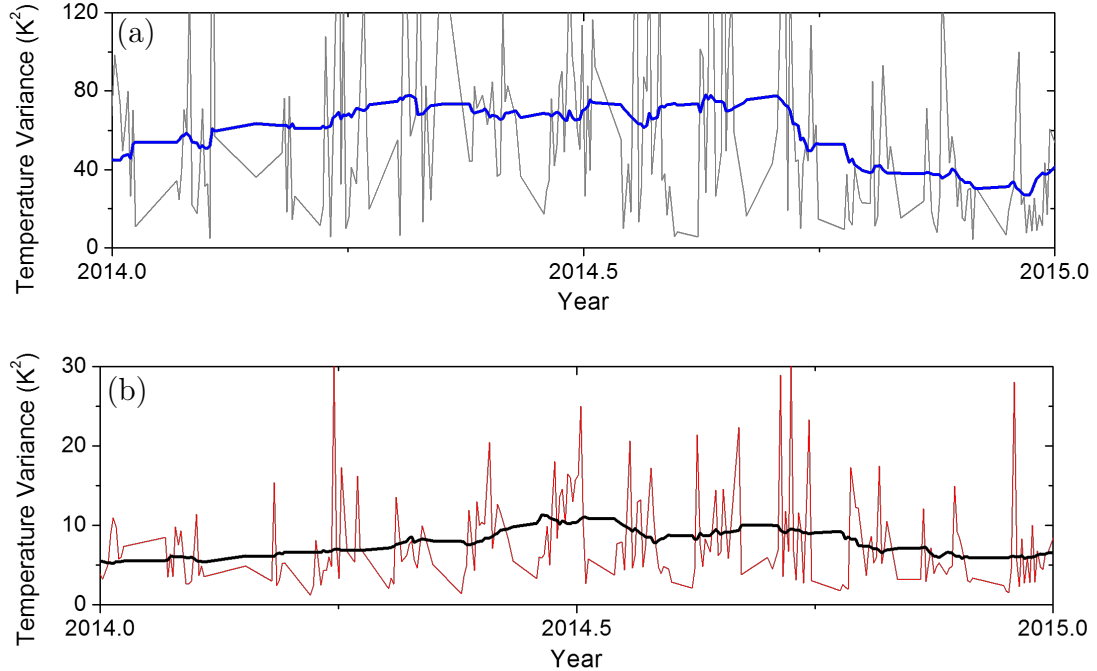


Figure 5.2. (a) Raw T'^2 (grey) for the year 2014 with a 30-day smoothing (blue), and (b) GW T'^2 measurements (red) with the 24 h and 12 h tides removed with a 30-day smoothing (black).

Figure 5.3 summarizes the tide-removed temperature variance for 6 consecutive years: 2010–2016, with 2015 omitted due to sparser data. Each one is plotted on the same scale to facilitate visible comparison of the seasonal differences of the consecutive years. All plots exhibit similarly ranged average variances of 5–10 K². A broad peak during the winter months is present in all plots, but is more pronounced in 2010, 2011, and 2016. A secondary peak in the spring months is also evident in most years. These results suggest significant interannual variability in the GW variance.

To investigate the interannual variability, Figure 5.4 plots the GW variance with the tides removed for all eight years. The plot clearly shows a strong annual variation in temperature variance during the course of each year and equally strong year-to-year variability in the magnitude of the variance. The plot also shows evidence for a

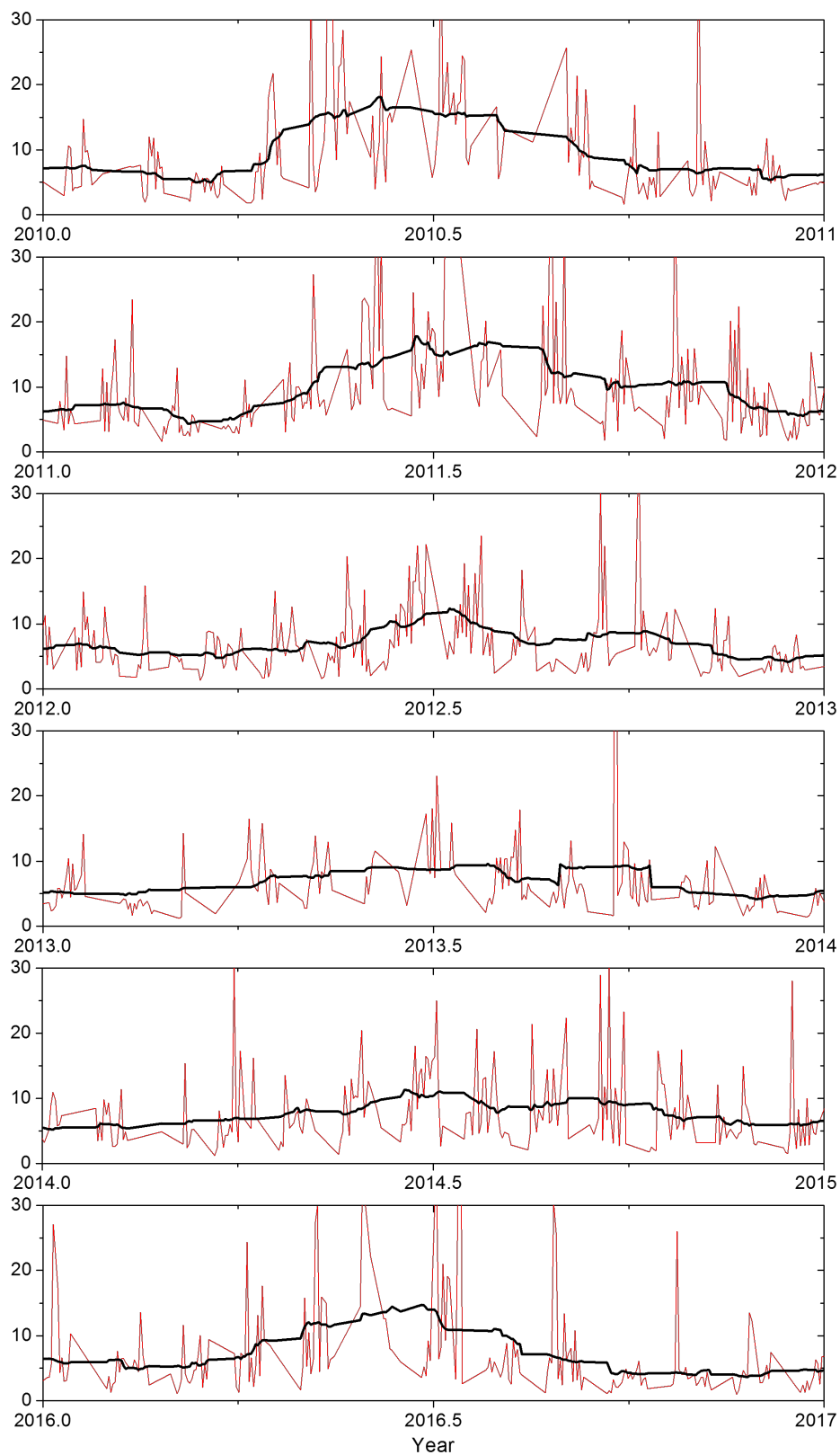


Figure 5.3. T^2 measurements (red) with the 24 h and 12 h tides removed for several years with a 30-day smoothing (black).

weaker secondary peak in most years as noted in Figure 5.3. Figure 5.4 confirms that the three years with enhanced temperature variance (2010, 2011, and 2016) were due to sustained increases in temperature variance, primarily during the winter months, as shown by the 30-point average fit (black curve).

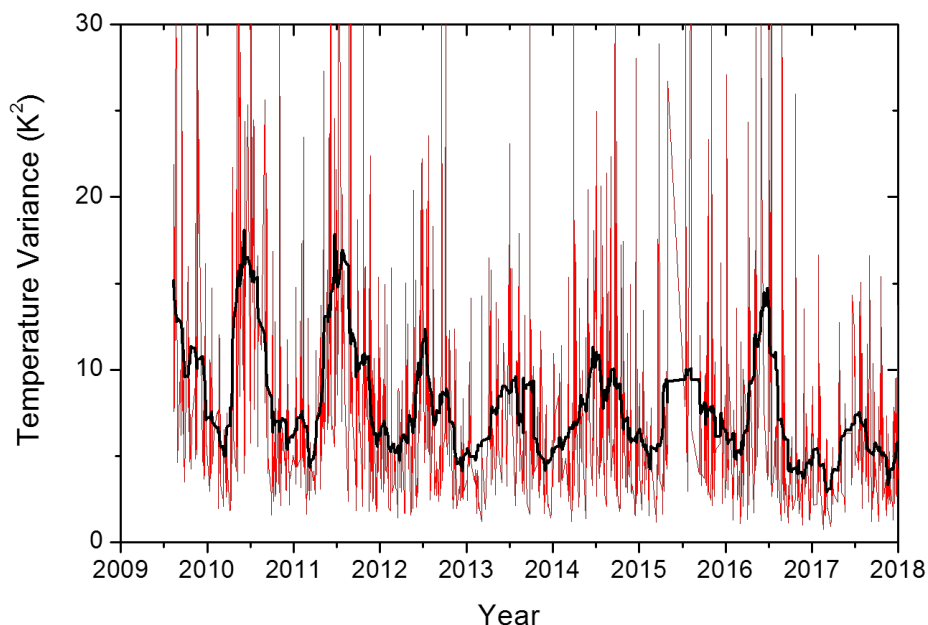


Figure 5.4. GW variance (red) with the tides removed for all eight years consecutively. The black curve shows a 30-point smooth.

Reisin and Scheer [2004] reported results from similar measurements of the zenith OH (6,2) I_{OH} and T_{OH} using a spectrometer. The measurements were made from El Leoncito Observatory, Argentina (31.8°S, 69.2°W) \sim 200 km SSE from ALO. Their results from January 1998 until September 2002 (four years) are shown in Figure 5.5, as a superposed annual plot. The dashed lines depict OH results (and the solid lines are O_2). The top panels show the total variance with tides, and the bottom panels are after the tides are removed. While their results also showed a strong winter annual enhancement, they reported primarily on the semiannual variation.

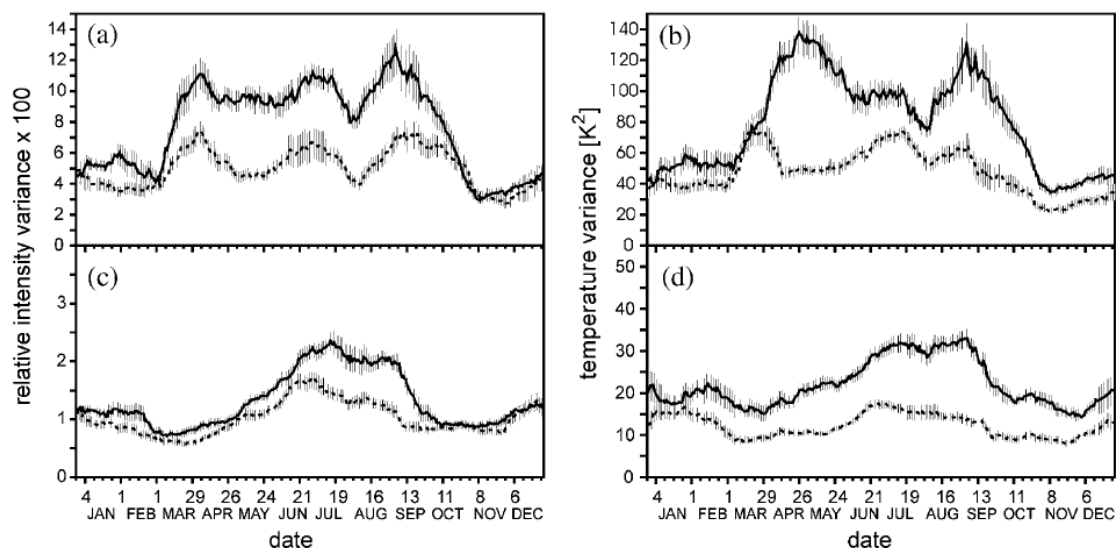


Figure 5.5. Average seasonal variance from nearby El Leoncito, Argentina (1998–2002) for OH (dashed line) and O₂ (solid line) shown by a 29-night running mean. The top plots include the tides, and the bottom plots show the data after subtraction of tides. Note the different vertical scales. Plots (a) and (c) show intensity variance; plots (b) and (d) show T'^2 [Reisin and Scheer, 2004].

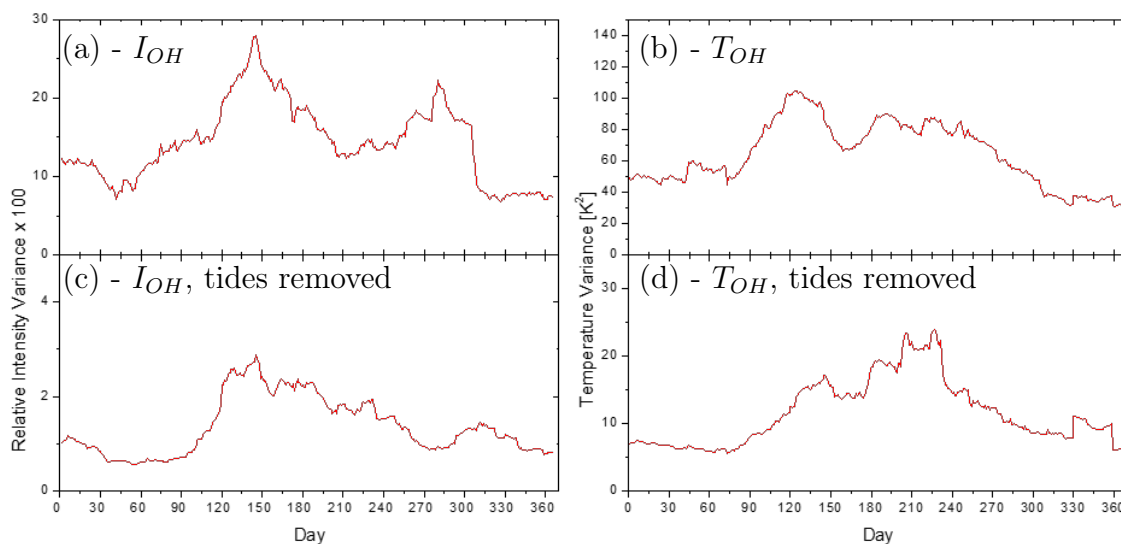


Figure 5.6. Composite year of the MTM OH variance data (2009–2017). The curves show 30-night running means to the measurements. The top plots are the raw measurements including the tides, and the lower plots show the data after the subtraction of tides. Note the different vertical scales. Plots (a) and (c) show I_{OH} variance, plots (b) and (d), T_{OH} variance.

For comparison, the MTM 8-yr results are plotted in Figure 5.6 in the same superposed format and with the same scales as the El Leoncito results. The plots show a 30-day running mean of both the raw geophysical variance and the variance after the subtraction of the two tidal components. The plots on the left side (a and c) show the relative I_{OH} variance and the plots on the right side (b and d) show the T_{OH} variance. The top plots include the tides, while the bottom plots show the variance once the 24 h and 12 h tidal components have been subtracted. Note that the y-axis (ordinate) of the top plots are scaled 5–6 times larger than the bottom plots due to the tidal contributions. GW variance accounted for only 18% of the total T'^2 , and only 10% of the total intensity variance. With the tides included, the variance has an apparent annual signature with enhanced variance during the winter months. With the tides removed, the GW variance also shows semiannual behavior with peaks in the Austral Fall (May) and the Austral Spring (November) (Figures 5.6c, 5.6d). This is highly consistent with results from *Reisin and Scheer* [2004], and with previous MTM temperature results as reported in Chapter 3. In each case, the main maxima of the variance plots are broad and occur during the austral winter. The intensity maximum peaks a month before the solstice and temperature peaks about a month after the solstice.

The relative scales of the OH intensity and temperature, i.e., the ratio of mean amplitude of the I'^2 to the mean amplitude of the T'^2 , depend on the airglow response to GWs. This relationship is referred to as Krassovsky's ratio, denoted by η , is usually applied to individual GWs, and is given by [*Krassovsky, 1972*]:

$$\eta = \frac{I'/\bar{I}}{T'/\bar{T}} \quad (5.1)$$

where I'^2 and T'^2 are the normalized intensity variance and the absolute temperature variance respectively, and the bar represents the mean value. Assuming the same

waves are involved in both measurements of intensity and temperature, *Reisin and Scheer* [2004] applied this ratio to the nocturnal temperature and intensity data to investigate the airglow response to an ensemble of GWs with differing variances. Figure 5.7 plots the distribution of nightly η values derived from the MTM data for the 8-yr program. The average $\eta = 6.0 \pm 0.1$, and the few nights that have larger η values than ~ 14 were all found to be associated with very small temperature perturbations. Our MTM results are in good agreement with $\eta = 5.6 \pm 0.1$ as previously determined by *Reisin and Scheer* [2004] (no comparative plot available).

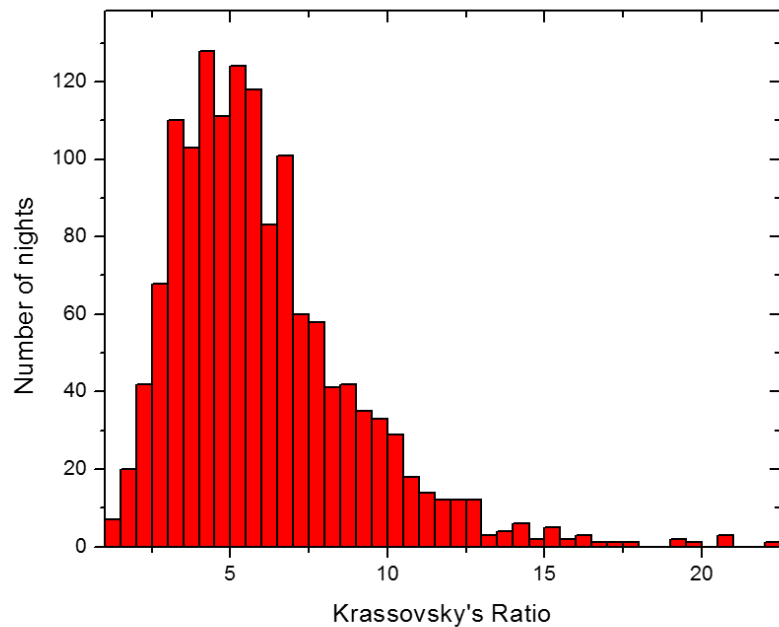


Figure 5.7. Distribution of nightly η values for all nights (2009–2016). Mean value is 6.0 ± 0.1 and the right end of the tail is due to low values of T' .

5.2.3. Contribution of Small-Scale Waves to Temperature Variance

The influence of smaller-scale GWs on the variance can be quantified from night-to-night helping to understand their contributions to the overall seasonal variance. To investigate this, Butterworth bandpass filters are applied to the nightly temperature

data. The variance of the temperature fluctuations are measured from the results of the filters: <1 h, and >1 h. Figure 5.8 shows the results of this filtering applied to the temperature data for the night of 30 July 2016. The temperature is demeaned from the temperature 190 K. The raw OH temperature data are shown by the black curve and is the same as shown in Figure 5.1, where large-scale tidal features were reported in addition to small-scale perturbations. The red curve shows filtered temperature fluctuations due to GWs with periods <1 h and has a variance of 4 K^2 . The magenta curve closely tracking the raw data is the low-pass filtered temperature perturbations showing all the wave activity with periods >1 h and has a large variance of 115 K^2 . Within the limits of the analysis, the red curve (<1 h data) when added to the magenta curve (>1 h data) recreates the raw data well. Due to the limits of the filters and length of the nightly data sets, the magnitudes of the large-scale wave variances are found to be underestimated using this basic technique.

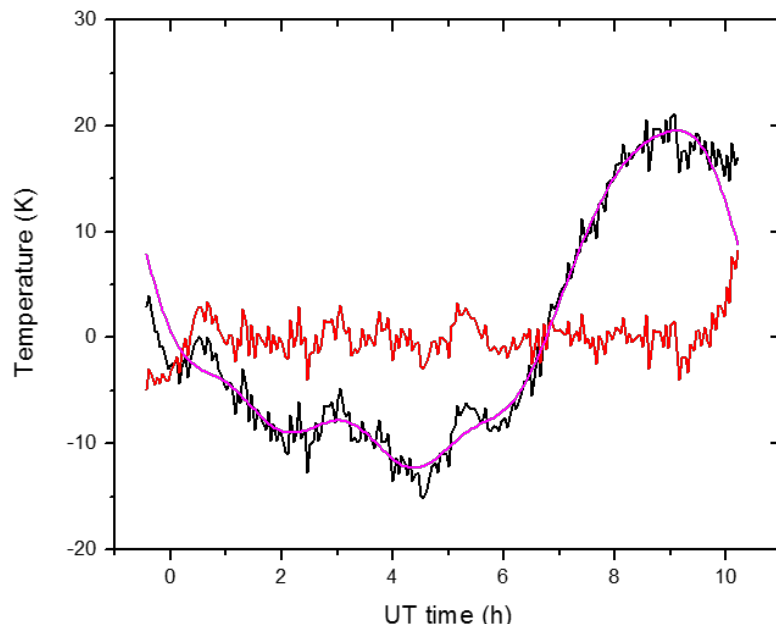


Figure 5.8. Example of bandpass filter subtraction for 30 July 2016. Demeaned data (solid black line), with band ranges: <1 h (red) and >1 h (magenta).

To quantify the seasonal small-scale GW contribution, the <1 h bandpass filter is applied to each night of data during the years 2012–2017. The results are superposed into one year and the 30-day running smooth fit is plotted as the red curve in Figure 5.9. The results exhibit an annual trend with a peak in the winter months. The black curve plots the average seasonal variance with tides removed (same as Figure 5.6d). The small-scale GWs (periods <1 h) contribute over 60% of the observed temperature variance due to all GWs once the diurnal and semidiurnal tidal components are removed showing the small-scale GWs contribute significantly to the seasonal GW variance. The enhanced variance measurements during the winter months appear to be in good agreement with an extensive study reported by *Offermann et al.* [2009], that examined the seasonal dependence and relative importance of different scale sizes of atmospheric waves (GWs, planetary waves, and tides) and concluded that the variance was significantly influenced by GWs.

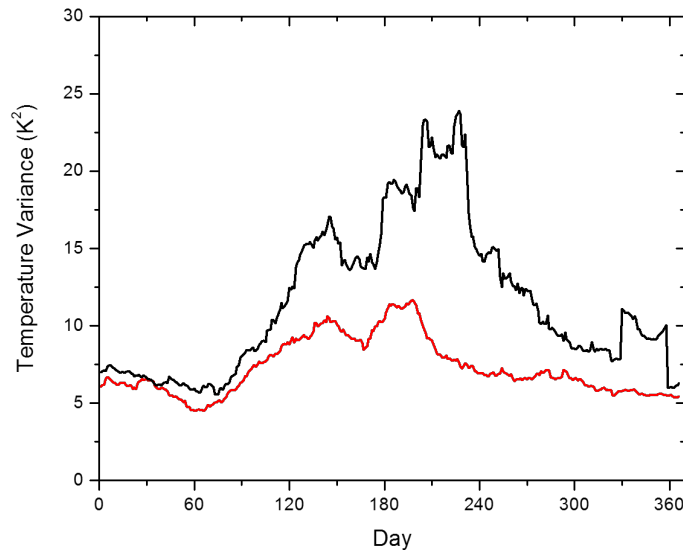


Figure 5.9. Average seasonal variance based on scale of GW. The black curve shows the average seasonal variance with tides removed (same as Figure 5.6d), and the red curve shows average seasonal variance for GWs with periods <1 h.

5.3. SABER Variance and Potential Energy Measurements

Thirteen years of SABER v2.0 data (2002–2015) are analyzed to independently investigate GW activity over ALO using measurements of mesospheric temperature variance and GW PE. Details about the SABER instrument on the TIMED satellite are given in Chapter 4. Following the methods of *Liu et al.* [2014], *John and Kumar* [2012], and *Preusse et al.* [2002], temperature profiles are used to extract fluctuations induced by GWs. The background temperature and mean trends were first removed by applying a least-square fit to subtract contributions from zonal wavenumbers 0–6 from all of the daily 24 h profiles falling in the 5° latitude bin centered over ALO. The wavenumber 0 corresponds to the zonal mean temperature, while wavenumber 1–6 correspond to the diurnal, semidiurnal, etc. tides with wavelengths being harmonics of the zonal belt.

Descending and ascending scan modes of SABER were analyzed separately to account for and remove diurnal tides. In this way GWs are isolated from the zonal mean, planetary waves, and breaking planetary waves [*Ern et al.*, 2006]. The removal of the large-scale waves and mean background from the raw profiles (Figure 5.10a) revealed the fluctuations due to GWs (Figure 5.10b) allowing further investigation using the T'^2 and GW PE [e.g., *John and Kumar*, 2012; *Liu et al.*, 2014; *Pugmire*, 2015; *Yamashita et al.*, 2013].

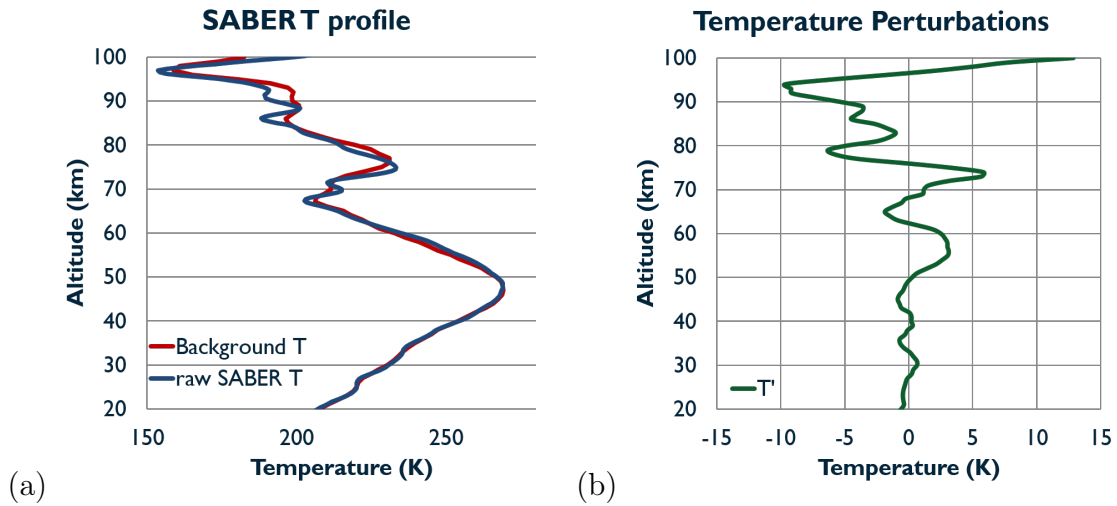


Figure 5.10. The process to reveal GW fluctuations from SABER temperature profiles. (a) Plot shows an example SABER raw temperature profile (blue line) and the mean background profile (red line). (b) The difference (green) is plotted to show the temperature perturbation attributed to the vertical propagation of the GWs.

5.3.1. Comparison of SABER and MTM Temperature Variances

The T'^2 measurements height-weighted to 87 km for all SABER temperature profiles within a $5^\circ \times 10^\circ$ box centered on ALO are presented in this study. Figure 5.11 plots the SABER measured temperature variance (black) together with the MTM measured T'^2 for five years (2010–2015). The red curve depicts MTM results for red: <1 h, while the blue depicts the GW variance results for <4 h. Comparisons of these results reveal the same basic annual structure for both the SABER and the MTM variances. Furthermore, the amplitude of the SABER variance agrees well with the MTM variance for all GWs <4 h. Considering these results were obtained from two independent data sets with differing FOVs, data lengths, and different methods used to derive the variance, these results are very promising and clearly establish the broad periodic wintertime enhancement of the variance over the Andes. Furthermore, the analysis shows that the wintertime enhancement is mainly due to small-scale GW activity. The SABER mesospheric variance also shows enhancements throughout the

year which vary from year-to-year. These differences may be due to differences in the observable wave spectrum based on each methods and the assumption of constant 87 km height of the OH layer.

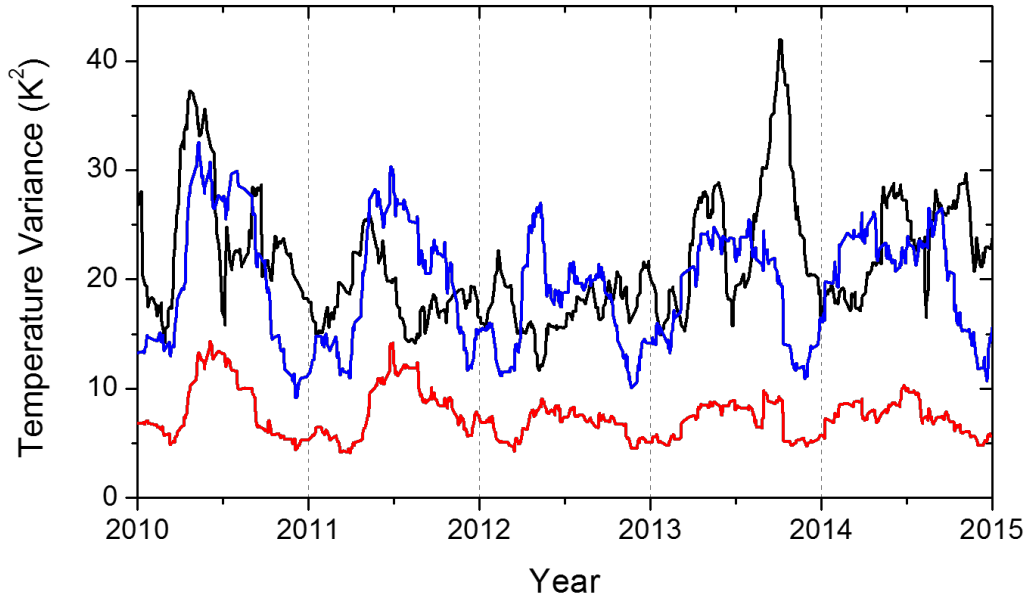


Figure 5.11. Comparison of the SABER measured temperature variance (black) with the MTM measured T'^2 (<1 h period: red, <4 h: blue) for 5 years (2010–15). Differences may be due to different observable wave spectrum based on each methods.

5.3.2. SABER Potential Energy Measurements

Having established robust comparable temperature variances using both the SABER and MTM temperature measurements, the associated GW PE can be calculated using [e.g., *Alexander et al.*, 2011]:

$$PE(z) = \frac{1}{2} \left(\frac{g}{N(z)} \right)^2 \left(\frac{T'(z)}{\bar{T}(z)} \right)^2 \quad (5.2)$$

$$N^2(z) = \left(\frac{g}{\bar{T}(z)} \right) \left(\frac{g}{c_p} + \frac{\partial \bar{T}(z)}{\partial z} \right) \quad (5.3)$$

where g is gravity at a given altitude, z ; N is the buoyancy frequency or the Brunt-Väisälä frequency in terms of temperature, T , as given by equation 5.3; and c_p is the heat capacity of dry air at a constant pressure. The T' indicates the temperature perturbation from the mean temperature, \bar{T} (the temperature variance is T'^2). If a single wave is propagating vertically in a simple atmosphere, with a constant background wind, then its potential energy per unit mass increases exponentially with altitude due to the decreasing density in order to conserve energy. A departure from the exponential growth of the PE can be identified as the altitude range where the single GW breaks or reflects, losing energy.

Figure 5.12 shows the monthly mean GW PE measured in J kg^{-1} calculated using 13 years of SABER data and superposed into a single year and quantifies the annual wave variability over the Andes Mountains. While significant variability was observed in PE from year to year (not shown), the superposed plot firmly establishes the seasonal and altitudinal structure. Note the strong enhancement during the winter months.

Figure 5.13 replots Figure 5.12, the PE as a function of month for different selected altitudes (10 km steps) from the stratosphere into the MLT region. In the upper stratosphere the peak of GW activity clearly occurs during the winter months. With increasing altitude the seasonal winter structure changes from annual more into a semiannual oscillation (e.g., 75 km and 85 km) with peaks in the summer and winter and minimums occurring in the spring and fall.

Finally, Figure 5.14 plots the vertical profiles of the PE in log scale derived from SABER for each of the four 3-month seasons: winter (blue line), spring (cyan line), summer (red line), and fall (green line). The solid black line shows conservative

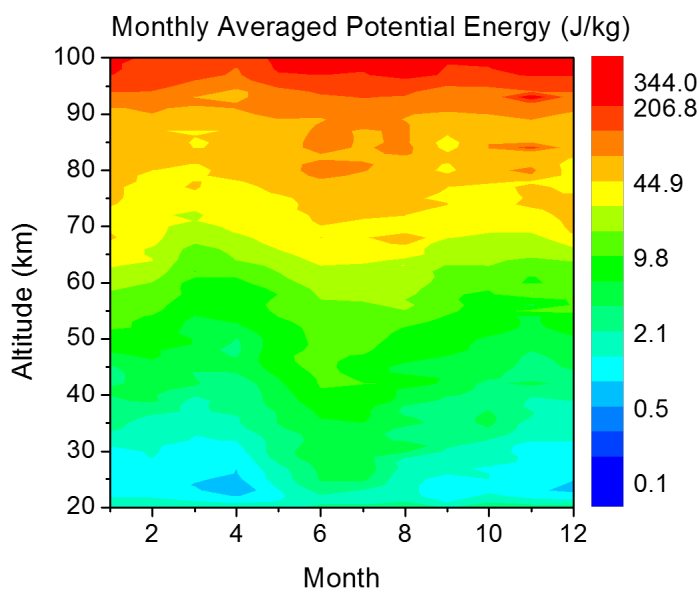


Figure 5.12. Contour plot showing the monthly mean GW PE plotted for 13 years (2002–2015) superposed into one year. The color bar is in J kg^{-1} . Note the enhancements during the winter months.

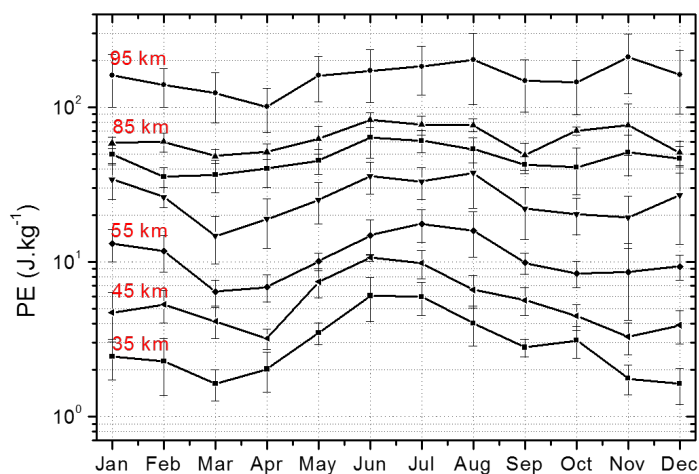


Figure 5.13. Average cycle of the GW potential energy over ALO taken at 10 km intervals throughout the stratosphere and mesosphere. The error bars represent 1σ uncertainty in the mean. Note the y-axis is in logarithmic scale.

growth, or the line a GW would follow as it grows in amplitude with a constant scale height of 7 km. Spring, summer, and fall show profiles that generally match the conservative growth line until they reach an altitude of 70 km, at which point they bend away from the curve indicating the location of wave dissipation. The wintertime profile (blue) has more PE and breaks at intermediate altitudes (shown as kinks), as well as at ~ 70 km altitude. In particular, the lower altitudes suggest increased wave breaking activity during the winter. Secondary waves may be created at these critical layers where waves break and then propagate into the MLT [Bossert *et al.*, 2017].

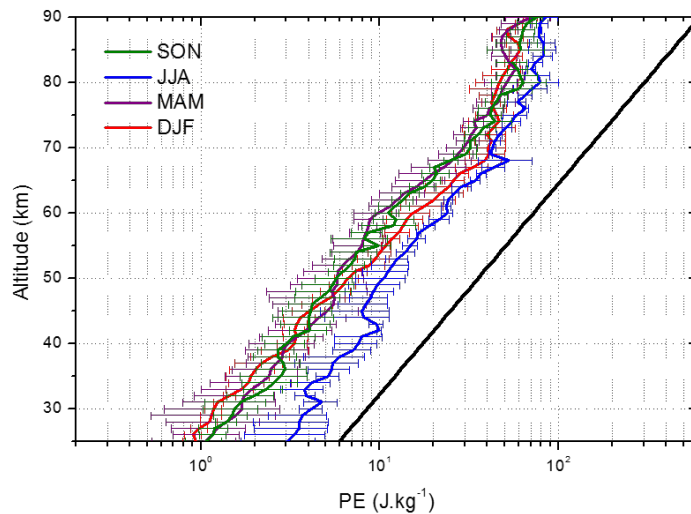


Figure 5.14. Vertical profiles of potential energy derived from SABER averaged over each 3-month season: winter (blue line), spring (cyan line), summer (red line), and fall (green line). The conservative growth line with a 7 km scale height is the black line. The error bars represent one sigma uncertainty in the respective mean values. Note the x -axis is in logarithmic scale.

Mzé et al. [2014] reported results from 16 years of GW PE measurements using a lidar in Southern France (43.9°N) and also found an annual cycle in the stratosphere and an SAO at higher altitudes, up to 75 km, with a stronger peak in the summer. In contrast, at ALO the SAO shows the strongest peak in the winter, as also confirmed

from SABER. *Mz  et al.* [2014] also reported dissipation of GWs at a similar altitude of 70 km with relatively little dissipation at lower altitudes. This suggest that ALO is a more active GW site during the winter months.

5.4. Summary and Conclusions

These coordinated temperature variance and GW PE observations using data recorded over several years consistently reveal increased wave activity over the Andes during the winter months. The MTM results show that GW activity is different from the tidal activity, in both seasonal trends and scales. The analysis demonstrates the importance of removing tidal signatures from the raw data, as best as possible. The results also confirm the strong night-to-night variability of GW activity at ALO, as reported by *Reisin and Scheer* [2004]. While the overall seasonal variation is semiannual, we find that the winter peak is larger than the summer peak. The ratio of the intensity and temperature variances for the OH emission have Krassovsky’s η values of 6.1 ± 3.0 , consistent with previous results [*Reisin and Scheer*, 2004]. Two separate methods of measuring the T'^2 were used for this study to quantify the GW contribution to the variance both involving removal of the large-scale tidal contributions using different filtering techniques: harmonic analysis of MTM data and filtering of the SABER vertical temperature profiles. Both methods reveal a main winter peak in GW activity with similar magnitudes. In addition, the bandpass filter analysis of the MTM data determined the significant contribution of the short-period GWs (< 1 h). The superposed GW PE data obtained from SABER measurements firmly establishes the seasonal structure evolving with increasing altitude from annual to semiannual with peaks in the summer and winter and minimums occurring in the spring and fall. Plots of GW PE show strong signs of wave breaking in both the stratosphere and mesosphere during the winter.

The enhanced variance of the temperature and GW PE during winter months is

in good agreement with other results [e.g., *Offermann et al.*, 2009], who concluded the variance was influenced primarily by GWs. The next chapter will investigate the winter months to quantify the terrain-generated GW's or mountain wave's contribution to this wintertime enhancement.

CHAPTER 6

OBSERVATIONS OF MESOSPHERIC MOUNTAIN WAVE STRUCTURE AND DYNAMICS OVER THE ANDES

6.1. Introduction to Mountain Waves

This chapter is a study of Mountain Waves (MWs), which are of high scientific interest and a major reason for locating the ALO in the Andes Mountains. MWs are a specific type of GW that occur when strong winds blowing over mountains generate standing waves, which can persist for several hours to several days [*Smith et al.*, 2009]. MWs have been measured penetrating into the stratosphere above a number of prominent mountain ranges in Alaska, Chile, Argentina, Greenland, Scandinavia, and New Zealand for quite some time [e.g., *Alexander and Teitelbaum*, 2007; *Alexander et al.*, 2009, 2013; *Eckermann and Preusse*, 1999; *Grimsdell and Alexander*, 2016; *Jiang et al.*, 2002, 2004; *Preusse et al.*, 2002; *Torre et al.*, 2012; *Wit et al.*, 2017]. In stark contrast, observations in the mesosphere have been much more limited. One of the prime reasons to operate the MTM as part of the ALO suite was to observe the occurrence, structure, and dynamics of mesospheric MWs as they perturb the OH airglow at 87 km. The strong flow of air over the Andes, particularly in the winter months, provides a strong source for MWs and makes ALO an ideal location for MW studies [*Jiang et al.*, 2002].

6.1.1. Linear Mountain Wave Theory

In Chapter 1, the equations of motion for Linear GW Theory were discussed. Equations 1.5–1.8, predict that the vertical displacement of a wind flow almost always leads to the generation of GWs. Terrain-generated GWs are created when stably stratified wind flows over topography such as mountains, hills and ridges as well as depressions such as basins, and canyons. There are two types of terrain-generated

waves: lee waves and MWs [Nappo, 2002]. Lee waves propagate downwind, or on the lee side of the ridge, and cause dangerous turbulent vortices or rotors. Lee waves are trapped close to the ground due to stable layers above and are a lower atmosphere phenomenon. MWs or orographic waves are terrain-generated GWs that can propagate upwards into the middle and upper atmosphere transporting significant amounts momentum and energy [Nappo, 2002]. MWs are stationary relative to the obstacles that generate them. For this to be, the obstacle exerts a force in the form of "stress" or wave drag on the background flow of the atmosphere. Wave drag's main effect is that it reduces flow velocities. The spectrum of MWs matches the spectrum of the widths of the terrain that generate them. The amplitudes of MWs are proportional to the amplitude of the terrain as illustrated in Figure 6.1. MWs are also known to be a contributor to the formation of mother-of-pearl clouds or polar stratospheric clouds [e.g., Alexander et al., 2013; Dörnbrack et al., 1999].

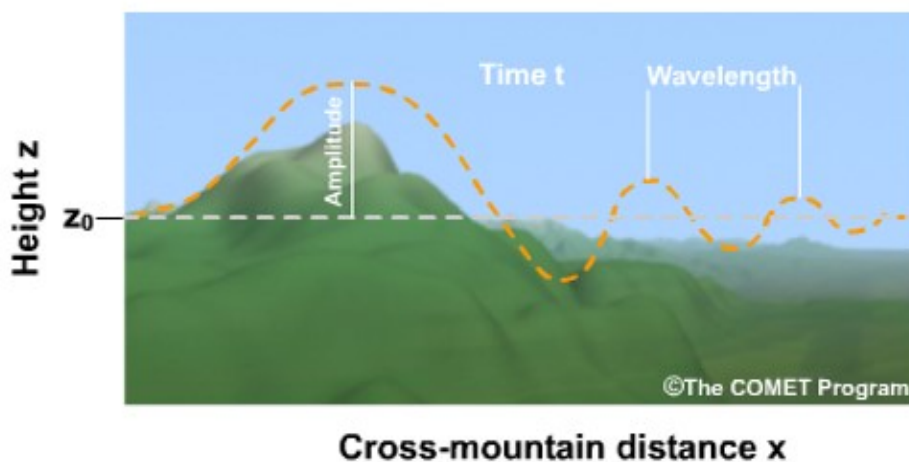


Figure 6.1. Stably stratified air is lifted over mountains and oscillates about its equilibrium height on the lee side of the mountain, producing stationary waves [Courtesy of the COMET Program].

MWs are stationary in relation to the ground and have an observed horizontal

phase speed of zero, $c = 0$. Like GWs, MWs develop and grow in amplitude as they propagate upward into the atmosphere and eventually saturate. This breakdown results in turbulence as shown in Figure 6.2.

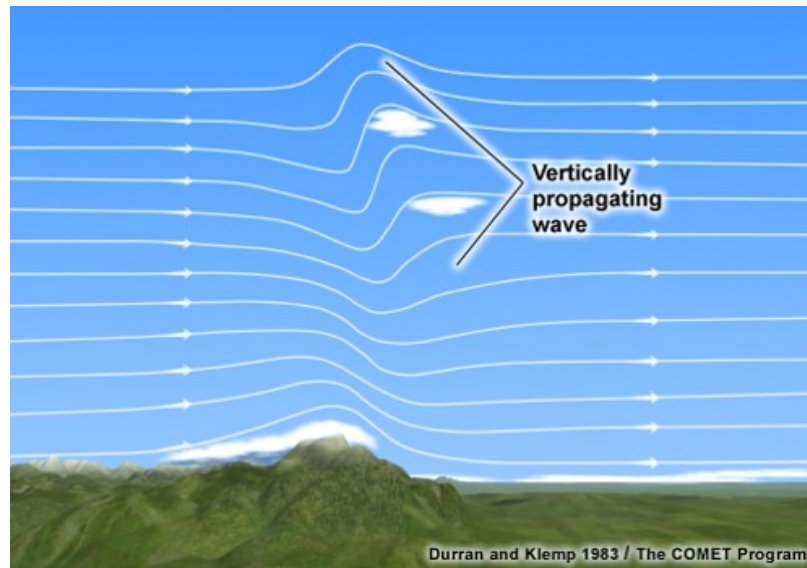


Figure 6.2. Depiction of the vertical propagation of MWs showing their largest amplitudes happen well above the mountains. Turbulence occurs when amplitudes grow too large and waves break [Courtesy of the COMET Program].

MWs are fixed in space, i.e., the observed wave frequency is zero, $\omega = 0$. Thus the intrinsic frequency becomes $\Omega = \omega - ku_o = -ku_o$. However, relative to the background flow of wind, u_o , the wave must be propagating upwind at the same speed as the wind ($c_I = -u_o$, where c_I is the intrinsic phase speed).

Following *Nappo* [2002], the simplest MW problem is a constant two-dimensional wind flow over a corrugated surface with constant stratification. The MWs are generated over the surface and propagate energy upward. So the *Taylor-Goldstein* wave equation gives a dispersion relation of

$$m^2 = \frac{N^2}{u_o^2} - k^2. \quad (6.1)$$

If $k < N/u_o$ then the right-hand side is positive making m real corresponding to vertically propagating stationary waves [Nappo, 2002].

The investigation of the impact of MWs on background wind is performed by looking at GW-critical level interactions. A critical layer occurs when the background wind vector, u_o , is equal to GWs horizontal phase velocity, c_I . At the critical layer, the GWs cannot propagate upward anymore. For a MW this occurs at the zero-wind line where the MW breaks, creates turbulence, and deposits its energy into the background flow [Worthington and Thomas, 1996]. In the summer months the wind changes direction from eastward to westward, thus crossing the zero-wind line and filtering out MWs around the tropopause (~ 20 km), as shown in Figure 6.3. In the winter months the zonal winds, u , are eastward at all altitudes up to the mesopause, i.e., no zero-wind line, allowing MWs to propagate upwind (westward) to high altitudes above the OH layer (~ 100 km). This is also the reason many observed GWs are monochromatic despite a large spectrum of possible waves being generated; only certain phase speeds can make it to the MLT region to be observed. Obtaining lower atmospheric wind conditions from such measurements as radiosondes are important for investigating the propagation of MWs.

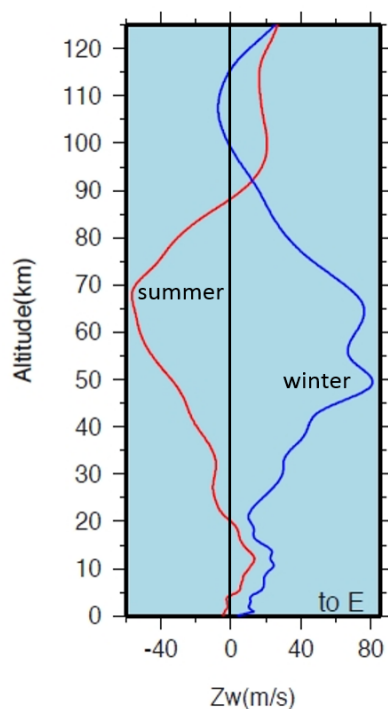


Figure 6.3. Plot showing seasonal zonal wind speed profiles. Note in the summer (red) the wind crosses the zero line in the lower atmosphere and filters out the MWs but in the winter (blue) it does not. Adapted from *Evers and Dost* [2010].

6.1.2. Observations and Models

Several observation techniques have been used to study MWs over the past thirty years in the stratosphere including radiosonde soundings [*Bacmeister et al.*, 1990; *Vincent and Joan Alexander*, 2000; *Yoshiki and Sato*, 2000], rockets [*Eckermann*, 1995], lidar [*Whiteway and Carswell*, 1995], radar [*Gavrilov et al.*, 1996; *Worthington and Thomas*, 1996], aircraft [*Eckermann et al.*, 2016; *Nastrom and Fritts*, 1992], and satellites. Space-based instruments used to study MWs with lidar, infrared and microwave scanning instruments include the Limb Infrared Monitor of the Stratosphere (LIMS) [*Gille and Russell*, 1984], MLS [*Jiang et al.*, 2002, 2004], CRISTA [*Preusse et al.*, 1999], CALIOP [*Alexander et al.*, 2013], Constellation Observing System for Meteorology, Ionosphere, and Climate (COSMIC) global positioning system

radio occultation (GPS RO) [Torre *et al.*, 2012], and Atmospheric Infrared Sounder (AIRS) [Alexander and Barnett, 2007; Alexander and Teitelbaum, 2007; Grimsdell and Alexander, 2016]. Each of these methods gives valuable information on MWs and their properties.

For example, CRISTA temperature perturbation data revealed enhanced wave activity over many mountain ranges. Eckermann and Preusse [1999] used CRISTA temperature profile measurements to detect the presence of MW in the stratosphere and their breaking over the Andes Mountains. The breaking waves drag on the atmosphere slowing the background flow until the horizontal wind speed was zero, creating a critical layer where both the vertical wavelength and the temperature perturbation vanished and prevented further penetration of MW energy.

It is difficult to determine all of the detailed properties for wave events observed from satellites. Most satellite studies in the literature have reported averaged temperature variances ($T' ^2$), and then MW sources were inferred on the basis of proximity to topography and zonal wind measurements. Jiang *et al.* [2002] used over two years of MLS radiance measurements and showed that the variances had strong annual variability over the Andes Mountains with enhancements during the winter months (see Figure 6.4a). These results matched model results and were associated with the right background wind conditions for the generation and propagation of MWs. The enhanced variances in the winter months happened when the winds were both eastward and the MW critical layers were absent. The annual variation of MLS radiance variance were also in good agreement with radiosonde data (see Figure 6.4b) and the Mountain Wave Forecasting Model [Bacmeister, 1993; Bacmeister *et al.*, 1990, 1994; Eckermann *et al.*, 2004].

Smith *et al.* [2009] was the first to report optical observations of MWs in the mesosphere using O, Na, and OH airglow emissions and to measure their properties.

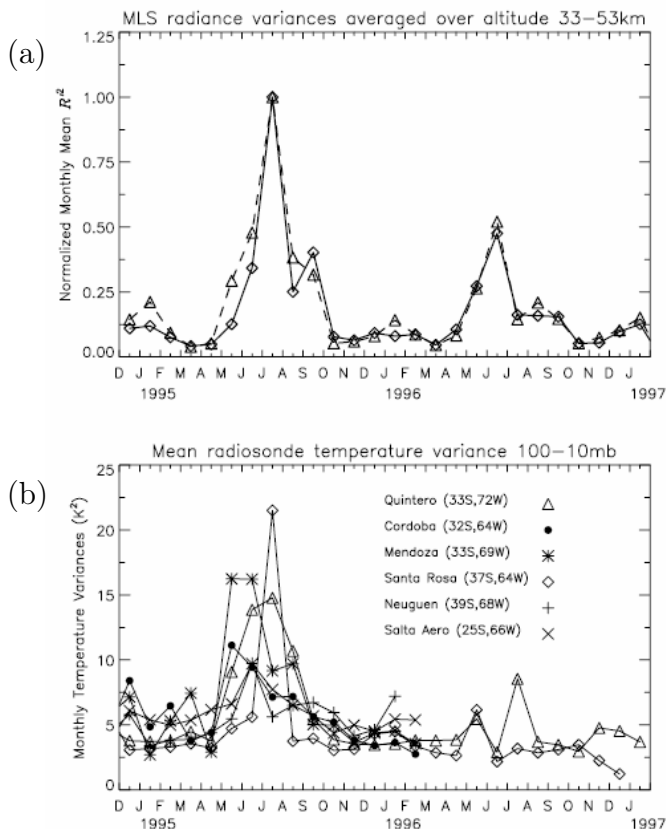


Figure 6.4. (a) Monthly mean MLS radiance variance measurements and (b) monthly temperature variance measurements over the Andes for two years (1995–1996). The monthly temperature variances in (b) are averaged between 100–10 mb (~ 16 –25 km) and taken from measurements from six radiosonde stations in/near the Andes [Jiang *et al.*, 2002].

The observations were made at the El Leoncito Observatory (31.8°S , 69.2°W), Argentina, close to ALO but further on the lee side of the Andes. Figure 6.5 shows the all-sky time-averaged OH images on three successive nights (2–4 July 2008), each obtained from averaging ~ 60 images over a ~ 11 -h period. The FOV is 535×535 km. Prominent in each image are MWs with a mean λ_H of 36 ± 2 km, as seen by the stationary nature of the waves along with their general North-South orientation parallel to the Andes Mountain Range. MWs have also been reported more recently in the mesosphere over New Zealand [e.g., Bossert *et al.*, 2017; Fritts *et al.*, 2016; Heale

et al., 2017; *Taylor et al.*, 2018] and over isolated islands in the Southern Ocean [*Eckermann et al.*, 2016; *Pautet et al.*, 2016].

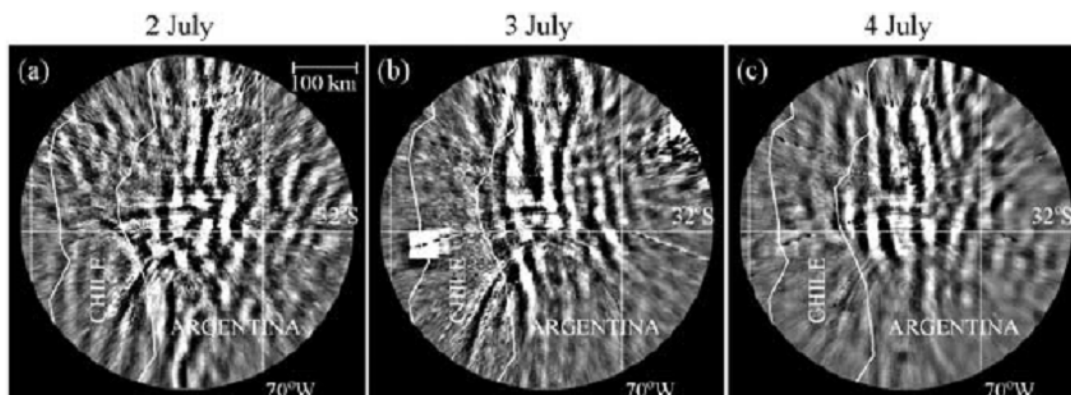


Figure 6.5. All-sky time-averaged OH images each obtained from averaging ~ 60 images during the ~ 11 hr night on three successive nights (2–4 July 2008). The FOV is 535×535 km. Each image features stationary MW structures with orientation parallel to the Andes Mountain Range [*Smith et al.*, 2009].

6.2. Mountain Wave Observations at ALO

The Andes Mountains have been identified as a "hot spot" for MW activity in the stratosphere during the winter months [e.g., *Alexander and Barnett*, 2007; *Eckermann and Preusse*, 1999; *Jiang et al.*, 2002; *Reisin and Scheer*, 2004; *Smith et al.*, 2009; *Torre et al.*, 2012, 2014; *Wit et al.*, 2017]. This is due to the prevailing strong winds that blow eastward from the Pacific Ocean and suddenly encounter the immense Andes Mountain Range, the longest mountain range in the world, with an average elevation of ~ 4000 m. The Andes are a productive source of MWs with an expected high potential for penetrating into the MLT region during the winter months. This chapter seeks to quantify the detection of and parameters of mesospheric MWs, and investigate prevailing wind conditions over the Andes during their manifestations.

6.2.1. MTM Data Set

This MW study is conducted from ALO, using six years of the MTM data from 2012 to 2017 and focusing on the winter months (May to August). High resolution (2 min) Keograms are used to search for MWs in the processed MTM data. As described in Section 2.7, a keogram is a time series plot that provides an overview for the entire night of observation in one summary "image" and is an excellent tool for identifying MWs.

The Andes Mountains are oriented essentially North to South $\pm 15^\circ$ with minor variations due to local terrain direction. In the search for MWs, only the East to West (E-W) keogram is necessary. This is because a quasi-stationary wave crest visible in a time series of images will remain in roughly the same location in the E-W slice of the images and will, therefore, appear as a horizontal structure in the E-W keogram.

For convenience, keograms are usually constructed from the central pixels of the image. In order to increase spatial coverage of the images, three keograms are made for any given night to aid the search for MWs. From each set of data comprising of 128×128 pixel images pixel #32, pixel #64, and pixel #96 (each two pixels wide) are selected to construct the three separate keograms. This analysis provides coverage over most of the image area. Figure 6.6 shows a keogram with a near-horizontal MW signature for the night of 2–3 June 2013. The keogram is 150 km wide and continuous measurements were made for over 8 h. The encircled MW event was first detected at dusk and lasted over 3 h from 2300 UT until 0200 UT. The bright arch to the right of the keogram is the residual signature of the Milky Way. In this study, 6 years of wintertime data (May–August) comprising of 24 months were inspected and 330 nights of good quality image data were studied using the keogram technique to identify potential MWs. The nightly keograms were individually inspected for the presence of MWs (even very faint signatures), producing over 60 candidate nights for

further processing.

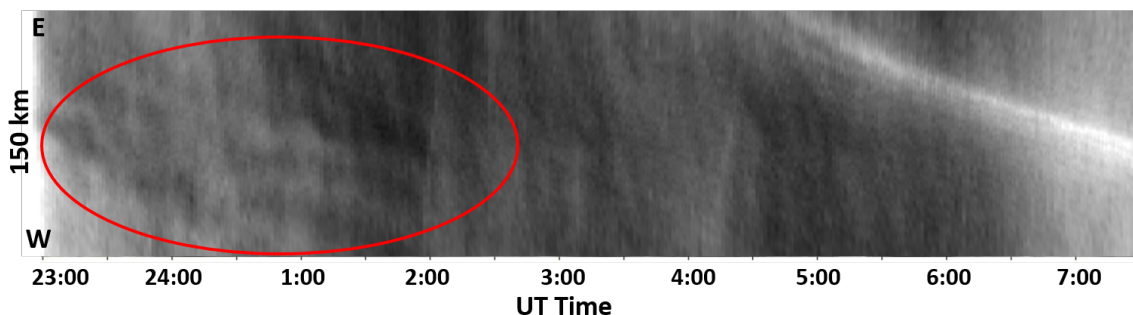


Figure 6.6. E-W keogram made from pixel 32 for the night of 2–3 June 2013 (UT day 154). The data last over 8 h and the highlighted MW event lasts about 3 h from 2300 UT until 0200 UT.

6.2.2. Survey of MW Parameters

In theory, MWs have phase velocities close to zero, but in reality the waves can fluctuate back and forth or drift slowly from their stationary position over time due to variations in the background wind. These data were carefully analyzed and cautiously interpreted because it is difficult to measure a wave with a close-to-zero phase speed, especially in the presence of other propagating waves. Many MW events are intermittent, and over the course of a single night the MWs can break or simply fade away. As such, these results may have minor differences when different people analyze the image data.

Examination of Figure 2.8 and its lowpass-filtered signature in Figure 2.9 also shows evidence of near-horizontal MW structure signatures during the night of 22–23 June 2012 (UT day 175). Figure 6.7 shows another E-W intensity keogram obtained on the night of 8–9 July 2012 (UT day 191) containing clear evidence of a MW structure during the first half of the night (2300–0200 UT). The slowly rotating Milky Way also shows up as an elongated bright curved structure towards the right

end of the image. This MW event was also observed to break and has recently been analyzed in detail [Hecht *et al.*, 2018].

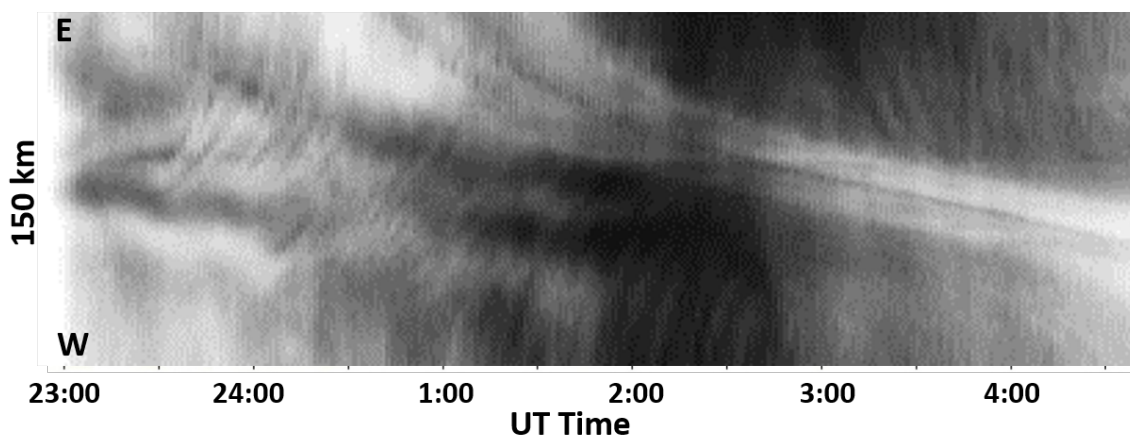


Figure 6.7. E-W keogram made from the middle pixels for the night of 8–9 July 2012.

An FFT analysis of the images of the 60 candidate nights produced 37 nights with MW signatures with phase velocities < 10 m/s. This study provides new insight into the occurrence and properties of MWs over ALO. Table 6.1 lists the results of the survey by year and UT day. MWs were observed from early May to mid August with most MW signatures detected during June. During each of the years 2012, 2013, and 2014 MW signatures were detected on 8 nights each, and 2017 had 7 nights with MW signatures. Due to limited data acquisition 2015 had only 2 nights, and 2016 had only 4 nights. [Guerrero, 2015] used all-sky imager data from ALO with a larger 180° FOV ($600 \text{ km} \times 600 \text{ km}$). He identified MW signatures on 95 nights out of a total of 544 nights from June to December during the years 2009–2013. During the years 2012 and 2013, the all-sky imager identified 8 nights and 14 nights, respectively, of MWs. The MTM similarly identified 8 nights in each year. The individual dates of the all-sky imager events are not identified [Guerrero, 2015].

Table 6.1. Parameters of Mountain Waves Observed at ALO and Notation of Coincidence Measurements From Other Instruments.

Year	UT Day	λ_H (km)	ϕ ($^\circ$)	Time (UT)	SCSN	MR	CIPS
2012	160	64	261	0204 – 0259	o	x	-
2012	174 [†]	36	234	2249 – 0136	x	x	-
2012	175 [†]	54	242	2249 – 0146	x	x	-
2012	176 [†]	42	264	2249 – 0047	x	o	-
2012	191 [†]	48	259	2254 – 0242	x	x	-
2012	192 [†]	35	275	2321 – 0143	x	x	-
2012	201	30	299	0645 – 0835	o	x	-
2012	205	49	279	2317 – 0143	x	x	-
2013	128	46	266	2258 – 0026	x	x	-
2013	134 [†]	49	253	2256 – 0320	-	x	-
2013	135 [†]	37	252	0226 – 0623	o	x	-
2013	151	27	251	2321 – 0214	x	x	-
2013	169	55	243	0435 – 0905	o	x	-
2013	209 [†]	56	265	0257 – 0441	o	x	-
2013	210 [†]	71	257	0134 – 0443	o	x	-
2013	217	51	251	0220 – 0601	o	x	-
2014	174	40	255	2249 – 0123	x	-	-
2014	177	65	252	0005 – 0410	o	-	-
2014	179	75	256	0001 – 0859	o	-	-
2014	181	55	243	2251 – 0635	x	-	-
2014	183 [†]	65	260	2251 – 0427	o	-	-
2014	184 [†]	14	262	0703 – 1025	o	-	-
2014	228	41	288	0130 – 0339	-	x	-
2014	231	47	272	0346 – 0512	-	x	-
2015	196	24	272	0549 – 0710	o	-	-
2015	200	32	253	0422 – 0849	o	-	-
2016	163 ^{†a}	24	281	0147 – 0456	o	x	x
2016	-	31	215	0748 – 1014			
2016	164 [†]	65	247	0302 – 0710	o	o	x
2016	180 [†]	42	250	2250 – 0102	x	-	x
2016	181 [†]	54	247	2316 – 0309	x	-	x
2017	137	60	276	2337 – 0056	x	-	-
2017	166	60	225	2247 – 0238	x	-	-
2017	169 [†]	41	305	2355 – 0217	x	-	-
2017	170 [†]	28	262	0223 – 0343	o	-	-
2017	171 [†]	44	270	2327 – 0053	x	-	-
2017	195	43	236	2259 – 0107	x	-	-
2017	228	28	258	0230 – 0438	o	-	-

Note: x – Coincident data. o – Data available, but not coincidence.

† – Consecutive nights of MW observations. ^a2 events on one night.

Using the MTM OH image data, the 37 MW events were further analyzed with software developed at USU and a two-dimensional FFT—as discussed in Section 2.8—to determine the observed horizontal wavelength (λ_H) the duration of the waves, and the azimuth (direction of propagation) of the waves (ϕ) measured in degrees clockwise from North. The results are plotted in Figure 6.8. The mean λ_H is 46 ± 3 km and range from 14 to 75 km (Figure 6.8a). *Guerrero* [2015] reported a similar λ_H range of 10–40 km. Most of the MWs occurred at the beginning of the night, around 2300 UT. The MWs were intermittent, lasting from ~ 30 min up to 9 h (Figure 6.8b) with a median of 2.7 ± 0.3 h, but with only nine events lasting more than 4 h. Note that the winter observations were limited by clouds or the ending of the observing period. Figure 6.8c shows the λ_H as a function of the ϕ . The distribution of the wave fronts as determined from the measured ϕ are well aligned with the orientation of the mountain range ($11^\circ\pm 3^\circ$ off of N-S with a range of ± 18) as shown in Figure 6.8d. Table 6.1 lists the measured wave parameters.

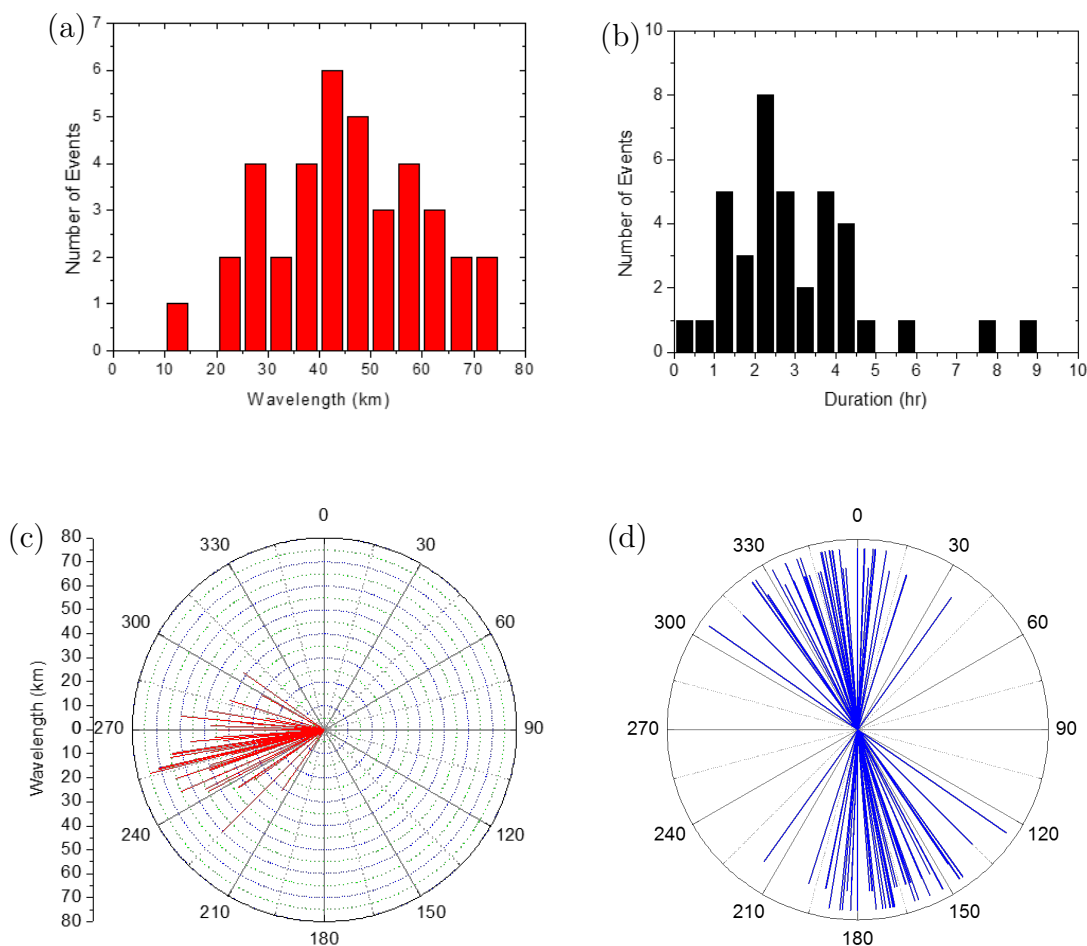


Figure 6.8. Observed parameters of MW events from ALO, 2012–2017. (a) Distribution of observed horizontal wavelength, the mean is 46 ± 3 km. (b) Duration of MW events, the median is 2.7 h. (c) Wavelength of MW events in their direction of propagation. North is 0° . (d) Orientation of wave fronts observed from ALO, 2012–2017 are closely aligned with the Andes Mountain Range ($\pm 18^\circ$).

6.2.3. Comparative Radiosonde Wind Data

Knowledge of the wind conditions in the lower atmosphere is important for investigating the prevailing conditions under which the MWs were able to propagate into the MLT region [Smith *et al.*, 2009]. Low altitude (0–30 km) wind measurements are available from radiosonde data from the SCSN Santo Domingo Sta-

tion (33.7°S , 71.6°W) located ~ 400 km to the South. The SCSN Station is part of the Upper Air Soundings Network, and data are provided by the University of Wyoming and available on the Department of Atmospheric Science website (<http://weather.uwyo.edu/upperair/sounding.html>). The radiosonde soundings, when available, are taken twice a day, at 00 UT and 12 UT. Radiosonde measurements are available on 34 out of the 37 nights, and on 17 of those nights a mesospheric MW signature is present during the 00 UT sounding (indicated by an "o" and "x" respectively, in Table 6.1 in the column labeled "SCSN").

An example night of radiosonde soundings demonstrate how the low altitude wind conditions influence the presence of MWs in the MLT region. On 29–30 June (UT day 181) 2014, the wind conditions were strong and consistently eastward, favorable for the creation and vertical propagation of MWs. Figure 6.9 shows the u profiles recorded by three radiosondes before (red), during (black), and after (blue) a MW was observed in the mesosphere. The associated MTM keogram shown in Figure 6.10 reveals a faint MW signature present at the beginning of the night (~ 2250 UT) and lasts until ~ 0630 UT.

Figure 6.11 summarizes the radiosonde soundings of the u profiles taken at 00 UT for the 17 of the 37 nights when observed mesospheric MW signatures coincide with the radiosonde soundings at 00 UT. Note that the mean zonal wind profile shown in red does not cross the zero-wind line. When the number of profiles are expanded to include all of the radiosonde soundings on nights with MW signatures for a total of 34 nights, the mean profile looks similar but several individual nights cross the zero-wind line. On these nights the MW signatures do not appear in the keograms until later in the night possibly providing time, up to several hours, for the winds to change and allow for the vertical propagation of MWs into the MLT region. Present in the individual SCSN radiosonde zonal wind profiles in Figure 6.11 is a weak positive

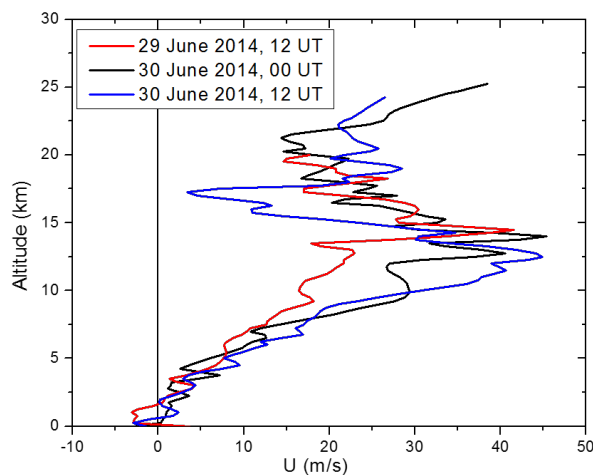


Figure 6.9. Zonal wind profiles recorded by three radiosondes before (red), during (black), and after (blue) MTM observed a MW events on the night of 29–30 June 2014.



Figure 6.10. E-W keogram for the night of 29–30 June 2014.

wind layer between the altitudes of ~ 15 – 25 km. While this weak wind layer doesn't cross the zero-wind line creating a MW critical layer, it does have a filtering effect on the MWs and their allowed phase speeds. This finding is in good agreement with *Kruse et al.* [2016], who reported on MWs propagating into the upper stratosphere over New Zealand that were limited by the presence of a similar layer they referred to as "valve layer" in the lower stratosphere.

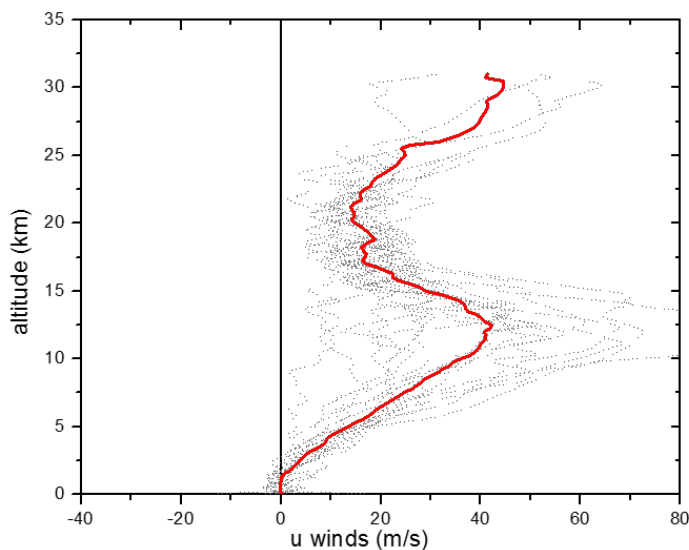


Figure 6.11. Radiosonde soundings of the zonal wind profiles, u , taken at 00 UT only for 17 of the 37 nights when MW signatures coincide with the radiosonde soundings at 00 UT. Note that the mean zonal wind profile show in red is eastward and does not cross the zero-wind line.

6.2.4. Coincident Meteor-Wind Radar Data

The meteor-wind radar (MR) at ALO provides wind measurements from 80–100 km. On 20 of the 37 nights with MW signatures the MR collected data (indicated by an "o" in Table 6.1 in the column labeled "MR"). On 18 of these nights there was coincident wind data (indicated by an "x" in Table 6.1 in the column labeled "MR"). Figure 6.12 shows the MR zonal winds, u , for several nights when MWs were present. MW signatures are present in the MTM keograms during the time indicated by the black vertical lines.

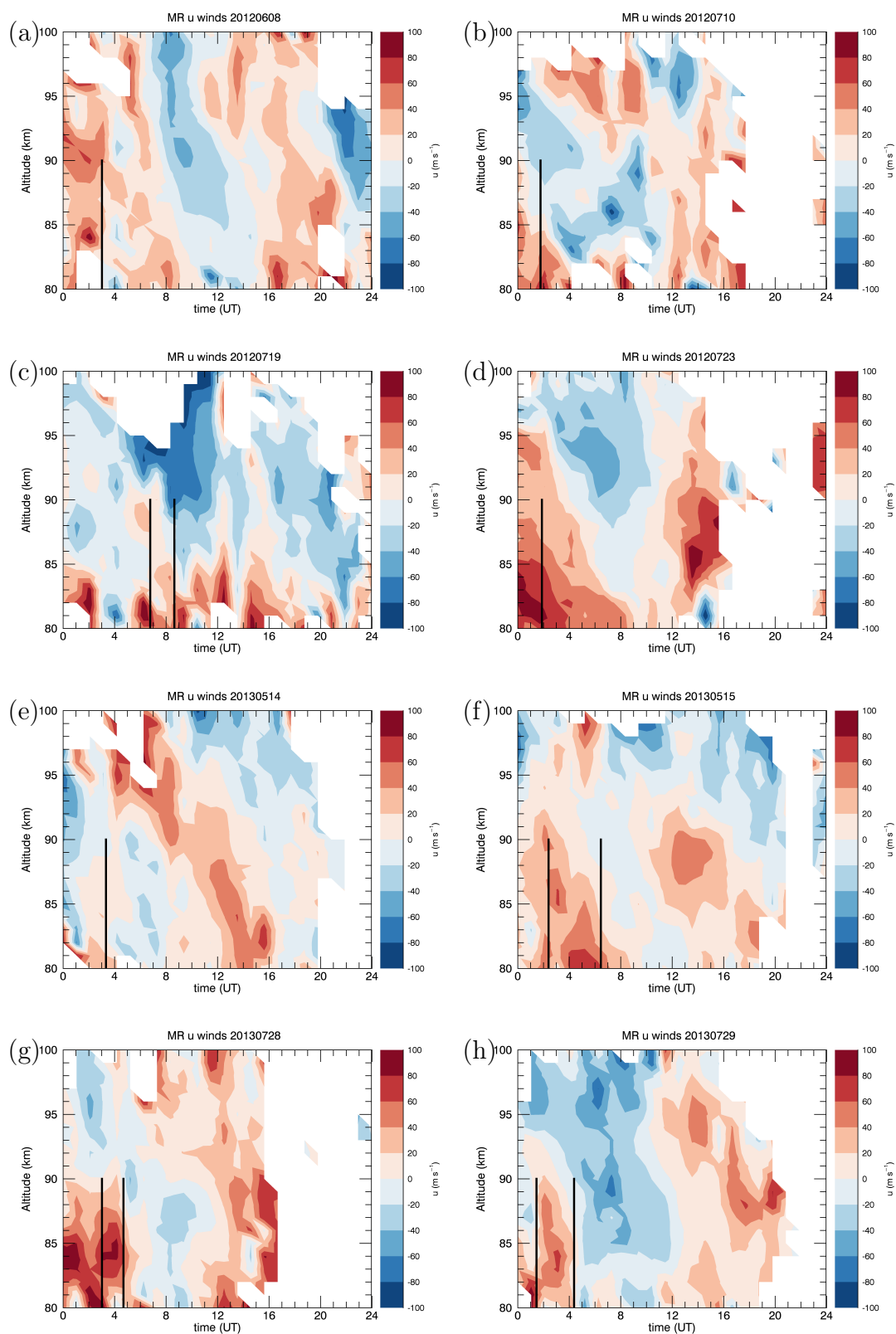


Figure 6.12. Example MR measurements showing different zonal wind conditions when MW were detected in the MLT region by the MTM. Bold lines indicate time interval when MWs were observed.

Of the 18 the nights with coincident MR data, nine nights exhibit strong positive winds, i.e., eastward (shades of red), allowing for the propagation of MWs into and within the MLT region throughout the duration of each MW event. For example, Figure 6.12a shows a MW signature is present at the beginning of the night of 8 June 2012 during strong eastward wind conditions until 0300 UT. At this time the MR zonal wind data reverses to westward (shades of blue). This creates a critical layer (zero-wind line) blocking the propagation of the MW into the MLT region in agreement with the observation that the MW ceased and is no longer detectable in the MTM data. Similar events can be seen in Figures 6.12c, 6.12f, 6.12g, and 6.12h. Another example night is 23 July 2012 (UT day 205), as shown in Figure 6.12d, where the MW is present at the beginning of the night, 2249 UT and lasts in the keogram almost 3 h until 0143 UT. However, the wind conditions in the MLT region continue to be favorable for several more hours (until \sim 04–08 UT), indicating that the penetration of the MW was quite probably limited at lower altitudes by critical-layer filtering.

The nine other nights exhibit situations as depicted in Figures 6.12b, 6.12c, and 6.12f, where both positive and negative wind conditions existed in the MLT region during the observation of the MW event. These nights were found to exhibit positive winds at lower altitudes and negative winds above. These nights are consistent with the airglow layer being a few km below its nominal altitude (\sim 87 km) on these occasions. For this comparison, no MTM data are available from 10–22 UT.

6.2.5. 18 June 2013 Case Study

Figure 6.13 shows the night of 18 June 2013 (UT day 169), when a MW was detected in the keogram, and both coincident radiosonde and MR data u winds were available. As shown in Figure 6.13a, the MW was detected at the start of the data set and lasts 4.5 h (0435–0905 UT). The measured λ_H was 55.2 km. Figure 6.13c

shows the radiosonde soundings the day before (red), 4 h before (black), and 3 hr after (blue) the MW was propagating, during which time the winds are all positive and exhibit the "valve layer" temperature profile between 17–25 km. The MR u wind shows positive winds up to ~ 85 km during the observation of the MW thus suggesting reduced height of the OH layer; wind reversals (zero-wind lines) encompass the MW event consistent with shades of blue on either side of the "observation window" in Figure 6.13b.

6.2.6. New MW Research Using MTM and AIM-CIPS Data

This section introduces new coordinated MTM MW observations over ALO with overpasses of the AIM satellite. The Cloud Imaging and Particle Size (CIPS) Instrument on board the AIM satellite was launched in April 2007, and measures ultraviolet Rayleigh-scattered light (265 nm) off of clouds with a primary mission of observing polar mesospheric clouds [Randall *et al.*, 2017]. It also provides GW detection from its recently developed Rayleigh Albedo Anomaly (RAA) data. CIPS is sensitive to GWs with λ_H between 15–600 km. On four nights with mesospheric MW signatures over ALO, observations of MWs in the upper stratosphere were obtained by CIPS (indicated by an "x" in Table 6.1 in the column labeled "CIPS").

For example, Figure 6.14a shows an E-W keogram for the night of 27–28 June 2016 as observed by the MTM. The observations start at 2335 UT and last until 0532 UT, approximately 7 h duration. The MTM MW signature was detected at the beginning of the observations and was observed for ~ 2 h. The measured λ_H was 42 km and was oriented 20° West of North. Figure 6.14b shows the horizontal strip of AIM's orbit over South America (North on the left). CIPS "scenes" are taken continually by four cameras every 3 min and "stitched" together creating a near-continuous large FOV (1000 km \times 2000 km). The observed radiance peaks near the ozone layer (50–55 km) and it has recently been shown that these data can be used to identify GW signatures

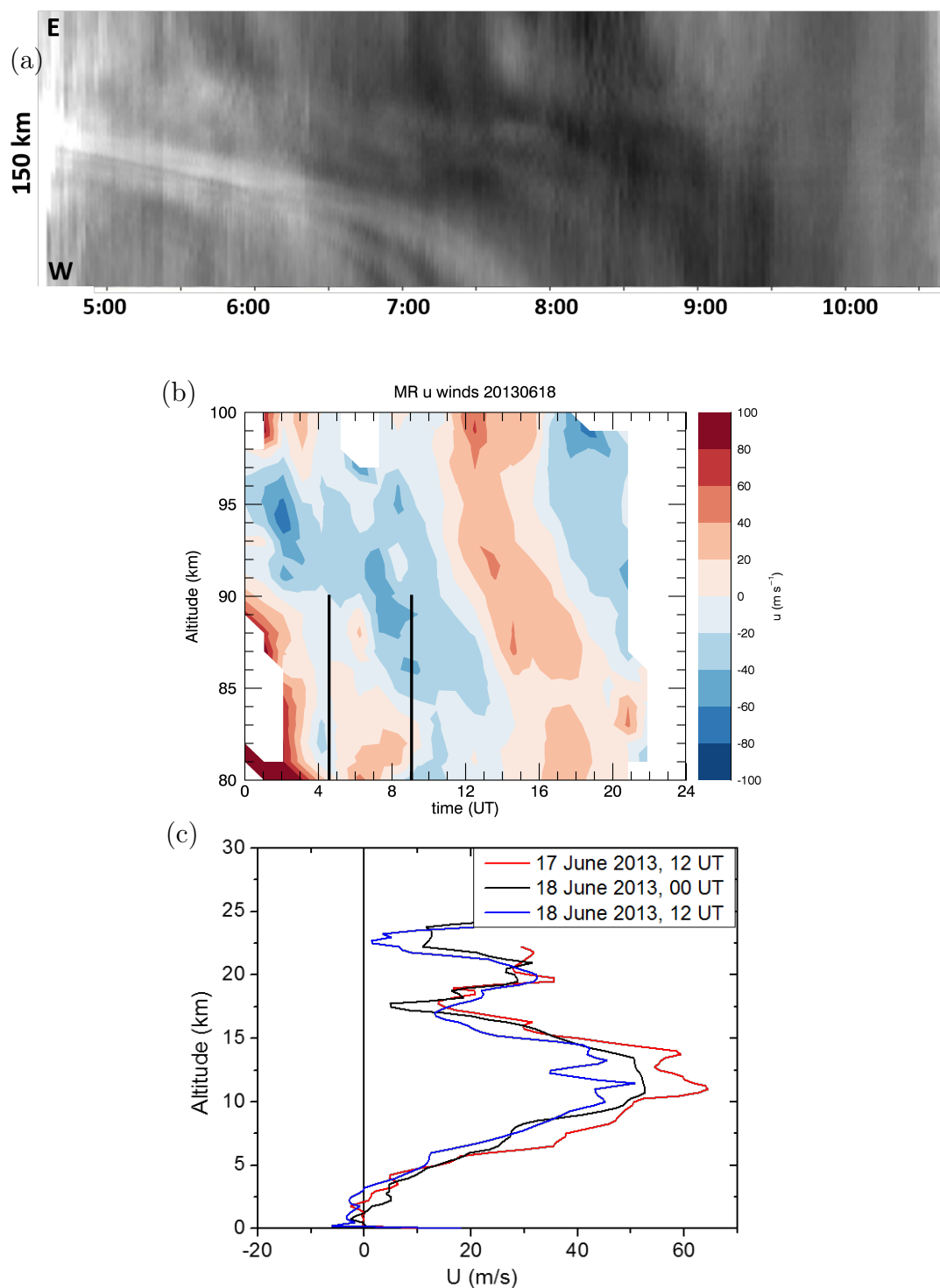


Figure 6.13. Plots showing MW signature in (a) the keogram, as well as coincident (b) MR u winds and (c) radiosonde u wind measurements for the night of 18 June (UT day 169) 2013. The MW lasted 4.5 h, from 0435–0905 UT.

in the upper stratosphere [Randall *et al.*, 2017]. Note the extensive presence of MW structures in the image over the Southern tip of South America extending up to the location of ALO (30°S) near the Chilean coastline. As more measurements become available, this could become a direction of future work in investigating the coupling by MWs in the stratosphere and mesosphere Taylor *et al.* [2016].

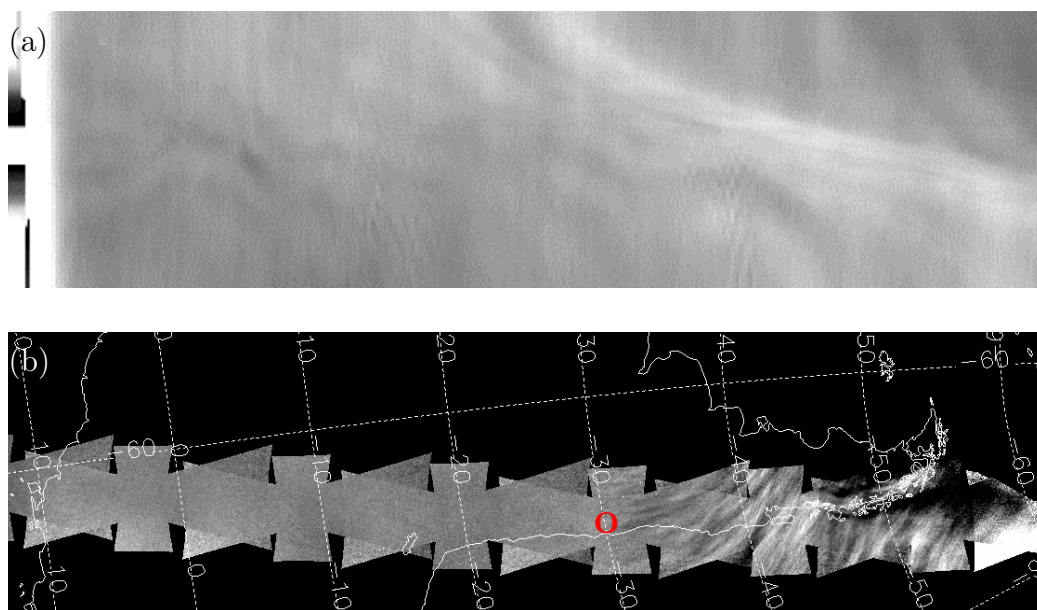


Figure 6.14. (a) E-W keogram and corresponding (b) CIPS images taken on the night of 27–28 June 2016. The CIPS images taken the same night showing large wave events over the Southern tip of South America extending north to ALO (indicated by red circle).

6.3. Summary and Conclusions

This chapter reports new observations of MWs occurring in the mesospheric OH airglow emission over the Andes. The primary goal is to catalogue, quantify, and analyze the MW signatures and their occurrence in relation to the background wind measurements. The measurements were made by the USU MTM imager during the winter periods 2012–2017. Keograms were used to visually identify the presence of

MWs. During the 6 years, 37 nights exhibited MW signatures representing $\sim 10\%$ of the nights. MWs were observed every year during the winter months (May–August). Their occurrence was relatively low compared to everyday freely propagating GWs. Using an all-sky OH imager also at ALO, [Guerrero, 2015] reported similar occurrence frequency for MWs during this period. To put these mesospheric results in context, *Alexander et al.* [2013] reported MW in the stratosphere on 37% of the possible winter nights during four winter season measurements over the high-latitude Antarctic Peninsula.

Individual wave parameters were analyzed for quasi-stationary MW events with orientations consistent with the mountain range. While some events lasted for several hours, most MWs were intermittent in nature with duration, lasting from ~ 30 min to a few hours, median 2.7 h. These results are in contrast to those reported by *Smith et al.* [2009] who measured a persistent MW event over three nights from El Leoncito with a mean λ_H of 36 ± 2 km. The 37 MTM MWs summarized in Table 6.1 exhibited a similar horizontal wavelength of 46 ± 3 km (ranging 15–75 km).

Using radiosonde soundings and MR, the atmospheric conditions preceding and during the occurrence of MWs were investigated. The radiosonde data shows strong eastward winds on all nights when MWs were observed. Similarly, the MR data show wind conditions during the intermittent period when MWs were observed to be favorable for MW propagation at MLT altitudes.

These results contribute to the understanding of how orographic forces affect the MLT in this "hot spot" of wave activity. MWs should be more prevalent further downwind on the leeward-side of the Andes Mountains and have been found to be more prevalent at higher-latitudes over the Southern tip of South America near the Drake Passage and extending to the Antarctic Peninsula due to the stronger vortex winds at stratospheric altitudes [*Alexander et al.*, 2015; *Sato et al.*, 2012; *Torre et al.*,

2014]. USU has recently located an AMTM at Tierra del Fuego, Argentina. New research on MWs is being focused over this region and should include the use of AIM-CIPS satellite imagery.

CHAPTER 7

SUMMARY AND FUTURE WORK

7.1. Summary

This dissertation presents a study of OH (6,2) band intensity and rotational temperature and small-scale GWs in the MLT region. The Utah State University (USU) Mesospheric Temperature Mapper (MTM) operated automatically from the Andes Lidar Observatory (ALO), Chile (30.3°S) for over eight years (2009–2017) acquiring over 1700 nights of high-quality data. Results include:

1. A large night-to-night variability was found at ALO in both temperature and intensity data, establishing a rich spectrum of GWs with strong tidal components. Two separate analysis methods were used to remove the effects of tides. Both methods revealed a main winter peak in GW variance with similar magnitudes. Further analysis determined the significant contribution (60%) of the short-period GWs (<1 h) to the total GW variance.
2. A seasonal investigation of the OH temperature data over the eight years determined a clear SAO signature, with an amplitude of 3.4 K (range 2–7 K), peaking in May and November. The AO component, which was usually smaller than the SAO with an average amplitude of 1.9 K (range 1–6 K), peaked in the winter (July). A systematic asymmetry was also found with the larger peak temperature occurring during the fall, likely due to a superposition of the AO and SAO signatures. An unexpected QAO (average amplitude, 2 K) was also identified at ALO [Zhao *et al.*, 2016] and reanalysis of the Maui MALT data determined a similar, but smaller QAO signature.

3. To investigate the effects of solar tides on the AO and SAO signatures, a harmonic local-time analysis was performed to remove diurnal and semidiurnal tidal contributions. With tides removed, the amplitude of the AO reduced significantly ($\sim 60\%$), while the amplitude of the SAO reduced only slightly ($\sim 10\%$). Following the findings of *Silber et al.* [2017], these new results suggest that at ALO, the semidiurnal tide has a greater influence on the combined AO and SAO seasonal variations.
4. Detailed analysis of coordinated MTM OH and SABER data reveal that MTM OH temperatures derived using the ratio method using transition probabilities given by *Pendleton Jr et al.* [2000] and *Goldman et al.* [1998] are in good agreement with the retrieved satellite measurements, both in their absolute values and their night-to-night variability. The selected $10^\circ \times 20^\circ$ sample volume provided a large coincident data set yielding a mean ΔT of 5.5 K. The MTM T_{OH} were found to be warmer than the SABER T_k measurements, in good agreement with several prior studies at other latitudes [e.g., *Oberheide et al.*, 2006; *Remsberg et al.*, 2008]. Comparison with earlier MTM and SABER studies at Maui have extended this investigation to over 15 years, establishing the MTM has maintained an accurate OH temperature measurement during this period with an average warm bias of ~ 5 K.
5. GW PE data obtained from SABER measurements depicts the seasonal structure evolving with increasing altitude from annual to semiannual with peaks in the summer and winter and minimums occurring in the spring and fall. GW PE show strong signs of wave breaking in both the stratosphere and mesosphere during the winter.

6. The solar sensitivity of the SABER T_k measured over ALO are in good agreement with other reported results [Beig, 2011; Forbes et al., 2014]. Longer data sets are needed to investigate the solar influence on the OH temperature. The MTM data set matches the solar cycle with a solar sensitivity of 12 K/100 sfu, but the effects of planetary waves have not yet been removed from this data. See Future Work below.
7. New observations of MWs occurring in the mesospheric OH airglow emission over the Andes resulted in the detection of 37 nights exhibited MW signatures during the six years representing $\sim 10\%$ of the clear winter nights. MWs were observed every year during the winter months (May–August). Most MWs were intermittent in nature with durations lasting from ~ 30 min to a few hours, median 2.7 h. Their horizontal wavelengths ranged from 15–75 km with a mean of 46 ± 3 km.
8. The radiosonde data shows strong eastward winds on all nights when MWs were observed. The MR data show wind conditions during the intermittent periods when MWs were observed to be favorable for MW propagation at MLT altitudes.
9. Although the winter atmospheric conditions over the Andes allow for the propagation of MWs into the mesosphere, the relatively low count of 37 MW nights over 6 consecutive winters is somewhat surprising. This suggests that the increase in GW variance over ALO (due in part to short-period GWs) as reported in Chapter 5 was probably not due to MWs alone.

The development of this dissertation has been shown at several conferences including the NSF sponsored Coupling, Energetics, and Dynamics of Atmospheric Regions (CEDAR) Workshop and the American Geophysical Union Fall Meeting [Pug-

mire, 2015; *Pugmire and Taylor*, 2013; *Pugmire et al.*, 2010, 2011, 2013, 2014; *Taylor et al.*, 2016, 2011; *Zhao et al.*, 2016].

7.2. Future Work

The extensive MTM measurements provide a trove of data available for future research endeavors. Possible directions for future work include the following:

1. As discussed in Section 6.2.6, as more measurements from CIPS RAA data become available, they could be used to investigate the coupling by MWs of the stratosphere and mesosphere [*Taylor et al.*, 2016].
2. As discussed in Section 4.3.2, an intriguing long-term trend in the MTM temperature data set was found (see Figure 4.10). There is an apparent visual correlation between the SABER T_k and the solar activity over this extended period. It is evident that the solar minimum of 2009 matches the low temperature measured by both SABER and the MTM, and the solar maximum in 2014 matches the temperature peak seen in both instruments. This trend matches the solar cycle with a solar sensitivity of 12 K/100 sfu. This solar sensitivity is currently two times larger than most other reported solar sensitivities, while the solar sensitivity of the SABER T_k are in good agreement with other reported results [*Beig*, 2011; *Forbes et al.*, 2014]. In order to investigate the correlation between the T_{OH} and T_k measurements and solar activity a longer data set needed.
3. The difference in temperatures obtained by SABER and the MTM over the observation period shows a recent decrease as shown in Figure 7.1. The most recent years (2016–2017) show the ΔT appears to have narrowed for both the MTM and El Leoncito spectrometer data. While more coincident measurements are needed for better understanding of the reasons, it does exhibit an inverse

relation to the long-term temperature trend measured by the MTM and the solar cycle.

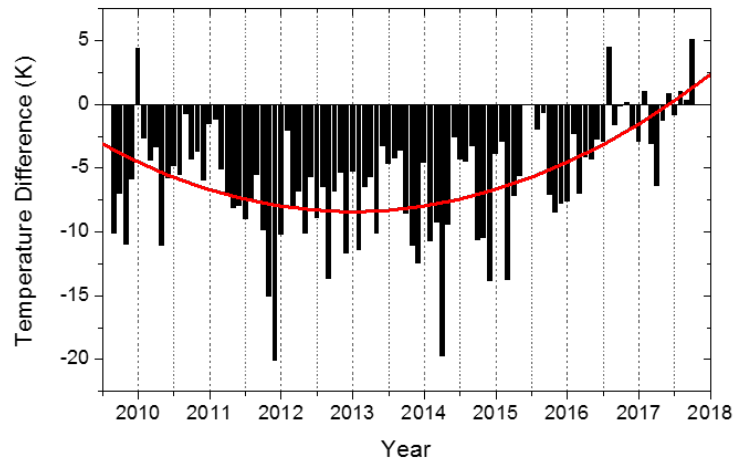


Figure 7.1. Monthly mean ΔT between the SABER T_k and the MTM T_{OH} for 2009–2017 at ALO.

4. Use SABER OH volume emission rates to determine the altitude of the OH layer to further investigate the seasonal difference of the 5 K temperature observed between the MTM and SABER and confirm the OH layer height during the observation of MWs while the MR winds exhibited zero-wind lines in the MLT region.
5. During the seasonal temperature analysis it was noted that strong quasi-two-day oscillations occurred almost every year during the summer months (January–February) [Hecht *et al.*, 2010; Moudden and Forbes, 2014]. The high quality of observation conditions at ALO have enabled long-duration (up to one month) of these events providing new information on the occurrence, temperature amplitudes, and variability. Future coordinated measurements with new improved MR data can be used to investigate their forcing, in particular the hypothesis

that they are subharmonic instabilities of the diurnal tide [Walterscheid *et al.*, 2015]. See Figure 7.2.

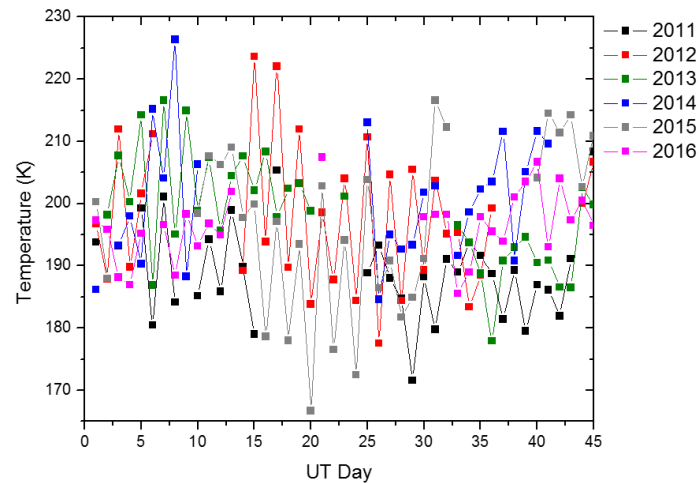


Figure 7.2. Nightly average temperature during each January and February from 2011 to 2016 showing two-day wave structure.

6. Further comparisons with on-site instruments and model data. So far the comparison has been used for calibration and focused on MWs. Comparisons with the Naval Research Laboratory's MSISE-00 model data show seasonal temperature differences.
7. Future analysis of small-scale GWs to find the wavelength, direction of propagation, phase speed and temperature perturbations of individual events, particularly using a newly developed statistical analysis method [Matsuda *et al.*, 2014; Talaei *et al.*, 2015]. Automation of keogram creation and wave parameter extraction would also speed up the GW and MW analyses.

REFERENCES

- Alexander, M. J., and C. Barnet (2007), Using satellite observations to constrain parameterizations of gravity wave effects for global models, *J. Atmos. Sci.*, *64*(5), 1652–1665.
- Alexander, M. J., and H. Teitelbaum (2007), Observation and analysis of a large amplitude mountain wave event over the Antarctic Peninsula, *J. Geophys. Res. Atmos. (1984–2012)*, *112*(D21).
- Alexander, M. J., S. D. Eckermann, D. Broutman, and J. Ma (2009), Momentum flux estimates for South Georgia Island mountain waves in the stratosphere observed via satellite, *Geophys. Res. Lett.*, *36*(12).
- Alexander, P., A. Torre, T. Schmidt, P. Llamedo, and R. Hierro (2015), Limb sounders tracking topographic gravity wave activity from the stratosphere to the ionosphere around midlatitude Andes, *J. Geophys. Res. Sp. Phys.*, *120*(10), 9014–9022.
- Alexander, S., A. Klekociuk, M. Pitts, A. McDonald, and A. Arevalo-Torres (2011), The effect of orographic gravity waves on Antarctic polar stratospheric cloud occurrence and composition, *J. Geophys. Res. Atmos. (1984–2012)*, *116*(D6).
- Alexander, S., A. Klekociuk, A. McDonald, and M. Pitts (2013), Quantifying the role of orographic gravity waves on polar stratospheric cloud occurrence in the Antarctic and the Arctic, *J. Geophys. Res. Atmos.*, *118*(20), 11–493.
- Andrews, D. G., J. R. Holton, and C. B. Leovy (1987), *Middle atmosphere dynamics*, 40, Academic press.

- Bacmeister, J. T. (1993), Mountain-wave drag in the stratosphere and mesosphere inferred from observed winds and a simple mountain-wave parameterization scheme, *J. Atmos. Sci.*, *50*(3), 377–399.
- Bacmeister, J. T., M. R. Schoeberl, L. R. Lait, P. A. Newman, and B. Gary (1990), ER-2 mountain wave encounter over Antarctica: Evidence for blocking, *Geophys. Res. Lett.*, *17*(1), 81–84.
- Bacmeister, J. T., P. A. Newman, B. L. Gary, and K. R. Chan (1994), An algorithm for forecasting mountain wave-related turbulence in the stratosphere, *Weather Forecast.*, *9*(2), 241–253.
- Baker, D. J., and A. Stair Jr (1988), Rocket measurements of the altitude distributions of the hydroxyl airglow, *Phys. Scripta*, *37*(4), 611.
- Banks, P., and G. Kockarts (2013), *Aeronomy*, Elsevier.
- Bates, D. R., and M. Nicolet (1950), Atmospheric hydrogen, *Publ. Astron. Soc. Pac.*, *62*(366), 106–110.
- Beig, G. (2011), Long-term trends in the temperature of the mesosphere/lower thermosphere region: 2. solar response, *J. Geophys. Res. Sp. Phys.*, *116*(A2).
- Bittner, M., D. Offermann, H.-H. Graef, M. Donner, and K. Hamilton (2002), An 18-year time series of OH rotational temperatures and middle atmosphere decadal variations, *J. Atmos. Sol. Terr. Phys.*, *64*(8), 1147–1166.
- Bossert, K., D. C. Fritts, P.-D. Pautet, M. J. Taylor, B. P. Williams, and W. R. Pendelton (2014), Investigation of a mesospheric gravity wave ducting event using coordinated sodium lidar and Mesospheric Temperature Mapper measurements at ALOMAR, norway (69 N), *J. Geophys. Res. Atmos.*, *119*(16), 9765–9778.

- Bossert, K., C. G. Kruse, C. J. Heale, D. C. Fritts, B. P. Williams, J. B. Snively, P.-D. Pautet, and M. J. Taylor (2017), Secondary gravity wave generation over New Zealand during the DEEPWAVE campaign, *J. Geophys. Res. Atmos.*
- Broadfoot, A. L., and K. R. Kendall (1968), The airglow spectrum, 3100–10,000 Å, *J. Geophys. Res.*, *73*(1), 426–428.
- Burns, G., T. Kawahara, W. French, A. Nomura, and A. Klekociuk (2003), A comparison of hydroxyl rotational temperatures from Davis (69 S, 78 E) with sodium lidar temperatures from Syowa (69 S, 39 E), *Geophys. Res. Lett.*, *30*(1).
- Cai, X., T. Yuan, Y. Zhao, P.-D. Pautet, M. J. Taylor, and W. Pendleton (2014), A coordinated investigation of the gravity wave breaking and the associated dynamical instability by a Na lidar and an Advanced Mesosphere Temperature Mapper over Logan, UT (41.7 N, 111.8 W), *J. Geophys. Res. Sp. Phys.*, *119*(8), 6852–6864.
- Cao, B., C. J. Heale, Y. Guo, A. Z. Liu, and J. B. Snively (2016), Observation and modeling of gravity wave propagation through reflection and critical layers above Andes Lidar Observatory at Cerro Pachón, Chile, *J. Geophys. Res. Atmos.*, *121*(21).
- Chamberlain, J. (1961), Physics of the aurora and airglow academic, *New York, 19612*, 34–61.
- Chapman, S. (1931), Bakerian Lecture. some phenomena of the upper atmosphere, *Proc.R. Soc. Lon. Ser.-A*, *132*(820), 353–374.
- Coble, M., G. C. Papen, and C. S. Gardner (1998), Computing two-dimensional unambiguous horizontal wavenumber spectra from OH airglow images, *IEEE T. Geosci. Remote*, *36*(2), 368–382.

- Dörnbrack, A., M. Leutbecher, R. Kivi, and E. Kyrö (1999), Mountain-wave-induced record low stratospheric temperatures above northern Scandinavia, *Tellus A*, *51*(5), 951–963.
- Eather, R., S. Mende, and R. Judge (1976), Plasma injection at synchronous orbit and spatial and temporal auroral morphology, *J. Geophys. Res.*, *81*(16), 2805–2824.
- Eather, R., S. Mende, and E. Weber (1979), Dayside aurora and relevance to substorm current systems and dayside merging, *J. Geophys. Res. Sp. Phys.*, *84*(A7), 3339–3359.
- Eckermann, S. D. (1995), On the observed morphology of gravity-wave and equatorial-wave variance in the stratosphere, *J. Atmos. Sol. Terr. Phys.*, *57*(2), 105–134.
- Eckermann, S. D., and P. Preusse (1999), Global measurements of stratospheric mountain waves from space, *Science*, *286*(5444), 1534–1537.
- Eckermann, S. D., J. Ma, and D. Broutman (2004), The NRL Mountain Wave Forecast Model (MWFM)[preprint], *Tech. rep.*, DTIC Document.
- Eckermann, S. D., D. Broutman, J. Ma, J. D. Doyle, P.-D. Pautet, M. J. Taylor, K. Bossert, B. P. Williams, D. C. Fritts, and R. B. Smith (2016), Dynamics of orographic gravity waves observed in the mesosphere over the Auckland Islands during the Deep Propagating Gravity Wave Experiment (DEEPWAVE), *J. Atmos. Sci.*, *73*(10), 3855–3876.
- Ern, M., P. Preusse, and C. Warner (2006), Some experimental constraints for spectral parameters used in the Warner and McIntyre gravity wave parameterization scheme, *Atmos. Chem. Phys.*, *6*(12), 4361–4381.

- Evers, L. G., and B. Dost (2010), Infrasound and seismology in the low frequency array LOFAR, *Triennial Scientific Report 2007-2009*.
- Forbes, J. M. (1982), Atmospheric tides: 1. model description and results for the solar diurnal component, *J. Geophys. Res. Sp. Phys. (1978–2012)*, *87*(A7), 5222–5240.
- Forbes, J. M., X. Zhang, and D. R. Marsh (2014), Solar cycle dependence of middle atmosphere temperatures, *J. Geophys. Res. Atmos.*, *119*(16), 9615–9625.
- French, W., and F. Mulligan (2010), Stability of temperatures from TIMED/SABER v1.07 (2002–2009) and Aura/MLS v2.2 (2004–2009) compared with OH (6-2) temperatures observed at Davis Station, Antarctica, *Atmos. Chem. Phys.*, *10*(23), 11,439–11,446.
- French, W., G. Burns, K. Finlayson, P. Greet, R. Lowe, and P. Williams (2000), Hydroxyl (6/2) airglow emission intensity ratios for rotational temperature determination, in *Ann. Geophys.*, vol. 18, pp. 1293–1303, Springer.
- Fritts, D. C., and M. J. Alexander (2003), Gravity wave dynamics and effects in the middle atmosphere, *Rev. Geophys.*, *41*(1).
- Fritts, D. C., and G. D. Nastrom (1992), Sources of mesoscale variability of gravity waves. part II: Frontal, convective, and jet stream excitation, *J. Atmos. Sci.*, *49*(2), 111–127.
- Fritts, D. C., K. Wan, J. Werne, T. Lund, and J. H. Hecht (2014a), Modeling the implications of Kelvin-Helmholtz instability dynamics for airglow observations, *J. Geophys. Res. Atmos.*, *119*(14), 8858–8871.
- Fritts, D. C., P. Pautet, K. Bossert, M. J. Taylor, B. P. Williams, H. Iimura, T. Yuan, N. J. Mitchell, G. Stober, et al. (2014b), Quantifying gravity wave momentum

- fluxes with mesosphere temperature mappers and correlative instrumentation, *J. Geophys. Res. Atmos.*, *119*(24).
- Fritts, D. C., R. B. Smith, M. J. Taylor, J. D. Doyle, S. D. Eckermann, A. Dörnbrack, M. Rapp, B. P. Williams, P.-D. Pautet, K. Bossert, et al. (2016), The Deep Propagating Gravity Wave Experiment (DEEPWAVE): An airborne and ground-based exploration of gravity wave propagation and effects from their sources throughout the lower and middle atmosphere, *B. Am. Meteorol. Soc.*, *97*(3), 425–453.
- Garcia, F., M. J. Taylor, and M. Kelley (1997), Two-dimensional spectral analysis of mesospheric airglow image data, *Applied optics*, *36*(29), 7374–7385.
- Garcia, R. R., and S. Solomon (1985), The effect of breaking gravity waves on the dynamics and chemical composition of the mesosphere and lower thermosphere, *J. Geophys. Res. Atmos.*, *90*(D2), 3850–3868.
- García-Comas, M., B. Funke, M. López-Puertas, D. Bermejo-Pantaleón, N. Glatthor, T. v. Clarmann, G. Stiller, U. Grabowski, C. Boone, W. French, et al. (2012), On the quality of MIPAS kinetic temperature in the middle atmosphere, *Atmos. Chem. Phys.*, *12*(13), 6009–6039.
- García-Comas, M., B. Funke, A. Gardini, M. López-Puertas, A. Jurado-Navarro, T. v. Clarmann, G. Stiller, M. Kiefer, C. Boone, T. Leblanc, et al. (2014), MIPAS temperature from the stratosphere to the lower thermosphere: Comparison of vM21 with ACE-FTS, MLS, OSIRIS, SABER, SOFIE and lidar measurements, *Atmos. Meas. Techn.*, *7*(11), 3633–3651.
- Gardner, C., T. Kane, J. Hecht, R. Walterscheid, J. Yee, R. Niciejewski, R. Lowe, and D. Turnbull (1991), Formation characteristics of sporadic na layers observed

- simultaneously by lidar and airglow instruments during ALOHA-90, *Geophys. Res. Lett.*, 18(7), 1369–1372.
- Gardner, C. S., and M. J. Taylor (1998), Observational limits for lidar, radar, and airglow imager measurements of gravity wave parameters, *J. Geophys. Res. Atmos.* (1984–2012), 103(D6), 6427–6437.
- Gavrilov, N., S. Fukao, T. Nakamura, T. Tsuda, M. Yamanaka, and M. Yamamoto (1996), Statistical analysis of gravity waves observed with the middle and upper atmosphere radar in the middle atmosphere: 1. method and general characteristics, *J. Geophys. Res. Atmos.*, 101(D23), 29,511–29,521.
- Gelinas, L., J. H. Hecht, R. Walterscheid, R. G. Roble, and J. M. Woithe (2008), A seasonal study of mesospheric temperatures and emission intensities at Adelaide and Alice Springs, *J. Geophys. Res. Sp. Phys.*, 113(A1).
- Gille, J. C., and J. M. Russell (1984), The limb infrared monitor of the stratosphere: Experiment description, performance, and results, *J. Geophys. Res. Atmos.* (1984–2012), 89(D4), 5125–5140.
- Goldman, A., W. Schoenfeld, D. Goorvitch, C. Chackerian Jr, H. Dothe, F. Mélen, M. Abrams, and J. Selby (1998), Updated line parameters for OH X2II–X2II ($\nu\hat{a}^{2'}$, $\nu\hat{a}^2$) transitions, *Journal of Quantitative Spectroscopy and Radiative Transfer*, 59(3–5), 453 – 469.
- Gossard, E. E., and W. H. Hooke (1975), Waves in the atmosphere: atmospheric infrasound and gravity waves-their generation and propagation, *Atmospheric Science*, 2.

- Greet, P., W. French, G. Burns, P. Williams, R. Lowe, and K. Finlayson (1997), OH (6–2) spectra and rotational temperature measurements at Davis, Antarctica, in *Ann. Geophys.*, vol. 16, pp. 77–89, Springer.
- Grimsdell, A. W., and M. J. Alexander (2016), Stratospheric gravity waves at Southern Hemisphere orographic hotspots: 2003–2014 AIRS/Aqua observations, *Atmos. Chem. Phys.*, 16(14), 9381.
- Guerrero, J. A. (2015), Investigation of mountain waves in the mesosphere over the Andes Mountains, Ph.D. thesis, Embry-Riddle Aeronautical University.
- Hapgood, M., and M. J. Taylor (1982), Analysis of airglow image data, in *Annales de Geophysique*, vol. 38, pp. 805–813.
- Heale, C., K. Bossert, J. Snively, D. Fritts, P.-D. Pautet, and M. J. Taylor (2017), Numerical modeling of a multiscale gravity wave event and its airglow signatures over Mount Cook, New Zealand, during the DEEPWAVE campaign, *J. Geophys. Res. Atmos.*, 122(2), 846–860.
- Hecht, J., A. Z. Liu, R. Walterscheid, and R. Rudy (2005), Maui mesosphere and lower thermosphere (Maui malt) observations of the evolution of kelvin-helmholtz billows formed near 86 km altitude, *J. Geophys. Res. Atmos.*, 110(D9).
- Hecht, J., R. Walterscheid, L. Gelinias, R. Vincent, I. Reid, and J. Woithe (2010), Observations of the phase-locked 2 day wave over the Australian sector using medium-frequency radar and airglow data, *J. Geophys. Res. Atmos.*, 115(D16).
- Hecht, J., K. Wan, L. Gelinias, D. C. Fritts, R. Walterscheid, R. Rudy, A. Liu, S. J. Franke, F. Vargas, P.-D. Pautet, et al. (2014), The life cycle of instability features measured from the Andes Lidar Observatory over Cerro Pachon on 24 march 2012, *J. Geophys. Res. Atmos.*, 119(14), 8872–8898.

- Hecht, J., D. Fritts, L. Wang, L. Gelinas, R. Rudy, R. Walterscheid, M. Taylor, P. Pautet, S. Smith, and S. Franke (2018), Observations of the breakdown of mountain waves over the Andes Lidar Observatory at Cerro Pachon on 8/9 July 2012, *J. Geophys. Res. Atmos.*, *123*(1), 276–299.
- Hecht, J. H., and R. L. Walterscheid (1991), Observations of the OH meinel (6, 2) and O₂ atmospheric (0, 1) nightglow emissions from Maui during the aloha-90 campaign, *Geophys. Res. Lett.*, *18*(7), 1341–1344.
- Herzberg, G. (1951), The atmospheres of the planets (with plates iii and iv), *Journal of the Royal Astronomical Society of Canada*, *45*, 100.
- Hickey, M. P., M. Taylor, C. S. Gardner, C. R. Gibbons, et al. (1998), Full-wave modeling of small-scale gravity waves using airborne lidar and observations of the Hawaiian airglow (ALOHA-93) O (1 S) images and coincident na wind/temperature lidar measurements, *J. Geophys. Res. Atmos.*, *103*(D6), 6439–6453.
- Hines, C. (1960), Internal atmospheric gravity waves at ionospheric heights, *Can. J. Phys.*, *38*(11), 1441–1481.
- Hines, C. O. (1989), Earlier days of gravity waves revisited, *Pure Appl. Geophys.*, *130*(2-3), 151–170.
- Holton, J. R., and M. J. Alexander (1999), Gravity waves in the mesosphere generated by tropospheric convection, *Tellus B*, *51*(1), 45–58.
- Huang, F. T., H. G. Mayr, C. A. Reber, J. M. Russell, M. G. Mlynczak, and J. G. Mengel (2008), Ozone quasi-biennial oscillations (QBO), semiannual oscillations (SAO), and correlations with temperature in the mesosphere, lower thermosphere, and stratosphere, based on measurements from SABER on TIMED and MLS on UARS, *J. Geophys. Res. Sp. Phys.*, *113*(A1).

- Jiang, J. H., D. L. Wu, and S. D. Eckermann (2002), Upper atmosphere research satellite (UARS) MLS observation of mountain waves over the Andes, *J. Geophys. Res. Atmos. (1984–2012)*, *107*(D20), SOL–15.
- Jiang, J. H., S. D. Eckermann, D. L. Wu, and J. Ma (2004), A search for mountain waves in MLS stratospheric limb radiances from the winter northern hemisphere: Data analysis and global mountain wave modeling, *J. Geophys. Res. Atmos. (1984–2012)*, *109*(D3).
- John, S. R., and K. K. Kumar (2012), TIMED/SABER observations of global gravity wave climatology and their interannual variability from stratosphere to mesosphere lower thermosphere, *Climate dynamics*, *39*(6), 1489–1505.
- Kam, H., G. Jee, Y. Kim, Y.-b. Ham, and I.-S. Song (2017), Statistical analysis of mesospheric gravity waves over King Sejong Station, Antarctica (62.2° S, 58.8° W), *J. Atmos. Sol. Terr. Phys.*, *155*, 86–94.
- Kane, T. J., C. A. Hostetler, and C. S. Gardner (1991), Horizontal and vertical structure of the major sporadic sodium layer events observed during ALOHA-90, *Geophys. Res. Lett.*, *18*(7), 1365–1368.
- Krassovsky, V. (1972), Infrasonic variations of OH emission in the upper atmosphere, *Ann. Geophys.*, *28*, 739.
- Kruse, C. G., R. B. Smith, and S. D. Eckermann (2016), The midlatitude lower-stratospheric mountain wave "valve layer", *J. Atmos. Sci.*, *73*(12), 5081–5100.
- Larsen, M., A. Z. Liu, C. Gardner, M. Kelley, S. Collins, J. Friedman, and J. Hecht (2004), Observations of overturning in the upper mesosphere and lower thermosphere, *J. Geophys. Res. Atmos.*, *109*(D2).

- Li, F., A. Z. Liu, and G. R. Swenson (2005), Characteristics of instabilities in the mesopause region over Maui, Hawaii, *J. Geophys. Res. Atmos.*, *110*(D9).
- Liu, A. Z., and C. S. Gardner (2005), Vertical heat and constituent transport in the mesopause region by dissipating gravity waves at Maui, Hawaii (20.7 N), and Starfire Optical Range, New Mexico (35 N), *J. Geophys. Res. Atmos.*, *110*(D9).
- Liu, A. Z., Y. Guo, F. Vargas, and G. R. Swenson (2016), First measurement of horizontal wind and temperature in the lower thermosphere (105–140 km) with a Na lidar at Andes Lidar Observatory, *Geophys. Res. Lett.*, *43*(6), 2374–2380.
- Liu, W., J. Xu, A. K. Smith, and W. Yuan (2015), Comparison of rotational temperature derived from ground-based OH airglow observations with TIMED/SABER to evaluate the Einstein coefficients, *J. Geophys. Res. Sp. Phys.*, *120*(11), 10,069–10,082.
- Liu, X., J. Yue, J. Xu, L. Wang, W. Yuan, J. M. Russell, and M. E. Hervig (2014), Gravity wave variations in the polar stratosphere and mesosphere from SOFIE/AIM temperature observations, *J. Geophys. Res. Atmos.*, *119*(12), 7368–7381.
- Lomb, N. R. (1976), Least-squares frequency analysis of unequally spaced data, *Astrophys. Space Sci.*, *39*(2), 447–462.
- López-González, M., M. García-Comas, E. Rodríguez, M. López-Puertas, M. Shepherd, G. Shepherd, S. Sargoytchev, V. Aushev, S. Smith, M. Mlynczak, et al. (2007), Ground-based mesospheric temperatures at mid-latitude derived from O₂ and OH airglow SATI data: Comparison with SABER measurements, *J. Atmos. Sol. Terr. Phys.*, *69*(17), 2379–2390.

- Lowe, R., and D. Turnbull (1995), Comparison of ALOHA-93, ANLC-93 and ALOHA-90 observations of the hydroxyl rotational temperature and gravity wave activity, *Geophys. Res. Lett.*, *22*(20), 2813–2816.
- Lu, D., T. VanZandt, and W. Clark (1984), VHF doppler radar observations of buoyancy waves associated with thunderstorms, *J. Atmos. Sci.*, *41*(2), 272–282.
- Matsuda, T. S., T. Nakamura, M. K. Ejiri, M. Tsutsumi, and K. Shiokawa (2014), New statistical analysis of the horizontal phase velocity distribution of gravity waves observed by airglow imaging, *Journal of Geophysical Research: Atmospheres*, *119*(16), 9707–9718.
- McIntyre, M. E., J. Holton, J. Pyle, and J. Curry (2003), Encyclopedia of atmospheric sciences, *Academic, London*, pp. 323–330.
- Meinel, I. (1950), OH emission bands in the spectrum of the night sky., *The Astrophysical Journal*, *111*, 555.
- Meriwether, J. W. (1975), High latitude airglow observations of correlated short-term fluctuations in the hydroxyl Meinel 8-3 band intensity and rotational temperature, *Planet. Space Sci.*, *23*(8), 1211–1221.
- Meriwether Jr, J. (1984), Ground based measurements of mesosphere temperature by optical means, *MAP*, *13*, 1–18.
- Mlynczak, M. G. (1997), Energetics of the mesosphere and lower thermosphere and the SABER experiment, *Advances in Space Research*, *20*(6), 1177–1183.
- Mlynczak, M. G., and S. Solomon (1993), A detailed evaluation of the heating efficiency in the middle atmosphere, *J. Geophys. Res. Atmos.*, *98*(D6), 10,517–10,541.

- Moudden, Y., and J. Forbes (2014), Quasi-two-day wave structure, interannual variability, and tidal interactions during the 2002–2011 decade, *J. Geophys. Res. Atmos.*, *119*(5), 2241–2260.
- Mulligan, F., and R. Lowe (2008), OH-equivalent temperatures derived from ACE-FTS and SABER temperature profiles—a comparison with OH*(3-1) temperatures from Maynooth (53.2°N, 6.4°W), *Ann. Geophys. (ANGEO)*, *26*(4), 795–811.
- Mzé, N., A. Hauchecorne, P. Keckhut, and M. Thétis (2014), Vertical distribution of gravity wave potential energy from long-term Rayleigh lidar data at a northern middle-latitude site, *J. Geophys. Res. Atmos.*, *119*(21).
- Nappo, C. (2002), *An Introduction to Atmospheric Gravity Waves*, no. v. 1 in *An Introduction to Atmospheric Gravity Waves*, Academic Press.
- Nastrom, G. D., and D. C. Fritts (1992), Sources of mesoscale variability of gravity waves. part I: Topographic excitation, *J. Atmos. Sci.*, *49*(2), 101–110.
- NOAA (2018), Space weather prediction center: F10.7 cm radio emissions, <https://www.swpc.noaa.gov/phenomena/f107-cm-radio-emissions>, accessed: 2018-06-01.
- Noll, S., W. Kausch, S. Kimeswenger, S. Unterguggenberger, and A. M. Jones (2016), Comparison of VLT/X-shooter OH and O₂ rotational temperatures with consideration of TIMED/SABER emission and temperature profiles, *Atmos. Chem. Phys.*, *16*(8), 5021–5042.
- Oberheide, J., D. Offermann, J. Russell, and M. Mlynczak (2006), Intercomparison of kinetic temperature from 15 μm CO₂ limb emissions and OH*(3, 1) rotational temperature in nearly coincident air masses: SABER, GRIPS, *Geophys. Res. Lett.*, *33*(14).

- Offermann, D., and R. Gerndt (1990), Upper mesosphere temperatures from OHâ-emissions, *Advances in Space Research*, 10(12), 217–221.
- Offermann, D., O. Gusev, M. Donner, J. Forbes, M. Hagan, M. Mlynczak, J. Oberheide, P. Preusse, H. Schmidt, and J. Russell (2009), Relative intensities of middle atmosphere waves, *J. Geophys. Res. Atmos.*, 114(D6).
- Parihar, N., D. Singh, and S. Gurubaran (2017), A comparison of ground-based hydroxyl airglow temperatures with SABER/TIMED measurements over 23° N, India, in *Ann. Geophys.*, vol. 35, p. 353, Copernicus GmbH.
- Pautet, P.-D., M. Taylor, W. Pendleton, Y. Zhao, T. Yuan, R. Esplin, and D. McLain (2014), Advanced mesospheric temperature mapper for high-latitude airglow studies, *Appl. optics*, 53(26), 5934–5943.
- Pautet, P.-D., M. J. Taylor, D. Fritts, K. Bossert, B. Williams, D. Broutman, J. Ma, S. Eckermann, and J. Doyle (2016), Large-amplitude mesospheric response to an orographic wave generated over the Southern Ocean Auckland Islands (50.7° S) during the DEEPWAVE project, *J. Geophys. Res. Atmos.*, 121(4), 1431–1441.
- Pautet, P.-D., M. Taylor, J. Snively, and C. Solorio (2018), Unexpected occurrence of mesospheric frontal gravity wave events over South Pole (90° S), *J. Geophys. Res. Atmos.*, 123(1), 160–173.
- Pendleton Jr, W., and M. J. Taylor (2002), The impact of L-uncoupling on Einstein coefficients for the OH Meinel (6, 2) band: implications for Q-branch rotational temperatures, *J. Atmos. Sol. Terr. Phys.*, 64(8-11), 971–983.
- Pendleton Jr, W., M. J. Taylor, and L. Gardner (2000), Terdiurnal oscillations in OH Meinel rotational temperatures for fall conditions at northern mid-latitude sites, *Geophys. Res. Lett.*, 27(12), 1799–1802.

- Press, W. H. (2007), *Numerical recipes 3rd edition: The art of scientific computing*, Cambridge university press.
- Press, W. H., and G. B. Rybicki (1989), Fast algorithm for spectral analysis of unevenly sampled data, *The Astrophysical Journal*, *338*, 277–280.
- Preusse, P., B. Schaeler, J. Bacmeister, and D. Offermann (1999), Evidence for gravity waves in CRISTA temperatures, *Advances in Space Research*, *24*(11), 1601–1604.
- Preusse, P., A. Dörnbrack, S. D. Eckermann, M. Riese, B. Schaeler, J. T. Bacmeister, D. Broutman, and K. U. Grossmann (2002), Space-based measurements of stratospheric mountain waves by CRISTA 1. sensitivity, analysis method, and a case study, *Journal of Geophysical Research: Atmospheres*, *107*(D23).
- Pugmire, J. (2015), Satellite measurements of mesospheric gravity wave temperature variances over the Andes, in *CEDAR Conference Abstracts*.
- Pugmire, J., and M. J. Taylor (2013), Investigating mesospheric gravity wave dynamics and temperature variability over the Andes, in *Utah Space Grant Consortium Fellowship Symposium*.
- Pugmire, J., N. R. Criddle, M. J. Taylor, D. Pautet, and Y. Zhao (2010), First year investigation of gravity waves and temperature variability over the Andes, in *PASI School and Workshop on the Dynamics and Chemistry of the Upper Atmosphere*.
- Pugmire, J., Y. Zhao, M. J. Taylor, and P. D. Pautet (2011), Mesospheric temperature variability and seasonal characteristics over the Andes, in *CEDAR Conference Abstracts*.

- Pugmire, J., M. J. Taylor, Y. Zhao, P. Paudet, and J. M. Russell (2013), Observations of mesospheric temperature variability over the Andes, in *CEDAR Conference Abstracts*.
- Pugmire, J., M. J. Taylor, Y. Zhao, D. Pautet, and J. Russell (2014), TIMED/SABER satellite investigations of mesospheric gravity wave variances over the Andes, in *AGU Fall Meeting Abstracts*.
- Qian, L., A. Burns, and J. Yue (2017), Evidence of the lower thermospheric winter-to-summer circulation from SABER CO₂ observations, *Geophys. Res. Lett.*
- Randall, C., J. Carstens, J. France, V. Harvey, L. Hoffmann, S. Bailey, M. Alexander, J. Lumpe, J. Yue, B. Thuraiajah, et al. (2017), New AIM/CIPS global observations of gravity waves near 50-55 km, *Geophys. Res. Lett.*
- Reed, R. J., et al. (1962), Some features of the annual temperature regime in the tropical stratosphere, *Mon. Weather Rev.*, *90*(6), 211–215.
- Reid, I. (1986), Gravity wave motions in the upper middle atmosphere (60–110 km), *J. Atmos. Sol. Terr. Phys.*, *48*(11-12), 1057–1072.
- Reid, I. M., A. J. Spargo, J. M. Woithe, A. R. Klekociuk, J. P. Younger, and G. G. Sivjee (2017), Seasonal MLT-region nightglow intensities, temperatures, and emission heights at a southern hemisphere midlatitude site, *35*(3), 567.
- Reisin, E. R., and J. Scheer (2004), Gravity wave activity in the mesopause region from airglow measurements at El Leoncito, *J. Atmos. Sol. Terr. Phys.*, *66*(6), 655–661.
- Reisin, E. R., and J. Scheer (2017), Unexpected East-West effect in mesopause region SABER temperatures over El Leoncito, *J. Atmos. Sol. Terr. Phys.*, *157*, 35–41.

- Remsberg, E., B. Marshall, M. Garcia-Comas, D. Krueger, G. Lingenfelter, J. Martin-Torres, M. Mlynczak, J. Russell, A. Smith, Y. Zhao, et al. (2008), Assessment of the quality of the version 1.07 temperature-versus-pressure profiles of the middle atmosphere from TIMED/SABER, *J. Geophys. Res. Atmos. (1984–2012)*, *113*(D17).
- Richter, J. H., F. Sassi, and R. R. Garcia (2010), Toward a physically based gravity wave source parameterization in a general circulation model, *J. Atmos. Sci.*, *67*(1), 136–156.
- Roble, R., and E. Ridley (1994), A thermosphere-ionosphere-mesosphere-electrodynamics general circulation model (TIME-GCM): Equinox solar cycle minimum simulations (30–500 km), *Geophys. Res. Lett.*, *21*(6), 417–420.
- Russell III, J. M., M. G. Mlynczak, L. L. Gordley, J. J. Tansock Jr, and R. W. Esplin (1999), Overview of the SABER experiment and preliminary calibration results, in *SPIE's International Symposium on Optical Science, Engineering, and Instrumentation*, pp. 277–288, International Society for Optics and Photonics.
- Sato, K., S. Tatenno, S. Watanabe, and Y. Kawatani (2012), Gravity wave characteristics in the Southern Hemisphere revealed by a high-resolution middle-atmosphere general circulation model, *J. Atmos. Sci.*, *69*(4), 1378–1396.
- Scargle, J. D. (1982), Studies in astronomical time series analysis. ii-statistical aspects of spectral analysis of unevenly spaced data, *The Astrophysical Journal*, *263*, 835–853.
- Scheer, J., and E. R. Reisin (1990), Rotational temperatures for OH and O₂ airglow bands measured simultaneously from El Leoncito (31° 48â2S), *J. Atmos. Sol. Terr. Phys.*, *52*(1), 47 – 57.

- Scheer, J., E. Reisin, O. Gusev, W. French, G. Hernandez, R. Huppi, P. Ammosov, G. Gavrilieva, and D. Offermann (2006), Use of CRISTA mesopause region temperatures for the intercalibration of ground-based instruments, *J. Atmos. Sol. Terr. Phys.*, *68*(15), 1698–1708.
- Schmidlin, F. (1992), First observation of mesopause temperatures lower than 100 k, *Geophys. Res. Lett.*, *19*(16), 1643–1646.
- Schunk, R., and A. Nagy (2004), *Ionospheres: Physics, Plasma Physics, and Chemistry*, Cambridge atmospheric and space science series, Cambridge University Press.
- Semenov, A., N. Shefov, and I. Medvedeva (2013), Longitudinal variations in the hydroxyl emission: 1. temperature, *Geomagnetism and Aeronomy*, *53*(4), 492–501.
- Seyler, C. (2005), Internal waves and undular bores in mesospheric inversion layers, *J. Geophys. Res. Atmos.*, *110*(D9).
- She, C., and R. Lowe (1998), Seasonal temperature variations in the mesopause region at mid-latitude: comparison of lidar and hydroxyl rotational temperatures using WINDII/UARS OH height profiles, *J. Atmos. Sol. Terr. Phys.*, *60*(16), 1573–1583.
- Sheese, P., E. Llewellyn, R. Gattinger, A. Bourassa, D. Degenstein, N. Lloyd, and I. McDade (2011), Mesopause temperatures during the polar mesospheric cloud season, *Geophys. Res. Lett.*, *38*(11).
- Sheese, P., E. Llewellyn, R. Gattinger, and K. Strong (2014), OH Meinel band night-glow profiles from OSIRIS observations, *J. Geophys. Res. Atmos.*, *119*(19).
- Sica, R., and A. Russell (1999), Measurements of the effects of gravity waves in the middle atmosphere using parametric models of density fluctuations. part I: Vertical wavenumber and temporal spectra, *J. Atmos. Sci.*, *56*(10), 1308–1329.

- Silber, I., C. Price, C. Schmidt, S. Wüst, M. Bittner, and E. Pecora (2017), First ground-based observations of mesopause temperatures above the Eastern-Mediterranean part I: Multi-day oscillations and tides, *J. Atmos. Sol. Terr. Phys.*, *155*, 95–103.
- Simkhada, D., J. Snively, M. J. Taylor, and S. Franke (2009), Analysis and modeling of ducted and evanescent gravity waves observed in the Hawaiian airglow, in *Ann. Geophys.*, vol. 27, p. 3213, European Geosciences Union.
- Smith, A. K. (2004), Physics and chemistry of the mesopause region, *J. Atmos. Sol. Terr. Phys.*, *66*(10), 839–857.
- Smith, S., J. Baumgardner, and M. Mendillo (2009), Evidence of mesospheric gravity-waves generated by orographic forcing in the troposphere, *Geophys. Res. Lett.*, *36*(8).
- Swenson, G. (2005), Preface to special section on mesospheric dynamic and thermodynamic studies, *J. Geophys. Res. Atmos.*, *110*(D9).
- Swenson, G., M. J. Taylor, P. Espy, C. Gardner, and X. Tac (1995), ALOHA-93 measurements of intrinsic AGW characteristics using airborne airglow imager and groundbased Na wind/temperature lidar, *Geophys. Res. Lett.*, *22*(20), 2841–2844.
- Swenson, G. R., and S. B. Mende (1994), OH emission and gravity waves (including a breaking wave) in all-sky imagery from Bear Lake, UT, *Geophys. Res. Lett.*, *21*(20), 2239–2242.
- Takahashi, H., B. Clemesha, Y. Sahai, and P. Batista (1994), Seasonal variations of the mesopause temperature observed at equatorial (4 S) and low (23 S) latitude stations, *Advances in Space Research*, *14*(9), 97–100.

- Takahashi, H., B. Clemesha, and P. Batista (1995), Predominant semi-annual oscillation of the upper mesospheric airglow intensities and temperatures in the equatorial region, *J. Atmos. Sol. Terr. Phys.*, *57*(4), 407–414.
- Talaei, A., M. J. Taylor, P.-D. Pautet, Y. Zhao, T. S. Matsuda, and T. Nakamura (2015), Horizontal phase speed distribution of gravity waves observed in mesospheric temperature maps, in *CEDAR Conference Abstracts*.
- Tang, J., G. Swenson, A. Z. Liu, and F. Kamalabadi (2005), Observational investigations of gravity wave momentum flux with spectroscopic imaging, *J. Geophys. Res. Atmos.*, *110*(D9).
- Taori, A., and M. Taylor (2006), Characteristics of wave induced oscillations in mesospheric O₂ emission intensity and temperatures, *Geophys. Res. Lett.*, *33*(1).
- Taori, A., M. J. Taylor, and S. Franke (2005), Terdiurnal wave signatures in the upper mesospheric temperature and their association with the wind fields at low latitudes (20° N), *J. Geophys. Res. Atmos. (1984–2012)*, *110*(D9).
- Taylor, M., Y. Zhao, P. Pautet, J. Carstens, J. Pugmire, S. Smith, A. Liu, F. Vargas, G. Swenson, C. Randall, et al. (2016), Coordinated ground-based and AIM satellite measurements of mesospheric and stratospheric waves over South America, in *AGU Fall Meeting Abstracts*.
- Taylor, M. J. (1997), A review of advances in imaging techniques for measuring short period gravity waves in the mesosphere and lower thermosphere, *Advances in Space Research*, *19*(4), 667–676.
- Taylor, M. J., and R. Edwards (1991), Observations of short period mesospheric wave patterns: In situ or tropospheric wave generation?, *Geophys. Res. Lett.*, *18*(7), 1337–1340.

- Taylor, M. J., and F. Garcia (1995), A two-dimensional spectral analysis of short period gravity waves imaged in the OI (557.7 nm) and near infra red OH nightglow emissions over Arecibo, Puerto Rico, *Geophys. Res. Lett.*, *22*(18), 2473–2476.
- Taylor, M. J., and M. Hill (1991), Near infrared imaging of hydroxyl wave structure over an ocean site at low latitudes, *Geophys. Res. Lett.*, *18*(7), 1333–1336.
- Taylor, M. J., and W. Pendleton Jr (2003), Buoyancy and buoyancy waves: optical observations, in *Encyclopedia of Atmospheric Sciences*, edited by M. E. McIntyre, J. Holton, J. Pyle, and J. Curry, pp. 323–330, Academic Press, London.
- Taylor, M. J., M. Bishop, and V. Taylor (1995a), All-sky measurements of short period waves imaged in the OI (557.7 nm), Na (589.2 nm) and near infrared OH and O₂ (0, 1) nightglow emissions during the ALOHA-93 campaign, *Geophys. Res. Lett.*, *22*(20), 2833–2836.
- Taylor, M. J., D. Turnbull, and R. Lowe (1995b), Spectrometric and imaging measurements of a spectacular gravity wave event observed during the ALOHA-93 campaign, *Geophys. Res. Lett.*, *22*(20), 2849–2852.
- Taylor, M. J., D. Fritts, and J. Isler (1995c), Determination of horizontal and vertical structure of an unusual pattern of short period gravity waves imaged during ALOHA-93, *Geophys. Res. Lett.*, *22*(20), 2837–2840.
- Taylor, M. J., G. Swenson, and V. Taylor (1995d), Height measurements of OI (557.7 nm) gravity wave structure over the Hawaiian Islands during ALOHA-93, *Geophys. Res. Lett.*, *22*(20), 2881–2884.
- Taylor, M. J., Y. Gu, X. Tao, C. Gardner, and M. Bishop (1995e), An investigation of intrinsic gravity wave signatures using coordinated lidar and nightglow image measurements, *Geophys. Res. Lett.*, *22*(20), 2853–2856.

- Taylor, M. J., W. Pendleton Jr, C. Gardner, et al. (1999), Comparison of terdiurnal tidal oscillations in mesospheric OH rotational temperature and Na lidar temperature measurements at mid-latitudes for fall/spring conditions, *Earth Planets Space*, 51(7-8), 877–885.
- Taylor, M. J., L. Gardner, and W. Pendleton Jr (2001), Long-period wave signatures in mesospheric OH Meinel (6,2) band intensity and rotational temperature at mid-latitudes, *Advances in Space Research*, 27(6), 1171–1179.
- Taylor, M. J., A. Taori, D. Hatch, H. Liu, and R. Roble (2005), Characterization of the semi-annual-oscillation in mesospheric temperatures at low-latitudes, *Advances in Space Research*, 35(11), 2037–2043.
- Taylor, M. J., P. Pautet, Y. Zhao, J. Pugmire, N. Criddle, G. Swenson, A. Liu, and J. Hecht (2011), Investigating gravity waves and mesospheric temperature variability over the Andes Mountains, in *AGU Fall Meeting Abstracts*.
- Taylor, M. J., P. Pautet, D. Fritts, B. Kaifler, Y. Zhao, S. Smith, P. McLaughlin, M. Eckermann, M. McCarthy, M. Rapp, L. Liley, and W. Pendleton Jr (2018), Gravity wave investigations during DEPWAVE (using an Advanced Mesospheric Temperature Mapper), in *European Geosciences Union General Assembly*.
- Torre, A., P. Alexander, R. Hierro, P. Llamedo, A. Rolla, T. Schmidt, and J. Wickert (2012), Large-amplitude gravity waves above the southern Andes, the Drake Passage, and the Antarctic Peninsula, *J. Geophys. Res. Atmos.*, 117(D2).
- Torre, A., P. Alexander, P. Llamedo, R. Hierro, B. Nava, S. Radicella, T. Schmidt, and J. Wickert (2014), Wave activity at ionospheric heights above the Andes Mountains detected from FORMOSAT-3/COSMIC GPS radio occultation data, *J. Geophys. Res. Sp. Phys.*, 119(3), 2046–2051.

- Tsuda, T., Y. Murayama, T. Nakamura, R. Vincent, A. Manson, C. Meek, and R. Wilson (1994), Variations of the gravity wave characteristics with height, season and latitude revealed by comparative observations, *J. Atmos. Sol. Terr. Phys.*, *56*(5), 555–568.
- Vargas, F., G. Swenson, A. Liu, and D. Pautet (2016), Evidence of the excitation of a ring-like gravity wave in the mesosphere over the Andes Lidar Observatory, *J. Geophys. Res. Atmos.*, *121*(15), 8896–8912.
- Vincent, R. A., and M. Joan Alexander (2000), Gravity waves in the tropical lower stratosphere: An observational study of seasonal and interannual variability, *J. Geophys. Res. Atmos.* (1984–2012), *105*(D14), 17,971–17,982.
- von Savigny, C. (2015), Variability of OH (3–1) emission altitude from 2003 to 2011: Long-term stability and universality of the emission rate–altitude relationship, *J. Atmos. Sol. Terr. Phys.*, *127*, 120–128.
- von Savigny, C., K.-U. Eichmann, E. Llewellyn, H. Bovensmann, J. Burrows, M. Bittner, K. Höppner, D. Offermann, M. J. Taylor, Y. Zhao, et al. (2004), First near-global retrievals of OH rotational temperatures from satellite-based Meinel band emission measurements, *Geophys. Res. Lett.*, *31*(15).
- Wallace, L., and A. Broadfoot (1969), Weak emissions in the near infrared daytime airglow, *Planet. Space Sci.*, *17*(5), 975–984.
- Walterscheid, R., and M. P. Hickey (2005), Acoustic waves generated by gusty flow over hilly terrain, *J. Geophys. Res. Sp. Phys.*, *110*(A10).

- Walterscheid, R., J. Hecht, L. Gelinas, A. MacKinnon, R. Vincent, I. Reid, S. Franke, Y. Zhao, M. Taylor, and P. Pautet (2015), Simultaneous observations of the phase-locked 2 day wave at Adelaide, Cerro Pachon, and Darwin, *J. Geophys. Res. Atmos.*, *120*(5), 1808–1825.
- Whiteway, J. A., and A. I. Carswell (1995), Lidar observations of gravity wave activity in the upper stratosphere over Toronto, *J. Geophys. Res. Atmos.*, *100*(D7), 14,113–14,124.
- Wit, R., D. Janches, D. Fritts, and R. Hibbins (2016), QBO modulation of the mesopause gravity wave momentum flux over Tierra del Fuego, *Geophys. Res. Lett.*, *43*(8), 4049–4055.
- Wit, R., D. Janches, D. Fritts, R. Stockwell, and L. Coy (2017), Unexpected climatological behavior of MLT gravity wave momentum flux in the lee of the Southern Andes hot spot, *Geophys. Res. Lett.*, *44*(2), 1182–1191.
- Worthington, R., and L. Thomas (1996), Radar measurements of critical-layer absorption in mountain waves, *Quarterly Journal of the Royal Meteorological Society*, *122*(534), 1263–1282.
- Xu, J., C. She, W. Yuan, C. Mertens, M. Mlynczak, and J. Russell (2006), Comparison between the temperature measurements by TIMED/SABER and lidar in the midlatitude, *J. Geophys. Res. Sp. Phys.*, *111*(A10).
- Xu, J., A. Smith, G. Jiang, H. Gao, Y. Wei, M. Mlynczak, and J. Russell (2010), Strong longitudinal variations in the OH nightglow, *Geophys. Res. Lett.*, *37*(21).
- Xu, J., H. Gao, A. K. Smith, and Y. Zhu (2012), Using TIMED/SABER nightglow observations to investigate hydroxyl emission mechanisms in the mesopause region, *J. Geophys. Res. Atmos.*, *117*(D2).

- Yamashita, C., S. L. England, T. J. Immel, and L. C. Chang (2013), Gravity wave variations during elevated stratopause events using SABER observations, *J. Geophys. Res. Atmos.*, *118*(11), 5287–5303.
- Yee, J.-H., G. Crowley, R. Roble, W. Skinner, M. Burrage, and P. Hays (1997), Global simulations and observations of O (1S), O₂ (1 σ) and OH mesospheric nightglow emissions, *J. Geophys. Res. Sp. Phys.*, *102*(A9), 19,949–19,968.
- Yee, J.-H., G. E. Cameron, and D. Y. Kusnierkiewicz (1999), Overview of TIMED, in *Optical Spectroscopic Techniques and Instrumentation for Atmospheric and Space Research III*, vol. 3756, pp. 244–255, International Society for Optics and Photonics.
- Yoshiki, M., and K. Sato (2000), A statistical study of gravity waves in the polar regions based on operational radiosonde data, *J. Geophys. Res. Atmos. (1984–2012)*, *105*(D14), 17,995–18,011.
- Yuan, T., P.-D. Pautet, Y. Zhao, X. Cai, N. R. Criddle, M. J. Taylor, and W. Pendleton (2014), Coordinated investigation of midlatitude upper mesospheric temperature inversion layers and the associated gravity wave forcing by Na lidar and Advanced Mesospheric Temperature Mapper in Logan, Utah, *J. Geophys. Res. Atmos.*, *119*(7), 3756–3769.
- Yuan, T., C. J. Heale, J. B. Snively, X. Cai, P.-D. Pautet, C. Fish, Y. Zhao, M. J. Taylor, W. Pendleton, V. Wickwar, et al. (2016), Evidence of dispersion and refraction of a spectrally broad gravity wave packet in the mesopause region observed by the Na lidar and Mesospheric Temperature Mapper above Logan, Utah, *J. Geophys. Res. Atmos.*, *121*(2), 579–594.

- Zhang, S. P., R. G. Roble, and G. G. Shepherd (2001), Tidal influence on the oxygen and hydroxyl nightglows: Wind imaging interferometer observations and thermosphere/ionosphere/mesosphere electrodynamics general circulation model, *J. Geophys. Res. Sp. Phys.*, *106*(A10), 21,381–21,393.
- Zhao, Y., M. J. Taylor, and X. Chu (2005), Comparison of simultaneous Na lidar and mesospheric nightglow temperature measurements and the effects of tides on the emission layer heights, *J. Geophys. Res. Atmos.*, *110*(D9).
- Zhao, Y., M. J. Taylor, H.-L. Liu, and R. Roble (2007), Seasonal oscillations in mesospheric temperatures at low-latitudes, *J. Atmos. Sol. Terr. Phys.*, *69*(17), 2367–2378.
- Zhao, Y., M. Taylor, M. Hagan, P. Pautet, J. Pugmire, W. Pendleton Jr, and J. Russell III (2016), Investigating the 90-day oscillations using ground-based, satellite and TIME-GCM model simulation data, in *AGU Fall Meeting Abstracts*.

APPENDIX

APPENDIX A
COPYRIGHT PERMISSIONS

Five figures from Chapters 4, 5, and 6 of this dissertation required copyright permission from their original sources. The following figures are copies of the copyright permissions granted by the publications' publishers.

**JOHN WILEY AND SONS LICENSE
TERMS AND CONDITIONS**

Jul 09, 2018

This Agreement between Jonathan R Pugmire ("You") and John Wiley and Sons ("John Wiley and Sons") consists of your license details and the terms and conditions provided by John Wiley and Sons and Copyright Clearance Center.

License Number	4384941238858
License date	Jul 09, 2018
Licensed Content Publisher	John Wiley and Sons
Licensed Content Publication	Journal of Geophysical Research: Atmospheres
Licensed Content Title	Assessment of the quality of the Version 1.07 temperature-versus-pressure profiles of the middle atmosphere from TIMED/SABER
Licensed Content Date	Sep 3, 2008
Licensed Content Pages	10
Type of use	Dissertation/Thesis
Requestor type	University/Academic
Format	Print and electronic
Portion	Figure/table
Number of figures/tables	2
Original Wiley figure/table number(s)	Figure 21, Figure 22
Will you be translating?	No
Title of your thesis / dissertation	Mesospheric Gravity Wave Climatology and Variances over the Andes Mountains
Expected completion date	Aug 2018
Expected size (number of pages)	169
Requestor Location	Jonathan R Pugmire 577 North 100 West Logan, UT 84321 United States Attn:
Publisher Tax ID	EU826007151
Total	0.00 USD
Terms and Conditions	

TERMS AND CONDITIONS

This copyrighted material is owned by or exclusively licensed to John Wiley & Sons, Inc. or one of its group companies (each a "Wiley Company") or handled on behalf of a society with which a Wiley Company has exclusive publishing rights in relation to a particular work (collectively "WILEY"). By clicking "accept" in connection with completing this licensing transaction, you agree that the following terms and conditions apply to this transaction (along with the billing and payment terms and conditions established by the Copyright

Figure A.1. Copyright permission for use of Figure 4.3 [*Remsberg et al.*, 2008].

**JOHN WILEY AND SONS LICENSE
TERMS AND CONDITIONS**

Jul 09, 2018

This Agreement between Jonathan R Pugmire ("You") and John Wiley and Sons ("John Wiley and Sons") consists of your license details and the terms and conditions provided by John Wiley and Sons and Copyright Clearance Center.

License Number	4384940935586
License date	Jul 09, 2018
Licensed Content Publisher	John Wiley and Sons
Licensed Content Publication	Geophysical Research Letters
Licensed Content Title	Intercomparison of kinetic temperature from 15 μm CO ₂ limb emissions and OH*(3,1) rotational temperature in nearly coincident air masses: SABER, GRIPS
Licensed Content Date	Jul 22, 2006
Licensed Content Pages	10
Type of use	Dissertation/Thesis
Requestor type	University/Academic
Format	Print and electronic
Portion	Figure/table
Number of figures/tables	1
Original Wiley figure/table number(s)	Figure 1b
Will you be translating?	No
Title of your thesis / dissertation	Mesospheric Gravity Wave Climatology and Variances over the Andes Mountains
Expected completion date	Aug 2018
Expected size (number of pages)	169
Requestor Location	Jonathan R Pugmire 577 North 100 West Logan, UT 84321 United States Attn:
Publisher Tax ID	EU826007151
Total	0.00 USD
Terms and Conditions	

TERMS AND CONDITIONS

This copyrighted material is owned by or exclusively licensed to John Wiley & Sons, Inc. or one of its group companies (each a "Wiley Company") or handled on behalf of a society with which a Wiley Company has exclusive publishing rights in relation to a particular work (collectively "WILEY"). By clicking "accept" in connection with completing this licensing transaction, you agree that the following terms and conditions apply to this transaction (along with the billing and payment terms and conditions established by the Copyright

Figure A.2. Copyright permission for use of Figure 4.7b [*Oberheide et al., 2006*].

**ELSEVIER LICENSE
TERMS AND CONDITIONS**

Jul 09, 2018

This Agreement between Jonathan R Pugmire ("You") and Elsevier ("Elsevier") consists of your license details and the terms and conditions provided by Elsevier and Copyright Clearance Center.

License Number	4384960236016
License date	Jul 09, 2018
Licensed Content Publisher	Elsevier
Licensed Content Publication	Journal of Atmospheric and Solar-Terrestrial Physics
Licensed Content Title	Gravity wave activity in the mesopause region from airglow measurements at El Leoncito
Licensed Content Author	Esteban R. Reisin, Jürgen Scheer
Licensed Content Date	April–June 2004
Licensed Content Volume	66
Licensed Content Issue	6-9
Licensed Content Pages	7
Start Page	655
End Page	661
Type of Use	reuse in a thesis/dissertation
Intended publisher of new work	other
Portion	figures/tables/illustrations
Number of figures/tables/illustrations	1
Format	both print and electronic
Are you the author of this Elsevier article?	No
Will you be translating?	No
Original figure numbers	Figure 4
Title of your thesis/dissertation	Mesospheric Gravity Wave Climatology and Variances over the Andes Mountains
Expected completion date	Aug 2018
Estimated size (number of pages)	169
Requestor Location	Jonathan R Pugmire 577 North 100 West Logan, UT 84321 United States Attn:
Publisher Tax ID	98-0397604
Total	0.00 USD

Figure A.3. Copyright permission for use of Figure 5.5 [*Reisin and Scheer, 2004*].

**JOHN WILEY AND SONS LICENSE
TERMS AND CONDITIONS**

Jul 09, 2018

This Agreement between Jonathan R Pugmire ("You") and John Wiley and Sons ("John Wiley and Sons") consists of your license details and the terms and conditions provided by John Wiley and Sons and Copyright Clearance Center.

License Number	4384951316147
License date	Jul 09, 2018
Licensed Content Publisher	John Wiley and Sons
Licensed Content Publication	Journal of Geophysical Research: Atmospheres
Licensed Content Title	Upper Atmosphere Research Satellite (UARS) MLS observation of mountain waves over the Andes
Licensed Content Date	Sep 12, 2002
Licensed Content Pages	1
Type of use	Dissertation/Thesis
Requestor type	University/Academic
Format	Print and electronic
Portion	Figure/table
Number of figures/tables	1
Original Wiley figure/table number(s)	Figure 2
Will you be translating?	No
Title of your thesis / dissertation	Mesospheric Gravity Wave Climatology and Variances over the Andes Mountains
Expected completion date	Aug 2018
Expected size (number of pages)	169
Requestor Location	Jonathan R Pugmire 577 North 100 West Logan, UT 84321 United States Attn:
Publisher Tax ID	EU826007151
Total	0.00 USD
Terms and Conditions	

TERMS AND CONDITIONS

This copyrighted material is owned by or exclusively licensed to John Wiley & Sons, Inc. or one of its group companies (each a "Wiley Company") or handled on behalf of a society with which a Wiley Company has exclusive publishing rights in relation to a particular work (collectively "WILEY"). By clicking "accept" in connection with completing this licensing transaction, you agree that the following terms and conditions apply to this transaction (along with the billing and payment terms and conditions established by the Copyright Clearance Center Inc., ("CCC's Billing and Payment terms and conditions"), at the time that

Figure A.4. Copyright permission for use of Figure 6.4 [*Jiang et al.*, 2002].

**JOHN WILEY AND SONS LICENSE
TERMS AND CONDITIONS**

Jul 09, 2018

This Agreement between Jonathan R Pugmire ("You") and John Wiley and Sons ("John Wiley and Sons") consists of your license details and the terms and conditions provided by John Wiley and Sons and Copyright Clearance Center.

License Number	4384951474991
License date	Jul 09, 2018
Licensed Content Publisher	John Wiley and Sons
Licensed Content Publication	Geophysical Research Letters
Licensed Content Title	Evidence of mesospheric gravity-waves generated by orographic forcing in the troposphere
Licensed Content Date	Apr 17, 2009
Licensed Content Pages	10
Type of use	Dissertation/Thesis
Requestor type	University/Academic
Format	Print and electronic
Portion	Figure/table
Number of figures/tables	1
Original Wiley figure/table number(s)	Figure 3
Will you be translating?	No
Title of your thesis / dissertation	Mesospheric Gravity Wave Climatology and Variances over the Andes Mountains
Expected completion date	Aug 2018
Expected size (number of pages)	169
Requestor Location	Jonathan R Pugmire 577 North 100 West Logan, UT 84321 United States Attn:
Publisher Tax ID	EU826007151
Total	0.00 USD
Terms and Conditions	

TERMS AND CONDITIONS

This copyrighted material is owned by or exclusively licensed to John Wiley & Sons, Inc. or one of its group companies (each a "Wiley Company") or handled on behalf of a society with which a Wiley Company has exclusive publishing rights in relation to a particular work (collectively "WILEY"). By clicking "accept" in connection with completing this licensing transaction, you agree that the following terms and conditions apply to this transaction (along with the billing and payment terms and conditions established by the Copyright

Figure A.5. Copyright permission for use of Figure 6.5 [*Smith et al.*, 2009].

Jonathan Rich Pugmire

Curriculum Vitae

SER Building 209
 Department of Physics
 Utah State University
 Logan, Utah 84322

Voice: (801) 648-6992
 Email: jon.pugmire1@gmail.com
https://works.bepress.com/jonathan_pugmire/

EDUCATION

- **Ph.D. Physics.** 2018.
 "Mesospheric Gravity Wave Climatology and Variances over the Andes Mountains"
 Advisor: Michael J. Taylor, Ph.D.
Utah State University, Logan, Utah
 PhD Defended, June 21st, 2018
- **B.S. Physics. Professional Emphasis, Mathematics Minor,** May 2010.
 Cum Laude, Undergraduate Research Scholar
 Research project: "*Mesospheric Temperature Mapping Data Analysis Over the Andes*"
Utah State University, Logan, Utah

RESEARCH INTERESTS

Atmospheric physics, astronomy, and physics education.

ACADEMIC POSITIONS and SERVICE

- **Graduate Research Assistant.**
 Atmospheric Imaging Lab, Center for Atmospheric and Space Sciences.
 Logan, Utah. May 2009–present.
- **Graduate Teaching Assistant.**
 Physics Department, USU.
 Logan, Utah. 2010–present.
- **Graduate Enhancement Award Reviewer.**
 USU Student Association
 Logan, Utah. 2018.

TEACHING EXPERIENCE

- **Physics Instructor**, USU, Logan, Utah.
PHYS 1040: Introduction to Astronomy: Summer 2016.
PHYS 2215: Physics for Scientists and Engineers Lab I: Fall 2017.
PHYS 2220: Physics for Scientists and Engineers: Summer 2017.
PHYS 2225: Physics for Scientists and Engineers Lab II: Spring 2013, 2017; Fall 2015.
- **Physics Instructor**, USU, Brigham City Campus, Utah.
PHYS 2225: Physics for Scientists and Engineers II: Summer 2013

- **Teaching Assistant**, USU, Logan, Utah, Fall 2010-Fall 2016.
PHYS 1040: Introduction to Astronomy: Teaching Assistant.
PHYS 1800: Physics of Technology: Substitute Instructor, Recitation Leader and Lab Instructor.
PHYS 2115: The Physics of Living Systems Lab I: Lab Instructor.
PHYS 2215: Physics for Scientists and Engineers Lab I: Lab Instructor.
PHYS 3870: Intermediate Physics Lab: Higher division Lab Instructor.
PHYS 3880: Advanced Physics Lab: Higher division Lab Instructor - Facilitated group undergraduate research projects.

ADVANCED GRADUATE SCHOOLS

- **International Incoherent Scatter Radar School.**
 Sodankylä Geophysical Observatory, Sodankylä, Finland, July 2016.
 Six day radar workshop organized by the Sodankylä Geophysical Observatory and SRI International sponsored by the European Incoherent Scatter Scientific Association (EISCAT) and the National Science Foundation (NSF).
- **PASI School and Workshop on the Dynamics and Chemistry of the Upper Atmosphere.**
 San Juan, Argentina, October 2010.
 Six day school under the sponsorship of the U.S. NSF's Pan-American Advanced Studies Institutes (PASI) program.

PROFESSIONAL MEMBERSHIP

- American Association of Physics Teachers, member
- SPIE, International Society for Optics and Photonics, USU Chapter, member
- American Radio Relay League; Bridgerland Amateur Radio Club, KI7BEN
- Society of Physics Students, USU Chapter
- Sigma Pi Sigmas, Physics Honor Society, USU Chapter
- Cache Valley Astronomical Society, member

EDUCATIONAL AND PUBLIC OUTREACH

- **August 21, 2017, USU Physics Department Solar Eclipse Outreach, Rigby, Idaho** - volunteer host running solar telescopes and educating the public about the sun.
- **April 2017 – present, Utah STEM Action Center** â STEM Ambassador.
- **February 2016 – present, Bridgerland Amateur Radio Club** â volunteer, ham radio test preparation.
- **August 2014 – present, USU Observatory** â volunteer host.
- **2012 – present, Boy Scouts of America** â Merit Badge Councilor, Troop Committee Member.
- **May 2010 – present, USU Physics Day at Lagoon** â volunteer.
- **June 2016** â Space camp presentation to 30 under-represented elementary-age students about the solar system.

- **February 2016** â Presentation to 80 students about research and travelling to Antarctica.
- **Summer 2014** â Hosted 120 8th graders as they toured the USU Physics Department and the Center for Atmospheric and Space Sciences.
- **Feb 21, 2014, USU Science Unwrapped Lecture** â Conducted physics demonstrations and talked about research in Antarctica.
- **2013** â Travelled to the McMurdo Station, Antarctica and the South Pole on a research expedition. As a result USU, my research, and the trip were highlighted in several news stories:
 - **ABC 4 News.** USU grad student travels to South Pole. Conway, K. (March 4, 2013). abc4.com
 - **Standard Examiner.** USU team travels to South Pole to measure gravity waves. Van Valkenburg, N. (March 4, 2013). <http://standard.net/>
 - **Herald Journal.** USU grad student, researchers collect project data at South Pole. Opsahl, K.(March 7, 2013). <http://news.hjnews.com/>
 - **Utah State Today.** Catching Waves: USU Grad Student Studies Mesosphere from South Pole. Muffoletto, M.-A. (March 7, 2013). <http://www.usu.edu/ust/>

GRANTS, HONORS and AWARDS

1. **Travel Grant and Support, NSF, \$2600, July 2016.**
2. **Keith Taylor Graduate Fellowship, \$4000, 2015.**
3. **Graduate Oral Presentation Winner, USU Student Research Symposium, April 2015.**
4. **Graduate Student Travel Grant, AGU '14, \$300, 2014.**
5. **Utah NASA Space Grant Consortium Fellowship, \$15,000, 2014.**
6. **Keith Taylor Graduate Fellowship, \$4000, 2014.**
7. **Antartica Service Metal, US Department of Defense, 2013.**
8. **Utah NASA Space Grant Consortium Fellowship, \$15,000, 2013.**
9. **Rocky Mountain NASA Space Grant Consortium Fellowship, \$15,000, 2012.**
10. **Outstanding Teaching Assistant, Physics Department, \$500, 2012.**
11. **Travel Grant and Support, PASI Workshop, \$3000, October 2010.**
12. **Best Graduate Presentation, APS 4-Corners Conference, October 2010.**
13. **Honorable Mention Presentation, CEDAR Conference, June 2010.**
14. **Sigma Pi Sigma Physics Honor Society, April 2010.**
15. **Outstanding Graduating Senior, Physics Department \$500, May 2010.**
16. **Cume Laude, USU, May 2010.**
17. **Undergraduate Research Scholar, May 2010.**
18. **Best Undergraduate Research Presentation, APS 4-Corners Conference, 2009.**
19. **Presidential Scholarship, \$10,000, 2003.**

RESEARCH TALKS PRESENTED

1. **International ISR School.** Sodankylä, Finland, July 2016.
Observations of Polar Mesospheric Summer Echoes with EISCAT VHF Radar.
Jonathan Pugmire, V. Belakhovsky, K. Dubin, H. Lawal, H. Lyu, J. Norberg.
2. **Coupling, Energetics, and Dynamics of Atmospherics Regions (CEDAR) Conference.** Seattle, WA, June 2015.
Satellite measurements of mesospheric gravity wave temperature variance over the Andes.
Jonathan Pugmire, Michael J. Taylor and Yucheng Zhao.
3. **Utah NASA Space Grant Consortium Fellowship Symposium.** Salt Lake City, UT, May 2015.
Mesospheric dynamics and temperature variance studies using satellite and ground-based instruments.
Jonathan Pugmire and Michael J. Taylor.
4. **USU Student Research Symposium.** Logan, UT, April 2015.
Observations of mesospheric gravity waves over the Andes.
Jonathan Pugmire, Michael J. Taylor and Yucheng Zhao.
5. **American Geophysical Union Fall Meeting.** San Francisco, CA, December 2014.
Investigating Mesospheric Gravity Wave Dynamics Over McMurdo Station, Antarctica (77° S).
Jonathan Pugmire, Michael J. Taylor and P. Dominique Pautet.
6. **Antarctic Gravity Wave Instrument Network Workshop.** Logan, UT, October 2014.
New measurements of McMurdo gravity wave parameters.
Jonathan Pugmire, Michael J. Taylor and P. Dominique Pautet.
7. **American Physical Society (APS) 4-Corners Meeting.** Orem, UT, October 2014.
TIMED/SABER satellite investigations of mesospheric gravity wave variances over the Andes.
Jonathan Pugmire, Michael J. Taylor and Yucheng Zhao.
8. **CEDAR Conference.** Seattle, WA, June 2014.
Investigating Mesospheric Gravity Wave Dynamics Over McMurdo Station, Antarctica.
Jonathan Pugmire, Michael J. Taylor, Yucheng Zhao and P. Dominique Pautet.
9. **Utah Space Grant Consortium Fellowship Symposium.** Ogden, UT, May 2014.
Observations of Mesospheric Gravity Wave Dynamics in the Southern Hemisphere.
Jonathan Pugmire and Michael J. Taylor.
10. **APS 4-Corners Conference.** Denver, CO, October 2013.
Satellite and Ground-Based Measurements of Mesospheric Temperature Variability Over Cerro Pachon, Chile (30.3° S).
J.R. Pugmire, M.J. Taylor, Y. Zhao, P.D. Pautet and J.M. Russell III.
11. **CEDAR Conference.** Boulder, CO, June 2013.
Observations of Mesospheric Temperature Variability Over the Andes.
J.R. Pugmire, M.J. Taylor, Y. Zhao, P.D. Pautet and J.M. Russell III.

12. **Utah Space Grant Consortium Fellowship Symposium.** Salt Lake City, UT, May 2013.
Investigating Mesospheric Gravity Wave Dynamics and Temperature Variability over the Andes.
Jonathan R. Pugmire and Michael J. Taylor.
13. **CEDAR Conference.** Santa Fe, NM, June 2011.
Mesospheric Temperature Measurements and Seasonal Variability Over the Andes.
Jonathan R. Pugmire, Michael J. Taylor, Yucheng Zhao and P. Dominique Pautet.
14. **PASI School and Workshop on the Dynamics and Chemistry of the Upper Atmosphere.** San Juan, Argentina, October 2010.
First Year Investigation of Gravity Waves and Temperature Variability over the Andes.
J.R. Pugmire, N. Criddle, M.J. Taylor, P.D. Pautet and Y. Zhao.

INVITED LECTURES

- **Professional**

- **USU Physics Colloquium.** Logan, Utah, September, 2015.
Mesospheric temperature variance measurements using SABER and ground-based instruments.
- **USU Physics Colloquium.** Logan, Utah, September, 2014.
My Summer in the Mountains Looking at Waves.

TEACHING REFERENCES

- | | |
|--|--|
| <ul style="list-style-type: none"> • Vincent Wickwar, Ph.D.
Professor of Physics, USU
<i>Phone:</i> 435-797-3641
<i>email:</i> vincent.wickwar@usu.edu | <ul style="list-style-type: none"> • Michael J. Taylor, Ph.D.
Professor of Physics, USU
<i>Phone:</i> 435-797-3919
<i>email:</i> mike.taylor@usu.edu |
| <ul style="list-style-type: none"> • J.R. Dennison, Ph.D.
Professor of Physics, USU
<i>Phone:</i> 435-797-2936
<i>email:</i> jr.dennison@usu.edu | <ul style="list-style-type: none"> • James Coburn
Teacher and Lab Supervisor, USU
<i>Phone:</i> 435-797-3014
<i>email:</i> james.coburn@usu.edu |

RESEARCH REFERENCES

- **Michael J. Taylor, Ph.D.**
PhD Advisor
Professor of Physics, USU
Phone: 435-797-3919
email: mike.taylor@usu.edu